

TABLE OF CONTENTS

	Page
SUMMARY	1 1/A11
INTRODUCTION	1 1/A11
SYMBOLS	4 1/A14
PROGRAM DESCRIPTION	5 1/B1
Task I – Extension of Method to Account for Skin Friction Effects	6 1/B2
Task II – Inclusion of Jet Entrainment Effects	11 1/B7
Task III – Development of a Viscous Flow Computer Program	14 1/B10
Task IV – Assessment of Accuracy of Method	17 1/B13
RECOMMENDATION FOR NEW DATA REQUIRED	20 1/C2
SUMMARY OF RESULTS AND RECOMMENDATIONS	21 1/C3
REFERENCES	23 1/C5
APPENDIX AN AFTERBODY VISCOUS FLOW USER'S MANUAL	61 1/F1

UG 14 1978

item 830-H-14

NAS 1.26: 3028

NASA Contractor Report 3028

**ORIGINAL
COMPLETED**

**An Improved Analytical Model
of the Separation Region on
Boattail Nozzles at Subsonic Speeds**

**Walter M. Presz, Jr., Ronald W. King,
and John D. Buteau**

**CONTRACT NAS1-14462
JULY 1978**

NASA

88

NASA Contractor Report 3028

**An Improved Analytical Model
of the Separation Region on
Boattail Nozzles at Subsonic Speeds**

Walter M. Presz, Jr., Ronald W. King,
and John D. Buteau
*United Technologies Corporation
East Hartford, Connecticut*

Prepared for
Langley Research Center
under Contract NAS1-14462



National Aeronautics
and Space Administration

Scientific and Technical
Information Office

1978

BLANK PAGE

FOREWORD

This report describes work performed by the Pratt & Whitney Aircraft Group, Commercial Products Division, United Technologies Corporation, for the National Aeronautics and Space Administration, Langley Research Center under Contract NAS1-14462. During this effort Mr. Lawrence E. Putnam was the NASA Project Manager and Dr. W. M. Presz, Jr. was the P&WA Program Manager. The report includes a user's manual for an afterbody viscous flow computer program developed under the contract. The user's manual is presented as an appendix.

BLANK PAGE

LIST OF ILLUSTRATIONS

Figure		Page
1	Schematic of the Separated Afterbody Flowfield	25
2	Comparison of Measured and Predicted Separation Angles	25
3	Comparison of Measured and Predicted Pressures on a Separated Afterbody At $M_\infty = 0.5$ with $\beta = 16^\circ$ and $(\delta^*/r) = 0.04$	26
4	Differential Control Volume Analytical Model	27
5	Assumed Reverse Flow Velocity Profile	28
6	Comparison of Calculated Discriminating Streamline Shapes for Circular Arc Nozzle Configuration With $\beta = 17^\circ$ and $d_b/D = 0.51$ at $M_\infty = 0.6$	28
7	Comparison of Calculated Discriminating Streamline Shapes For Circular Arc Nozzle Configuration With $\beta = 17^\circ$ and $d_b/D = 0.51$ at $M_\infty = 0.8$	29
8	Comparison of Calculated Discriminating Streamline Shapes For Circular Arc Nozzle Configuration With $\beta = 17^\circ$ and $d_b/D = 0.51$ at $M_\infty = 0.90$	29
9	Comparison of Calculated Discriminating Streamline Shapes For Circular Arc Nozzle Configuration With $\beta = 17^\circ$ and $d_b/D = 0.51$ at $M_\infty = 0.94$	30
10	Comparison of Calculated Discriminating Streamline Shapes For Circular Arc Nozzle Configuration With $\beta = 13.8^\circ$ and $d_b/D = 0.51$ at $M_\infty = 0.8$	30
11	Comparison of Calculated Discriminating Streamline Shapes For Circular Arc Nozzle Configuration With $\beta = 13.8^\circ$ and $d_b/D = 0.51$ at $M_\infty = 0.90$	31
12	Comparison of Calculated Discriminating Streamline Shapes For Circular Arc Nozzle Configuration With $\beta = 13.8^\circ$ and $d_b/D = 0.51$ at $M_\infty = 0.94$	31
13	Comparison of Calculated Discriminating Streamline Shapes For Circular Arc Nozzle Configuration With $\beta = 11^\circ$ and $d_b/D = 0.61$ at $M_\infty = 0.8$	32

LIST OF ILLUSTRATIONS (Cont'd)

Figure		Page
14	Comparison of Calculated Discriminating Streamline Shapes For Circular Arc Nozzle Configuration With $\beta = 11^\circ$ and $d_b/D = 0.61$ at $M_\infty = 0.90$	32
15	Comparison of Measured and Predicted Separation Angles	33
16	Skin Friction and Pressure Gradient Effects on the Calculated Discriminating Streamline For Circular Arc Nozzle Configuration With $\beta = 17^\circ$ and $d_b/D = 0.51$ at $M_\infty = 0.6$	34
17	Discriminating Streamline Shape Effects on Afterbody Pressures For Circular Arc Nozzle Configuration With $\beta = 17^\circ$ and $d_b/D = 0.51$ at $M_\infty = 0.6$	34
18	Comparison of Predicted Separation Angles	35
19	Major Components of the Calculation Scheme	35
20	Discrete Control Volume For Jet Entrainment Region	36
21	Jet Shearing Effects on Predicted Afterbody Pressure For Circular Arc Nozzle Configuration With $\ell/D = 0.8$ and $d_b/D = 0.51$ at $M_\infty = 0.8$ and $NPR = 2.00$	37
22	Schematic of the Flow Recirculation Regions	38
23	Schematic of the Jet Recirculation Flowfield	39
24	Schematic of the Assumed Velocity Profiles	39
25	A Schematic of the Viscous Flow Calculation	40
26	Convergence of the Viscous Inviscid Flow Iteration Scheme for a Circular Arc Conical Afterbody Configuration (6524) With an $\ell/D = 0.961$ and $d_b/D = 0.50$ at $M_\infty = 0.601$ and a Reynolds Number of 4.29×10^7	41
27	Comparison of Measured and Predicted Afterbody Pressures for a Circular Arc Conical Afterbody Configuration (6524) With $\ell/D = 0.961$ and $d_b/D = 0.50$ at $M_\infty = 0.601$ and a Reynolds Number of 4.29×10^7	42

LIST OF ILLUSTRATIONS (Cont'd)

Figure		Page
28	Comparison of Measured and Predicted Afterbody Pressures For a Circular Arc Conical Afterbody Configuration With $\ell/D = 0.961$ and $d_b/D = 0.50$ at $M_\infty = 0.597$ and a Reynolds Number of 2.61×10^6	43
29	Comparison of Measured and Predicted Afterbody Pressures For a Circular Arc Nozzle Configuration With $\beta = 17^\circ$ and $d_b/D = 0.51$ at $M_\infty = 0.397$	44
30	Comparison of Measured and Predicted Afterbody Pressures For a Circular Arc Nozzle Configuration With $\beta = 17^\circ$ and $d_b/D = 0.51$ at $M_\infty = 0.6$	45
31	Comparison of Measured and Predicted Afterbody Pressures For a Circular Arc Nozzle Configuration With $\beta = 17^\circ$ and $d_b/D = 0.51$ at $M_\infty = 0.8$	46
32	Comparison of Measured and Predicted Afterbody Pressures With Separation Point Fixed at Experimental Location for a Circular Arc Nozzle Configuration With $\beta = 17^\circ$ and $d_b/D = 0.51$ at $M_\infty = 0.6$	47
33	Comparison of Measured and Predicted Afterbody Pressures For a Circular Arc Nozzle Configuration With $\beta = 11^\circ$ and $d_b/D = 0.61$ at $M_\infty = 0.798$	48
34	Comparison of Measured and Predicted Pressures for Shrewsbury Configuration 1015 at $M_\infty = 0.7$	49
35	Effect of Separation Location on Predicted Pressures and Drag of Circular Arc Nozzle Configuration With $\beta = 13.4^\circ$ and $d_b/D = 0.51$ at $M_\infty = 0.798$	50
36	Effect of Jet Entrainment on Discriminating Streamline Shape of a Circular Arc Afterbody at $M_\infty = 0.6$ and $NPR = 2.91$	51
37	Effect of Entrainment on Afterbody Calculated Pressures for a Circular Arc Nozzle Configuration With $\beta = 17^\circ$ and $d_b/D = 0.51$ at $M_\infty = 0.8$ and $NPR = 2.91$	52
38	Comparison of Measured and Predicted Afterbody Pressures for a Circular Arc Nozzle Afterbody With $\beta = 17^\circ$ and $d_b/D = 0.51$ at $M_\infty = 0.6$ and $NPR = 2.91$	53

LIST OF ILLUSTRATIONS (Cont'd)

Figure		Page
39	Comparison of Measured and Predicted Afterbody Pressures for a Circular Arc Afterbody With $\beta = 17^\circ$ and $d_b/D = 0.51$ at $M_\infty = 0.8$ and $NPR = 2.91$	54
40	Comparison of Measured and Predicted Afterbody Pressures for a Circular Arc Afterbody With $\beta = 17^\circ$ and $d_b/D = 0.51$ at $M_\infty = 0.598$ and $NPR = 2.002$	55
41	Comparison of Measured and Predicted Afterbody Pressures for a Circular Arc Afterbody With $\beta = 17^\circ$ and $d_b/D = 0.51$ at $M_\infty = 0.8$ and $NPR = 2.0$	56
42	Comparison of Measured and Predicted Afterbody Pressures for a Circular Arc Afterbody With $\beta = 17^\circ$ and $d_b/D = 0.51$ at $M_\infty = 0.8$ and $NPR = 5.0$	57

AN IMPROVED ANALYTICAL MODEL OF THE SEPARATED REGION ON BOATTAIL NOZZLES AT SUBSONIC SPEEDS

by

Walter M. Presz Jr., Ronald W. King and John D. Butea

Pratt & Whitney Aircraft, East Hartford, CT 06108

SUMMARY

Boundary layer flow separation often occurs on the afterbody of aircraft, increasing drag and decreasing performance. Although the separation phenomenon is theoretically understood, the complexities of the governing equations limit solutions to simplified flowfields. Because present methods of predicting and analyzing afterbody flow separation are not reliable, the current program was undertaken.

A practical engineering calculation has been developed to model the viscous effects of a separated, reverse-flow region on afterbody pressures and drag. This viscous calculation is designed to be iteratively coupled with any existing inviscid-flow calculation through an aerodynamic interface. A standard boundary layer displacement thickness is used to modify the afterbody shape where the flow is attached. A discriminating streamline calculation is developed to account for the displacement effects of the reverse flow in separated regions. The discriminating streamline calculation includes the effects of skin friction, axial pressure gradients, and jet entrainment. Skin friction was found to have little effect on the shape of the discriminating streamline. Axial pressure gradients and jet entrainment effects, however, do drastically change the shape of the discriminating streamline from the conical shape previously used.

The viscous flow calculation was coupled to a potential flow calculation. Predictions obtained with this computer program were compared with experimental data for afterbodies with solid jet simulators previously tested by NASA. The analysis was found to accurately predict both the magnitude of the measured afterbody pressures and drag and also their variation with Reynolds number, Mach number, and afterbody shape. Predictions for cases with a flowing jet were also compared with a limited amount of available data. The code accurately predicts a double cell reverse flow region near the afterbody-jet juncture, and reasonably predicts the afterbody pressures. Recommendations for new data required to improve the accuracy of the technique predicting the effects of the jet on afterbody pressures and drag are also presented.

INTRODUCTION

Boundary layer separation frequently occurs on the afterbody of jet aircraft, increasing drag and decreasing engine performance. Currently employed methods of predicting and analyzing this phenomenon are not reliable, which handicaps the designer and increases the uncertainties in predicting performance. To ameliorate this condition, this research program was undertaken. The program is based on earlier work conducted by Dr. W. M. Presz of Pratt & Whitney Aircraft and Dr. E. T. Pitkin of the University of Connecticut (ref. 1 & 2).

Boundary layer separation, a fundamental problem of aerodynamics, is caused primarily by two related factors: viscosity and an adverse pressure gradient. Viscosity depletes the momentum of the boundary layer flow in an adverse pressure gradient. At some point, because of the adverse pressure gradient, the flow breaks away from the wall, and a local area of reversed flow is formed. The point along the wall dividing the forward and reverse flows is defined as the separation point.

An exact flow solution for boundary layer separation can theoretically be obtained from the finite difference calculations of the fully turbulent, compressible Navier Stokes equations. The required calculations, however, have only been solved for simplified flowfield cases, and have required such long computer times as to render the approach unrealistic at this time for engineering requirements.

Current engineering techniques for predicting the separation point generally employ only attached boundary layer and inviscid-flow pressure calculations. A usual assumption of these techniques is that both the momentum and pressure gradients normal to the solid boundary contour are negligible in a thin flow region adjacent to the contour. This approximation allows the momentum equations in a direction normal to the contour and several related flow-direction terms of the Navier Stokes equations to be omitted, resulting in the boundary layer momentum equation. The momentum integral equation is simply the integral of the momentum equation through the boundary layer in the normal direction, and is limited, therefore, to the same basic assumptions. When either of these equations is used to calculate boundary layer development on a curved wall, the development is actually for a flat plate with the characteristic pressure distribution of the curved surface superimposed.

Neither the differential boundary layer equations (finite difference) nor the momentum integral equations have been very successful in predicting flow separation (ref. 3). A local singularity in the calculation occurs near the separation point, rendering finite difference techniques in gross error. In addition, all available turbulence models are based on attached boundary layers and become very inaccurate near separation.

The momentum integral equations are inadequate because they require the calculation of a small difference of large numbers as separation is approached. Furthermore, the empirical skin-friction model used in most turbulent momentum integral calculations never reaches zero — and on a smooth axisymmetric surface with a large radius of curvature, the separation point is always associated with a zero wall shearing stress. In addition, the velocity profiles used in the turbulent momentum integral calculations are based on attached boundary layer assumptions, which are unrealistic near separation.

Calculations have shown, however, that with proper assumptions (viz, a priori displacement thickness distribution through separation) the singularity can be eliminated in the finite difference approach and the boundary layer calculations will yield valid approximations to the full Navier Stokes equations. The boundary layer assumptions are not, therefore, the critical limitations for predicting separation. Current techniques for calculating separation have been unsuccessful because separation and the resultant recirculation region drastically alter the afterbody pressure distribution, which in turn significantly alter the position of the separation point. Standard boundary layer techniques that use only the attached boundary layer and inviscid flowfield calculations to predict separation cannot account for this effect.

The engineering approach for predicting flow separation on afterbodies developed during the earlier work (ref. 2) is iterative and combines all four major flowfield components shown in figure 1: the inviscid flowfield, the attached boundary layer, the point of separation, and the separated recirculating-flow region. The iterative scheme first assumes that there is no separation. Based on this assumption, the inviscid flowfield and corresponding pressure distribution on the afterbody are determined. Next the boundary layer development is calculated by a turbulent boundary layer program. The separation point is then determined by a control volume calculation; and a recirculating-flow region is introduced downstream of the separation point.

The streamline separating the external and recirculating flows is called the discriminating streamline and is treated as if it were the boundary of a body extending between the separation point and the reattachment point on the real body. The discriminating streamline in reference 2 is assumed to be straight, and this assumption is used to define the reattachment point. A recirculating-flow velocity profile is assumed and combined with a mass and a momentum balance for the recirculating region to determine the angle this streamline makes with the afterbody at the point of separation.

Once the separation and reattachment points have been determined, the inviscid flowfield is recomputed for the flow over the quasi surface as defined by body contour plus the discriminating streamline. The entire process is now repeated, and the reiterations continued until the solution converges.

Although standard techniques were shown to be capable of accurately calculating the attached boundary layer and the inviscid flowfield, new flow models had to be developed to calculate the point of separation and the recirculating flow. The earlier work (ref. 2) showed that blockage is the dominant effect of a separation region on an afterbody flowfield. Once the point of separation and a discriminating streamline designating the displacement effect of the recirculating region are determined, afterbody pressures and drags can be calculated from an inviscid analysis of an aerodynamic contour defined by the body and the viscous flow displacement thickness of both the attached boundary layer and the recirculation region.

Available experimental pressure data typically indicated a constant pressure region covering the majority of the model-afterbody area between the separation and reattachment points. It was determined from both analysis and data that a conical discriminating streamline would produce the observed constant-pressure region. A conical, discriminating-streamline model was utilized in reference 2.

Although agreement is good between the analyses and data presented in references 1 and 2, available data is limited. Furthermore, the flow calculation developed has several inherent problems in the flow which could limit its application: the discriminating streamline shape is crude and is based on insufficient data; the no-slip wall boundary condition is not accounted for in the recirculation region; and jet entrainment effects are neglected. As a result skin friction forces cannot be calculated through the recirculation region and drag could be inaccurate on an afterbody with a flowing jet. The program described in this report addresses these limitations, and identifies new data required to develop a better flow model for afterbody flow separation.

SYMBOLS

A	-	cross-sectional area
A _j	-	minimum cross-sectional area of afterbody
A _m	-	maximum cross-sectional area of afterbody
b	-	equivalent length of flat plate boundary layer
C	-	constant representing the wake spread rate
C _D	-	afterbody pressure drag coefficient: $\frac{1}{A_m} \int C_p dA$
C _f	-	skin friction coefficient
C _p	-	static pressure coefficient, $(P - P_\infty)/q$
D	-	maximum diameter of model
d _b	-	base diameter of afterbody
d _s	-	sting diameter
H	-	boundary layer shape factor, δ^*/θ_m
h	-	height of discriminating streamline above body surface in the s coordinate system
J _x	-	axial momentum in the X direction for axisymmetric flow
K _x	-	axial momentum in the X direction for two-dimensional flow
L	-	length of model from nose to start of afterbody
ℓ	-	length of afterbody
ℓ ₁	-	width of wake
ℓ ₂	-	width of shear layer
M	-	Mach number
n	-	normal distance from afterbody surface
P	-	local static pressure
P _t	-	local total pressures
q	-	freestream dynamic pressure
R	-	Reynolds number based on distance from nose to start of afterbody
R _{ex}	-	local Reynolds number based on axial distance from model nose
R _{eθ}	-	local Reynolds number based on boundary layer momentum thickness
r	-	radial coordinate system
r _c	-	radius of outer shear layer edge
r _d	-	radius of the discriminating streamline
r _e	-	radius of outer edge of wake
r _j	-	radius of inner shear layer edge
s	-	coordinate system perpendicular to streamline in the recirculating region
s _x	-	surface area defined by the separated-flow region
T	-	static temperature
T _T	-	total temperature
u	-	local axial velocity
u _b	-	maximum reverse flow velocity
u _j	-	inviscid jet velocity
u _e	-	local inviscid velocity
v _c	-	radial velocity at edge of shear
v _e	-	radial velocity at edge of wake
v _j	-	radial velocity of jet

SYMBOLS (Cont'd)

X_o	-	coordinate system parallel to flow streamlines in recirculating region
x	-	axial coordinating system
w	-	local recirculating velocity
α	-	angle at profile inflection point
α_w	-	angle between the afterbody surface and the profile inflection point
β	-	afterbody mean angle
ν	-	kinetic viscosity
δ	-	boundary layer thickness
δ^*	-	boundary layer displacement thickness
γ	-	nondimensional coordinate, $(\gamma_c - \gamma)/\ell_2$
ψ	-	angle of the discriminating streamline
ρ	-	density
σ	-	jet spreading rate parameter
τ	-	local shear stress
θ	-	local flow angle
θ_m	-	boundary layer momentum thickness
ξ	-	nondimensional coordinate, $(\gamma - \gamma_c)/\ell_1$
\vec{n}	-	unit normal vector
\vec{s}_x	-	vector having magnitude equal to the control volume surface area and a direction parallel to the body surface

Subscripts:

1,2	-	station indicators
av	-	average parameter
BODY-	-	along contour
c	-	outer edge of jet shear layer
d	-	along discriminating streamline
e	-	local inviscid flow properties
j	-	inner edge of jet shear layer
n	-	point of minimum pressure on an afterbody
o	-	start of the afterbody
s	-	condition at afterbody separation point
∞	-	freestream condition

PROGRAM DESCRIPTION

This research program conducted under NASA contract NAS1-14462, entitled "An Afterbody Viscous Flow Program", has extended the usefulness and increased the accuracy of the analytical procedure developed earlier by Dr. Presz and Dr. Pitkin. The analysis iteratively combines four major components: the inviscid flowfield, the attached boundary layer, the point of separation, and the separated recirculating flow region. The work described herein improves the recirculating flow model to more accurately predict the effects of separation on axisymmetric nozzle afterbody performance. Previously this analysis had not accounted for the effects of varying density, axial pressure gradients, skin friction, and jet entrainment. These effects are now included.

The technical effort was organized into four tasks. During Task I the straight-line, discriminating-streamline analysis of reference 2 was further developed to include the effects of varying density, pressure gradients, and skin friction. This was accomplished by reformulating the analysis procedure to a discrete control-volume calculation. During Task II an entrainment model was added to the procedure, accounting for jet effects on separation. A viscous-flow computer program was developed during Task III by combining available, attached-boundary-layer and separation-point calculations with the new, discriminating-streamline model. The accuracy of the procedure was assessed during Task IV.

TASK I - EXTENSION OF METHOD TO ACCOUNT FOR SKIN FRICTION EFFECTS

Although the conical discriminating model developed by Dr. Presz and Dr. Pitkin provides a method for realistically predicting separated afterbody pressures and drag (ref. 1 & 2), the procedure has several limitations: separation angles predicted at Mach numbers above 0.8 are too large (see figure 2), and the predicted recompression pressures are often much too high near the afterbody-sting junction (see figure 3). Both of these errors are believed to be due to the effects on the discriminating-streamline shape of variable density, axial pressure gradients, and wall skin friction. The objective of Task I was to correct the deficiencies by developing a discrete-control-volume analysis for the wake which would include these effects.

A conceptual model of the flowfield in the vicinity of a separated afterbody is shown in figure 4 along with the discrete control volume used to calculate the discriminating-streamline shape. The upper surface of the control volume is inclined at an angle ψ with the wall and, since the upper surface is a flow streamline, no mass flux passes through it. The recirculating-flow streamlines are assumed to be source-like in direction, with each streamline having a common origin. This assumption allows a smooth transition from the flow direction on the body to that on the discriminating streamline. The inside walls of the calculation control volume are constructed normal to the streamlines.

Applying the continuity and momentum equations to the axisymmetric control volume, one obtains

$$2\pi \int_0^{h_1} (\rho w)_1 (r_1 + s) ds - 2\pi \int_0^{h_2} (\rho w)_2 (r_2 + s) ds = 0 \quad \text{eq. (1)}$$

and

$$\oint \rho \vec{n} \cdot d\vec{s} = -\frac{C_f}{2} \rho_B u_B^2 (2\pi r_{av}) \Delta X_0 + (\tau_d) 2\pi (r_{av} + h_{av}) \cos \psi_{av} \Delta X_0 = J_{x,2} - J_{x,1} \quad \text{eq. (2)}$$

where

$$J_x \approx 2\pi \int_0^h \rho w^2 \left(\cos \frac{\psi}{h} s \right) (r + s) ds \quad \text{eq. (3)}$$

and

$$\frac{h_1 \psi^2}{r} \ll 1.0$$

$$r_{av} \equiv \frac{r_1 + r_2}{2}$$

$$\psi_{av} \equiv \frac{\psi_1 + \psi_2}{2}$$

$$s \equiv X_0 \theta$$

$$h \equiv X_0 \psi$$

$$h_{av} \equiv (h_1 + h_2)/2$$

The recirculating flow region can be considered a free-shear layer. Nash (ref. 4); and Vasilu (ref. 5) have used the similarity between the velocity distribution of a free-shear layer and the velocity of a jet flow in the analysis of problems involving shear layers associated with boundary layer separation. The free-shear layers encountered here are treated in like manner. Thus, the velocity across the reverse flow regions is assumed to vary as an error function. The exact profile used is a modification of one developed by Korst and Chow (ref. 6) and which has been shown to accurately model isoenergetic turbulent mixing between two compressible streams at constant pressure.

$$\frac{w}{u_e} \equiv \left(1 + \frac{u_B}{u_e}\right) \left(\frac{1 + \operatorname{erf} [\sigma (\theta - \alpha_w)]}{2}\right) - \frac{u_B}{u_e} \quad \text{eq. (4)}$$

$$\sigma \equiv 12 (1 + 23 M_e)$$

$$\theta \equiv \frac{s}{X_0} = \frac{s}{h} \psi$$

Equation (4) represents the recirculating-flow velocity as a function of streamline coordinates s and X_0 . This equation provides a continuous variation in both magnitude and direction for the velocity between the reverse flow at the wall and the inviscid stream velocity. The angle θ represents the velocity direction measured with reference to the local body surface.

The velocity profile is shown in figure 5; the maximum velocity in the reverse-flow direction is u_B . A laminar body layer is superimposed on the reverse-flow region, and is assumed to grow from the trailing edge of the afterbody for a flowing jet and from the reattachment point for a solid sting. The exact solution for laminar boundary layer growth on a flat plate is used for the boundary layer profile, as indicated in figure 5. Again, the angle inclination between the discriminating streamline and afterbody surface is ψ . It is clear from the geometry in the figure that

$$\psi = \alpha_j + \alpha_w \quad \text{eq. (5)}$$

The following relationships for the turbulent shearing stress along the discriminating streamline and the angle α_j can be derived from the tables presented by Korst and Chow (ref. 6).

$$\frac{\tau_d}{\rho_e u_e^2} = \frac{0.1481 - 0.0478 M_e - 0.1278 \frac{u_B}{u_e} + 0.1632 M_e \frac{u_B}{u_e} + 0.3990 \left(\frac{u_B}{u_e} \right)^2}{\sigma} \quad \text{eq. (6)}$$

and

$$\alpha_j = \frac{0.2090 + 0.0226 M_e + 0.3080 \frac{u_B}{u_e}}{\sigma} \quad \text{eq. (7)}$$

Equations 1, 2, and 3 and the remaining defining equations comprise a proper set of three equations with three unknowns: h , α_w , and u_B . Given the point of separation, body shape, and inviscid flow thermodynamic properties in the axial direction, the shape of the discriminating streamline can be obtained. The equation set includes the effects of compressibility, axial pressure gradient, and skin friction.

Figures 6 through 14 were obtained by applying this analysis to nine test cases chosen jointly by NASA and P&WA. These figures show the calculated pressure and separation location of separated flow regions for three afterbody contours at four Mach numbers. This data is from pressure and separation location experiments by Reubush (ref. 7) and Abeyounis (ref. 8), respectively. The results shown in the figures were obtained with an axisymmetric cone-cylinder forebody ($L/D = 8$) tested with various circular-arc afterbodies with solid-plume simulators. The three afterbodies analyzed have mean angles and l/D ratios of 17.0° and 0.8, 13.8° and 1.0, and 11.0° and 1.0. For these calculations the separation location was set equal to the experimental values obtained by Abeyounis and the pressure distributions from experiments by Reubush. In these figures the straight-line predictions based on the reference 2 analysis are also shown for comparison. The discrete control volume results show considerable curvature in the shape of the discriminating streamline and significant variation with separation Mach number. Equivalent separation angles were obtained for the discrete-control-volume results by drawing a conical surface between the point of separation and the predicted flow reattachment point. A comparison of these equivalent separation angles and the reference 9 data is shown in figure 15. As can be seen, the results obtained with the discrete control volume analysis are in better agreement with the data than are the results obtained with the reference 2 analysis.

Figure 16 shows the effects of the skin-friction, axisymmetric-flow, and pressure terms from equations 1 through 7 on the shape of the discriminating-streamline. Four distinguishably different discriminating streamlines are shown: (1) the straight conical streamline determined by the method of reference 2; (2) the predicted streamline, using equations 1 through 7 but neglecting skin-friction, pressure, and axisymmetric-flow terms; (3) the predicted streamline using equations 1 through 7 but neglecting only skin friction and pressure terms; and (4) the predicted discriminating streamline, using equations 1 through 7 both with and without skin-friction terms.

The predicted discriminating streamlines in figure 16 are essentially the same with a $C_f = 0.003$ and with a $C_f = 0.000$. This is consistent with equation 2 where skin-friction and shear-stress term order-of-magnitudes can be compared.

We have from equation 2

$$\frac{\text{skin friction term}}{\text{shear stress term}} = \frac{\frac{C_f}{2} \rho_B u_B^2 (2\pi r_{av})}{\tau_d 2\pi (r_{av} + h_{av}) \cos \psi_{av}}$$

Since

$$C_f \approx \frac{\tau_d}{\rho_e u_e^2}$$

and

$$r_{av} + h_{av} \approx r_{av}$$

$$\cos \psi_{av} \approx 1.0$$

$$\rho_e \approx \rho_B$$

Therefore

$$\frac{\text{skin friction term}}{\text{shear stress term}} \approx \left(\frac{u_B}{u_e} \right)^2 < < 1.0$$

Thus, skin friction effects on the discriminating-streamline shape should be second order, which agrees with results shown on figure 16. Figure 16 also shows, however, that the effect of axisymmetric flow tends to increase the separation angle and, thus, the size of the separation bubble. The pressure-gradient term increases the discriminating-streamline angle in a favorable gradient region and decreases the angle in an adverse gradient region.

A potential flow analysis (ref. 10) was used to calculate the flow over the various discriminating streamlines presented in figure 16. Figure 17 compares the predicted pressures for configuration 1 as functions of axial location. These results show that the discrete-control-volume analysis can accurately predict the effects of separation on afterbody pressures.

Figure 16 shows that even when the skin-friction, axisymmetric, and pressure terms are dropped there is still a considerable difference between the discriminating streamline obtained from equations 1 through 7 and the one presented in reference 2, which was obtained using similar equations but with constant density and a constant separation angle assumed throughout the recirculation flow region. This discrepancy is investigated in the following paragraphs.

By assuming constant density, letting r get very large compared with h (i.e., to approach two-dimensional flow), and dropping the pressure-gradient and skin-friction terms, equations 1 through 7 reduce to

$$X_{0,1} \int_0^{\psi_1} (\rho u)_1 d\theta - X_{0,2} \int_0^{\psi_2} (\rho u)_2 d\theta = 0 \quad \text{eq. (8)}$$

$$\frac{0.1481 - 0.0478 (M_e)_{av} - 0.1278 \left(\frac{u_B}{u_e} \right)_{av} + 0.1632 M_e \left(\frac{u_B}{u_e} \right)_{av} + 0.3990 \left(\frac{u_B}{u_e} \right)_{av}^2}{\sigma} =$$

$$\frac{K_{x,2} - K_{x,1}}{(\rho u_e^2)_{av} \Delta X_o} \quad \text{eq. (9)}$$

and

$$\psi = \frac{0.2090 + 0.0226 M_e + 0.3080 \left(\frac{u_B}{u_e} \right)}{\sigma} + \alpha_w \quad \text{eq. (10)}$$

where

$$K_x \equiv X_o \int_0^{\psi} \rho u^2 (\cos \theta) d\theta \quad \text{eq. (11)}$$

$$X_o \equiv \frac{h}{\psi}$$

Equations 8 through 11 comprise a proper set of equations for calculating the angle of a conical surface rather than a discrete discriminating separation streamline, and are similar to those presented in reference 2. Figure 18 provides a comparison between the results obtained with the simplified equation set which assumes incompressible flow and small-angles, as in reference 2, and those obtained by solving exactly the equations using numerical techniques. The results show that both compressibility effects and errors associated with small-angle assumptions can have a large effect on the predicted discriminating streamline angle.

The complete, exact solutions of equations 1 through 7 have been programmed and coded for one part of the complete separation analysis shown in figure 19. For the remaining components, existing flow calculations are used. A user's manual for the computer program developed is presented in the appendix.

TASK II - INCLUSION OF JET ENTRAINMENT EFFECTS

During Task II, the analytical model developed during Task I was extended to include jet entrainment effects, which are neglected by currently utilized models. The normal procedure has been to remodel the jet by using a solid sting, a procedure that can lead to large drag errors (ref. 11).

Two approaches for analyzing the separation bubble-jet shear-layer region were examined during Task II. The first and simpler of the approaches was to determine the magnitude of the entrainment effects on the calculation procedure by imposing a slip-velocity and a shearing term at the trailing edge of the afterbody. (See figure 20). This method can be expected to express the jet effects quite accurately near the afterbody trailing edge. However, as the jet mixing layer grows and affects the profile of the recirculating region, the method becomes increasingly in error. As shown in figure 21, the effect of the jet shearing term on afterbody pressure is quite large. Thus, neglecting the jet mixing layer cannot be justified. For this reason the second approach was developed. The second approach is more complete and includes the jet mixing layer.

The model for the second approach assumes an incompressible, turbulent boundary layer and that the radial pressure gradients are negligible. By satisfying integral forms of the equations of motion, the developed procedure calculates shape parameters for an assumed mean-velocity-profile.

The discriminating streamline is then calculated and used as input for the inviscid-flowfield calculation procedure. Communication of jet entrainment to the separated flow over the nozzle afterbody is assumed to take place by means of changes in the inviscid flowfield that result because of the effects of jet entrainment on the discriminating streamline.

The schematic shown in figure 22 represents the flowfield assumed for a nozzle afterbody with both separated flow and a high-pressure jet. The separation bubble exists beyond the nozzle exit plane and consists of two recirculation zones. One recirculation zone is associated with the freestream flow; the other with the jet-stream flow.

A schematic of the flow model used to simulate the flowfield of the jet separation bubble is shown in figure 23. The viscous region is assumed to consist of two parts: a jet shear layer and a separation bubble wake. Velocities at the outer and inner edges of the viscous region are assumed to be equal to the inviscid freestream velocity and to the inviscid jet velocity, respectively. The minimum velocity of the profile is assumed to be at the interface of the jet-shear layer and the separation wake. The discriminating streamline for the freestream flow must exist between the outer edge and inner radius of the wake region.

The velocity profile selected to simulate the viscous region is shown in figure 24. The profile consists of two turbulent mixing layers which treat the minimum velocity as a counter flowing stream. The expressions describing the velocity profiles are modifications of the polynomial function used extensively by Abramovich (ref. 12).

For the jet shear layer $-(r_j \leq r \leq r_c)$

$$u = -u_B + \Delta u_j (2\eta^{1.5} - \eta^3) \quad \text{eq. (12)}$$

where

$$\begin{aligned} \Delta u_j &= u_j + u_B \\ \eta &= \frac{r_c - r}{l_2} \end{aligned}$$

For the wake region $-(r_c \leq r \leq r_e)$

$$u = -u_B + \Delta u_e (2\xi^{1.5} - \xi^3) \quad \text{eq. (13)}$$

where

$$\begin{aligned} \Delta u_e &= u_e + u_B \\ \xi &= \frac{r - r_c}{l_1} \end{aligned}$$

One additional geometric parameter is shown in figure 24: the radius of the discriminating streamline (r_d).

Two of the governing equations for the jet entrainment model were obtained by integrating the differential forms of the equations of motion and applying the Leibniz formula to the integrals.

The resulting continuity equation for the viscous flowfield is

$$\frac{\partial}{\partial x} \int_{r_j}^{r_e} ur \, dr + u_j r_j \frac{dr_j}{dx} - u_e r_e \frac{dr_e}{dx} + v_e r_e - v_j r_j = 0 \quad \text{eq. (14)}$$

Assuming that the incompressible form of Bernoulli's equation is applicable results in the following expression for the axial momentum equation

$$\frac{\partial}{\partial x} \int_{r_j}^{r_e} u^2 r \, dr + u_j^2 r_j \frac{dr_j}{dx} - u_e^2 r_e \frac{dr_e}{dx} + u_e v_e r_e - \frac{r_e^2}{2} u_e \frac{du_e}{dx} = 0 \quad \text{eq. (15)}$$

Two additional equations were added to the equations of motion to complete the set of governing equations. One equation is the continuity equation for the shear layer

$$\frac{\partial}{\partial x} \int_{r_j}^{r_c} u r dr + u_j r_j \frac{dr_j}{dx} - u_c r_c \frac{dr_c}{dx} + v_c r_c - v_j r_j = 0 \quad \text{eq. (16)}$$

where $v_c \equiv$ radial velocity at the outer edge of the shear layer

The other equation is the continuity equation for the discriminating streamline

$$\frac{\partial}{\partial x} \int_{r_j}^{r_d} u r dr + u_j r_j \frac{dr_j}{dx} = 0 \quad \text{eq. (17)}$$

Using the assumed velocity profile with the governing equations results in the following set of eight unknowns

$$\frac{du_B}{dx} \equiv \text{axial rate of change of the minimum velocity}$$

$$\frac{dr_j}{dx} \equiv \text{slope of inner edge of shear layer}$$

$$\frac{d\ell_2}{dx} \equiv \text{spreading rate of the shear layer}$$

$$\frac{d\ell_1}{dx} \equiv \text{spreading rate of the wake}$$

$$\frac{dr_d}{dx} \equiv \text{slope of the discriminating streamline}$$

$$v_e, v_j, v_c \equiv \text{radial velocities at points within the viscous region.}$$

Since there are eight unknowns and only four equations, four additional conditions have to be specified to obtain a solvable set of equations.

Since the jet shear layer is assumed to dominate the viscous flowfield, three of the necessary closure conditions relate to the characteristics of the shear layer. The first assumption is that the shear layer spreads at a constant rate, as suggested by Abramovich (ref. 12).

$$\frac{d\ell_2}{dx} = 0.25 \quad \text{eq. (18)}$$

The second assumption is that the radial velocity at the inner edge of the shear layer is zero.

$$v_j = 0 \quad \text{eq. (19)}$$

The third closure condition is that the net flow through the outer edge of the shear layer is defined by

$$-u_b r_c \frac{dr_c}{dx} + v_c r_c = k u_j r_c \quad \text{eq. (20)}$$

where k is a constant whose value is selected to maintain a continuous discriminating streamline slope at the initial jet entrainment station.

The final closure condition assumes that the outer wake region has a constant spreading rate. The value of the spreading rate is assumed to be given by

$$\frac{d\ell_1}{dx} = \left. \frac{dr_b}{dx} \right|_e + 0.25 = C \quad \text{eq. (21)}$$

where $\left. \frac{dr_b}{dx} \right|_e \equiv \text{slope of the nozzle afterbody at the nozzle exit.}$

TASK III – DEVELOPMENT OF A VISCOUS FLOW COMPUTER PROGRAM

A computer subroutine package was developed during Task III. This package, called VISCUS, calculates boundary layer flow separation by utilizing the procedures previously described and by interfacing them with existing programs that calculate the external inviscid flow. The subroutine package is described in the appendix.

To define the equivalent aerodynamic contours of afterbodies with separated flow, the discriminating-streamline wake calculations of Tasks I and II were combined with:

- 1) a separation point prediction method
- 2) a modified Reshotko-Tucker boundary layer analysis (ref. 13).
- 3) a displacement thickness, inviscid flow, interface calculation for attached boundary layers.

The calculation procedure, shown schematically in figure 25, was developed for iterative matching with an existing inviscid flow procedure. The viscous flow procedure calculates the aerodynamic contour based on a given flow-pressure distribution, and the inviscid procedure calculates the pressure distribution based on the aerodynamic contour. The iteration between the two calculations continues until the aerodynamic contour and the pressure distribution are in equilibrium.

The basic assumptions in the analysis are: 1) the inviscid or external flowfield imposes its axial pressure field on the boundary layer and separation region, and 2) the normal pressure gradients in the boundary layer and separation region are not important. The following paragraphs describe each of the major components of the VISCUS subroutine.

Separation Point Prediction

The VISCUS subroutine package provides the "user" with four options for calculating the separation: Stratford's criterion, Page's criterion, Goldschmied's criterion, and the control volume criterion.

Stratford's Criterion (ref. 14) — This approach is based on an approximate solution of the equations of motion; a single empirical factor is required. The equations are integrated using a modified inner and outer solution technique. It is assumed that the outer part of the boundary layer is affected only by the initial velocity profile and the downstream pressure gradient, and the inner part of the boundary layer is locally in equilibrium and is independent of upstream conditions. At a Reynolds number of the order of 10^6 , the criterion is:

$$C_{p,s} [bd (C_{p,s})/db]^{1/2} = 0.98 (Re_b)^{0.1} \quad \text{eq. (21)}$$

The distance b represents an equivalent length of flatplate, constant-pressure boundary-layer growth. Re_b is the Reynolds number based on this equivalent length.

Page's Criterion (ref. 15) — This is probably the most commonly used approach for prediction of the local separation point. The recirculation region is modeled as a base-type region and entrainment equations for constant pressure viscous mixing are used to derive an equilibrium pressure. In its original form for subsonic flow, the criterion $C_s = 0.38$ where C_s is a modified separation pressure coefficient defined as

$$C_s = (2(P_s - P_\infty)/\gamma P_s M_s^2) \quad \text{eq. (22)}$$

Eilers (ref. 16) modified this criterion for use on axisymmetric afterbodies where the boundary layer goes through a strong expansion before recompressing to a separated region. This modified version, which will be used herein, is $C_s = C_n + 0.38$, where C_n is defined as

$$C_n = (2(P_n - P_\infty)/\gamma P_n M_n^2) \quad \text{eq. (23)}$$

The subscript n indicates reference to the point of minimum pressure on the afterbody.

Goldschmied's Criterion (ref. 17) – This criterion was originally derived for planar incompressible flow. The criterion is based on a line of constant total pressure occurring in a boundary layer, even under an adverse pressure gradient. At separation the height of the constant pressure line and the laminar sublayer are equal. The resulting criterion becomes $C_{p,s} = 200 C_{f,n}$ where $C_{f,n}$ is the skin friction coefficient at a minimum pressure point on the afterbody. This separation prediction technique is independent of the pressure distribution downstream of the minimum pressure point and is dependent on Reynolds number and Mach number only through the skin friction coefficient.

Control Volume Criterion (ref. 18) – A control volume in the boundary layer between the minimum pressure point and the point of separation on the afterbody is used. Conservation of mass and momentum through the volume, along with the compressible law of the wall law of the wake boundary-layer profiles are used to calculate the separation pressure.

Boundary Layer Analysis

The attached, turbulent boundary layer is calculated using an integral approach. The need to assume something explicitly about the local Reynolds stresses is eliminated by integrating the flow equations across the boundary layer. In this manner, the following momentum integral equation is derived.

$$\frac{d\theta_m}{dx} = \frac{C_f}{2} - \theta_m \left[\frac{1}{\rho_e} \frac{d\rho_e}{dx} + \frac{1}{u_e} \frac{du_e}{dx} (2 + H) + \frac{1}{r} \frac{dr}{dx} \right] \quad \text{eq. (23)}$$

A solution of this momentum integral equation for turbulent boundary layers is obtained using the approach and equations of Reshotko and Tucker (ref. 13). An approximate shear integral obtained by a correlation of extensive data in an adverse pressure gradient is employed (ref. 19).

Aerodynamic Interface

An aerodynamic contour is calculated by adding a displacement thickness to the basic contour where the boundary layer is attached and to the discriminating streamline where the flow is separated on the afterbody. The contour is then smoothed between each iteration.

The smoothing routine uses finite difference equations with a Taylor series expansion to determine, among other properties, the curvature at the midpoint of each five point interval describing the body. Curvature is calculated both with and without the midpoint. When the curvature is larger with the midpoint not included, the curve is under-constrained with the four points. Smoothing or moving the centerpoint would significantly alter the local characteristics of the curve near the midpoint and, therefore, no smoothing occurs. If the curvature is smaller with the midpoint, the midpoint is adjusted in a systematic manner to increase the curvature. Thus, a numerical model with a smooth, continuous, second derivative is assured. All sharp corners or slope discontinuities are faired out.

TASK IV - ASSESSMENT OF ACCURACY OF METHOD

The afterbody viscous flow calculation from Task III was interfaced with an existing, inviscid, potential-flow program that uses a combination of the Neumann method, (ref. 10) and the Labrujere compressibility correction (ref. 20). The complete analysis was applied to several afterbody contours and flow conditions, and the results compared with available data to determine the accuracy of the calculation methods. The test cases included fifteen chosen jointly by NASA and Pratt & Whitney Aircraft. The comparisons, discussed below, have been divided into afterbody flowfields with solid-plume simulators and afterbody flows with a jet: the solid-plume comparisons relate to Task I calculations; the flows with jets, to Task II calculations.

Solid Plume Results

A jet exhaust plume affects afterbody boattail pressures in two ways: through blockage and through entrainment. A significant amount of data for separated afterbody contours has been recently obtained by using solid jet simulators, or rearward stings (ref. 7, 8, 9, 11, 21 and 22). Although this type of jet simulator accounts for only the blockage effect of a jet, it does provide a useful media for studying the separation region over an afterbody, including the reattachment zone on the sting. A study of the accuracy of the analytical prediction methods developed in Task I was determined using this data. This study included variations in afterbody pressures and drag as a function of Reynolds number, Mach number, afterbody contour, and separation location. Results obtained by varying each of these parameters will be discussed in the following paragraphs.

A thorough experimental study of afterbody pressures and drag as a function of Reynolds number has been conducted by NASA (ref. 21) in the NASA-Langley 1/3-meter cryogenic tunnel. A comparison of the analytically predicted pressures with data from these tests are shown in figure 26 for a circular arc-conic afterbody at a Mach number of 0.601 and a Reynolds number of 4.29×10^7 . The upper part of the figure presents the afterbody contour. Several iterations of the pressures predicted by the analysis are presented. In the first iteration, the calculation procedure solves for pressures over the actual contour without a boundary layer. A boundary layer displacement thickness is used to modify the afterbody contour on all subsequent iterations. In the third iteration, the procedure solves for the pressures over the afterbody contour modified to also include a constant-pressure discriminating separation streamline. In the fifth and subsequent iterations, the procedure solves for the pressure over the afterbody with the discrete discriminating streamline calculated to include the effects of skin friction and pressure gradients. The separation point is averaged with the previous value, and the thickness of the boundary-layer displacement is averaged with the previous two values after the fifth iteration. (See appendix for details of this iteration procedure.) The convergence shown in figure 26 is excellent after seven iterations for both predicted pressure distribution and separation-point location. The separation point results produced in figure 26 are based on the control volume technique. Since the same results were observed after the seventh iteration in other applications of the analysis, the iteration scheme was set to fix the separation point at the value predicted during the seventh iteration. This scheme accelerates convergence of the boundary layer, minimizes instabilities in calculations for more severely separated contours, and provides the best comparisons with available data.

A comparison of the results from the final (i.e., tenth) iteration with data for the same body is shown in figure 27. The agreement between analysis and data is excellent. The largest differences between predicted and measured pressures are over the initial portion of the afterbody ($x/D = 0$ to 0.2); the reason for the discrepancy is not clear. The pressures in the highly viscous flow region at the trailing edge of the nozzle are matched quite well. A comparison of measured and predicted pressure drag (also shown in figure 27) shows that the prediction is higher than the measured pressure drag. This result has to be function of the pressure discrepancies over the initial portion of the afterbody.

Figure 28 presents a comparison of measured and predicted pressures and drags over this same afterbody at the lower Reynolds number of 2.61×10^6 . The wide variation in Reynolds number in the data was obtained using the NASA Langley 1/3-meter cryogenic tunnel. Again, agreement between analysis and data for the pressures is excellent except near the onset of the afterbody. The analysis predicts the weaker expansion and recompression on the afterbody, which occurs at this lower Reynolds number and also that the separation point moves downstream with increasing Reynolds number. The pressure drag is again over-estimated. In comparing figure 27 and 28, the analysis predicts a slight decrease in afterbody pressure drag with Reynolds number, and the data verifies this trend.

Separated afterbody pressures have been measured on a full circular-arc afterbody ($l/D = 0.80$ and $d_b/D = 0.51$) at several freestream Mach numbers (ref. 7 and 11) and a comparison of the predictions with the data is shown in figures 29, 30, and 31 for Mach numbers of 0.4, 0.6, and 0.8, respectively. The agreement between analysis and data is excellent at a Mach number of 0.4 and is good at 0.6 and 0.8. The analysis predicts that with an increase in Mach number there will be an increase in expansion, an upstream separation point movement, and an increase in drag; these predictions are all verified by the data. At the higher Mach numbers the recompression pressures are slightly overestimated by the analysis. The major reason for this discrepancy is in the separation-point calculation. This is emphasized in figure 32 where the pressures over the afterbody are again predicted by the analysis at a Mach number of 0.6, but with the separation point fixed at the experimental value. The agreement between analysis and data becomes much improved, substantiating that the separation point calculation is the major sources of error for existing discrepancies between analysis and data.

Additional comparisons were made for several different contours, and these results are presented in figures 33 through 37. Figure 33 shows predicted results for a circular-arc afterbody having an $l/D = 1.0$ and a $d_b/D = 0.61$ (ref. 24) at a Mach number of 0.8. Although the predicted separation location is slightly too far upstream, agreement between predicted and measured pressures is excellent.

Figure 34 presents the results for a circular-arc, conical afterbody that was tested by Shrewsbury (ref. 23) and which has a ratio of radius-of-curvature to maximum-diameter of 0.5 and a ratio of afterbody-length to maximum-diameter of 0.5715. This afterbody contour is very nearly conical, as can be seen in the upper portion of figure 34. The measured pressures near the juncture of the afterbody and the maximum diameter indicates a very rapid, localized expansion region. The analysis drastically under predicts this expansion region. Since this area is far upstream of any separation point or viscous region, this discrepancy

appears to be due to limitations of the inviscid flowfield calculation or the contour smoothing employed. Further downstream near the junction of the afterbody and sting, the analysis accurately predicts the pressures.

A comparison of predicted and measured pressures is presented in figure 35 for a full circular-arc afterbody having a $L/D = 8.0$, and $\ell/D = 1.0$, and a $d_b/D = 0.51$ at a Mach number of 0.798—the contour is shown in the top of the figure. The agreement between both predicted and measured pressures is again excellent. This figure also shows the effect on the predicted pressures as the separation point is artificially moved. When the separation point is moved downstream $\Delta x/D = 0.05$ from the experimental value, too much recompression near the sting-afterbody juncture and relatively little difference in afterbody drag results. When the separation point is moved upstream $\Delta x/D = 0.05$ from the experimental value, less recompression near the afterbody juncture and an increase in afterbody drag results. These results emphasize the importance of accurately predicting separation point location when using a patched inviscid, viscous interaction procedure for estimating afterbody pressures and drag.

Jet Plume Results

During this portion of Task IV, the accuracy of the jet-entrainment model developed under Task II was assessed. Because detailed information is not currently available for jet/separation bubble interaction flowfields, the accuracy had to be checked indirectly. This was accomplished by using the wake entrainment model to predict the effect of jet entrainment on afterbody pressures and comparing the results with data. The model was incorporated into the afterbody calculation analysis described previously. The procedure was then applied to five of the test cases chosen jointly by NASA and Pratt & Whitney Aircraft. Experimental data for the test cases—which included variations of nozzle pressure and free-stream Mach number—were obtained from an earlier NASA experimental study (ref. 11 and 22).

The iteration procedure used for analysis of the jet entrainment effects was identical to the one used for the solid-jet simulator analysis, except the jet entrainment model was used to calculate the discriminating streamline downstream of the nozzle exit. The inviscid core of the jet plume was assumed to be independent of the external flowfield, and the shape was assumed to be identical to that of an inviscid jet issuing into a quiescent atmosphere.

The effect of jet entrainment on the discriminating streamline of a separation region is shown in figure 36. A comparison is presented for discriminating streamlines calculated for flow over a circular-arc afterbody at a Mach number of 0.6 and a nozzle total pressure ratio of 2.91. The dashed line is the calculated discriminating streamline, assuming the inviscid core to be a solid sting, thus accounting for plume blockage only. The solid line is the discriminating streamline calculated with jet entrainment included. The separation point was not allowed to change for these calculations and was set equal to the experimentally observed separation point. A significant difference in the two streamlines can be seen at the end of the recirculating zone. In figure 37 the afterbody pressures calculated by the two modes are compared. These results indicate that the differences between the two discriminating streamlines downstream of the nozzle exit has a small effect on the afterbody pressures, implying that the mixing layer assumed

to grow along the discriminating streamline dampened out the effects of streamline variations near the end of the separated region. The results of the application of the analysis to the five test cases is presented in figures 38 through 42. The separation point was computed for these cases and was fixed at the value predicted in the seventh iteration. The shape of the discriminating streamline was also set as that calculated during the seventh iteration with subsequent iterations used to settle out the boundary layer superimposed upon the discriminating streamline. The afterbody configuration analyzed for all of the test cases was a circular-arc afterbody with $\ell/D = 0.80$ and $d_b/D = 0.51$. Figures 38 and 39 present comparisons of analytical results with experimental data for a nozzle pressure ratio of 2.9 and Mach numbers of 0.6 and 0.8, respectively. Figures 40 and 41 present a similar Mach number variation for a nominal nozzle pressure ratio of 2. Figure 42 presents the comparison for a Mach number of 0.8 and a pressure ratio of 5. A good comparison between predicted and experimental separation point can be observed for all cases. In all the comparisons the predicted measured pressure is good except right near the nozzle trailing edge.

When a nozzle jet interacts with an external flowfield, the effective inviscid jet contour is changed (ref. 24) from what it would have been in a constant-pressure environment. Since all the results presented herein were based on an inviscid jet contour expanding into a constant-pressure environment, the calculations neglected suppression on the inviscid jet contour. And this could account for the small jet effects on the predicted afterbody pressures. Development of an iteration scheme that includes coupling with the calculation of the inviscid plume should be undertaken before further assessing the accuracy of the model.

RECOMMENDATION FOR NEW DATA REQUIRED

The primary area of uncertainty in the afterbody viscous flow calculation is the jet entrainment model. The analysis includes all the physics of the flowfield believed to be important, and yields a recirculation region that is consistent with available flow visualization and with intuition. Even so, pressures over the separated afterbody with a flowing jet represents the largest area of disagreement between calculation results and data. To resolve this problem, new data is required for improved calibration of the calculating procedure and for checking current assumptions made in the jet entrainment model.

Calibration of the jet entrainment model requires test data that will enable refinement of the empirical-closure assumptions used to complete the set of governing equations. The specific closure assumptions that have to be refined are the spread and entrainment rates of the shear layer and the spread rate of the outer wake. To adequately define effective models for these flow characteristics, an elaborate test program is required.

The program should be designed to define the separation-bubble, jet-entrainment region for axisymmetric nozzle afterbodies with high-pressure air jets. Variations of the flowfield with Reynolds number, Mach number, nozzle pressure ratio, and afterbody shape should be defined.

The jet separation bubble interaction region should be mapped using optical techniques to provide measurements of the pertinent flow characteristics. Use of conventional rake and probe or hot wire instrumentation is not recommended because the presence of the measurement device can significantly affect the flowfield in the recirculation region.

SUMMARY OF RESULTS AND RECOMMENDATIONS

The conical discrimination streamline calculation for separated flows developed earlier by Presz and Pitkin (ref. 1) was extended to include effects of large separation angles, variable density, skin friction, and axial pressure gradient. Skin friction within the recirculating flow region was found to have a second order effect on the separated streamlines while pressure gradients were found to add a little curvature to the discriminating streamline shape without drastically affecting its mean angle. The constant-density, small-angle assumption originally used in developing the conical discriminating streamline calculation was found to be a primary reason for discrepancies between analysis and data at high subsonic Mach numbers. With these effects accounted for in the separation model, the analysis predicts the extent of the separation region on afterbody-sting models quite accurately for the data available.

The discriminating streamline calculation was extended to also include jet entrainment effects on the separation region. A wake-jet profile capability downstream of an afterbody was incorporated into the analysis. In this manner, jet entrainment was found to change the separation region on an afterbody from a single recirculating flow to a double counter-rotating, recirculating flow. This results in the jet sucking down the discriminating streamline and drastically changing its shape downstream of the afterbody jet exit.

The extended discriminating streamline calculation was combined with an attached-boundary-layer calculation, a separation point prediction, and an inviscid flow calculation. The complete analysis was applied to several separated afterbodies. The analysis accurately predicts the pressures and drag as a function of Reynolds number, Mach number, and afterbody shape for the comparisons made with data from afterbody-sting models tested by NASA. Thus the analysis provides an engineering approach for predicting nozzle afterbody drags. The small discrepancies found between analysis and data most likely result from inaccuracies in the separation point prediction, not the recirculating flow model.

The limited comparisons of predicted and measured pressures over afterbodies with a flowing jet are encouraging. The predictions were made with the inviscid plume shape fixed. These calculations should, however, be repeated with a scheme to iterate between the external flow and the plume. The change in plume shape caused by the high pressures near the afterbody-jet junction should improve agreement between analysis and data.

In closing, the viscous flow subroutine present herein provides a useful engineering tool for predicting pressures and drags over separated afterbodies. The coupling of the viscous flow subroutine to an inviscid flow calculation is highly sensitive, and extreme care should be used when exercising the analysis.

Langley Research Center
National Aeronautic and Space Administration
Langley Station, Hampton, Va., 28 June 1977

BLANK PAGE

REFERENCES

1. Presz, W. M. and Pitkin, E.: "Flow Separation Over Axisymmetric Afterbody Models", *Journal of Aircraft*, Vol. 11, Nov. 74, pp. 677-682.
2. Presz, W. M. and Pitkin, E.: "Analytical Model of Axisymmetric Afterbody Flow Separation", *Journal of Aircraft*, Vol. 13, July 76, pp. 500-505.
3. Hahn, M. ; Rubbert, P. ; and Mahal, A.: "Evaluation of Separation Criteria and Their Application to Separated Flow Analysis", Technical Report AFFDL-TR-72-145, January 1973.
4. Nash, H. F.: "An Analysis of Two-Dimensional Turbulent Base Flow, Including the Effect of the Approaching Boundary Layer", R. & M. No. 3344, British A. R. C., 1960.
5. Vasiliu, J.: "Pressure Distribution in Regions of Step Induced Turbulent Separation", *Journal of Aerospace Science*, Vol. 29, 1962, pp. 596.
6. Korst, H. H. and Chow, W. L.: "Non-Isoenergetic Turbulent Jet Mixing Between Two Compressible Streams at Constant Pressure", NASA CR-419, 1966.
7. Reubush, D. E.: "Experimental Study of the Effectiveness of Cylindrical Plume Simulators for Predicting Jet - On Boattail Drag at Mach Numbers Up to 1.30", NASA TN D-7795.
8. Abeyounis, W. K.: "Boundary Layer Separation on Isolated Boattail Nozzles", M. S. Thesis, George Washington University, May 8, 1977.
9. Wilmoth, R. G.: "Analytical Study of Viscous Effects on Transonic Flow Over Boattail Nozzles", AIAA Paper No. 77-223, July 1977.
10. Smith, A. M. O. and Pierce, J.: "Exact Solution of the Neumann Problem; Calculation of Non-Circulatory Plane and Axial Symmetry Flow About or Within Arbitrary Boundaries", *Proceedings of the Third U. S. National Congress of Applied Mechanics*, Vol. 2 Brown Univ., 1968, pp. 807-815.
11. Putnam, L. E. and Abeyounis W. K.: "Experimental and Theoretical Study of Flow Field Surrounding Boattail Nozzles at Subsonic Speeds", AIAA Paper No. 76-675, 1976.
12. Abramovich, G. M. ; "The Theory of Turbulent Jets", MIT Press, 1963.
13. Reshotko, E. and Tucker, M.: "Approximate Calculation of the Compressible Turbulent Boundary Layer With Heat Transfer and Arbitrary Pressure Gradient", NASA TN-4154, 1957.
14. Stratford, B. S.: "The Prediction of Turbulent Boundary Layer", *J. Fluid Mech.*, Vol. 5, Jan. 59, pp. 1-16.
15. Page, R. H.: "A Theory of Incipient Separation", *Development in Mechanics*, Vol. 1, Plenum Press, N. Y., 1961, pp. 563-577.

REFERENCES (Cont'd)

16. Eilers, R. E.: "Analytical Investigation of Subsonic Separation from Axisymmetric Boattails", Boeing Aircraft Co., D6-20399, A68, 1968.
17. Goldschmied, F. R.: "An Approach to Turbulent Incompressible Separation Under Adverse Pressure Gradients", *Journal of Aircraft*, Vol. 2, March-April 1965, pp. 108-115.
18. Presz, W. M.: "Turbulent Boundary Layer Separation on Axisymmetric Afterbodies", Ph. D. Thesis, Univ. of Connecticut, 1974.
19. Elliot, D. G.; Bartz, D. R.; and Silber, S.: "Calculation of Turbulent Boundary Layer Growth and Heat Transfer in Axisymmetric Nozzles", Jet Propulsion Lab., TR-32-387, 1963.
20. Labrujere, Th. E.; Loeve, W.; and Slooff, J. W.: "An Approximate Method for the Calculation of the Pressure Distribution on Wing-Body Combinations at Subcritical Speeds", Aerodynamic Interface, AGARD-CP-71-71, Sept. 70.
21. Reubush, D. E. and Putnam, L. E.: "An Experimental and Analytical Investigation of the Effect on Isolated Boattail Drag of Varying Reynolds Number Up to 130×10^6 ", NASA TN D-8210, 1976.
22. Reubush, D. E. and Runckel, J. F.: "Effect of Fineness Ratio on the Boattail Drag of Circular-arc Afterbodies Having Closure Ratios of 0.50 With Jet Exhaust at Mach Numbers up to 1.30", NASA TN D-7192, 1973.
23. Shrewsbury, G.: "Effect of Boattail Juncture Shape on Pressure Drag Coefficients of Isolated Afterbodies", NASA TM X-1517, 1967.
24. Grund, E.; Presz, W. M.; Konarski, M.: "Predicting Airframe/Exhaust Nozzle Interaction at Transonic Mach. Numbers," AIAA Paper No. 71-20, June 14-18, 1971.

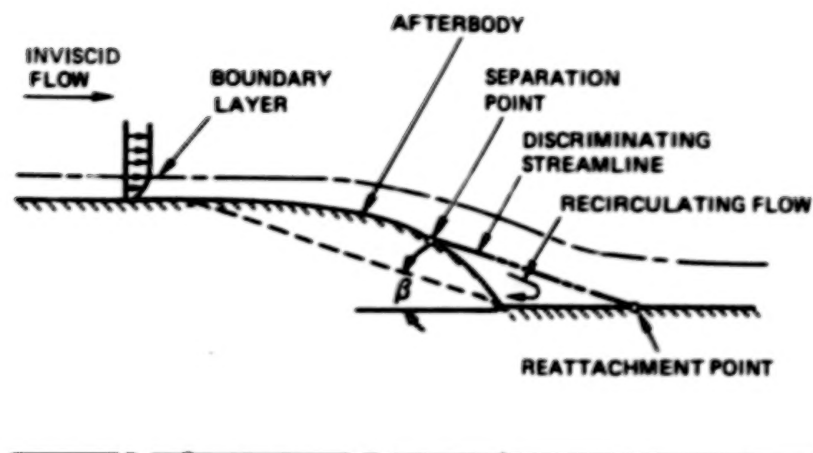


Figure 1 Schematic of the Separated Afterbody Flowfield

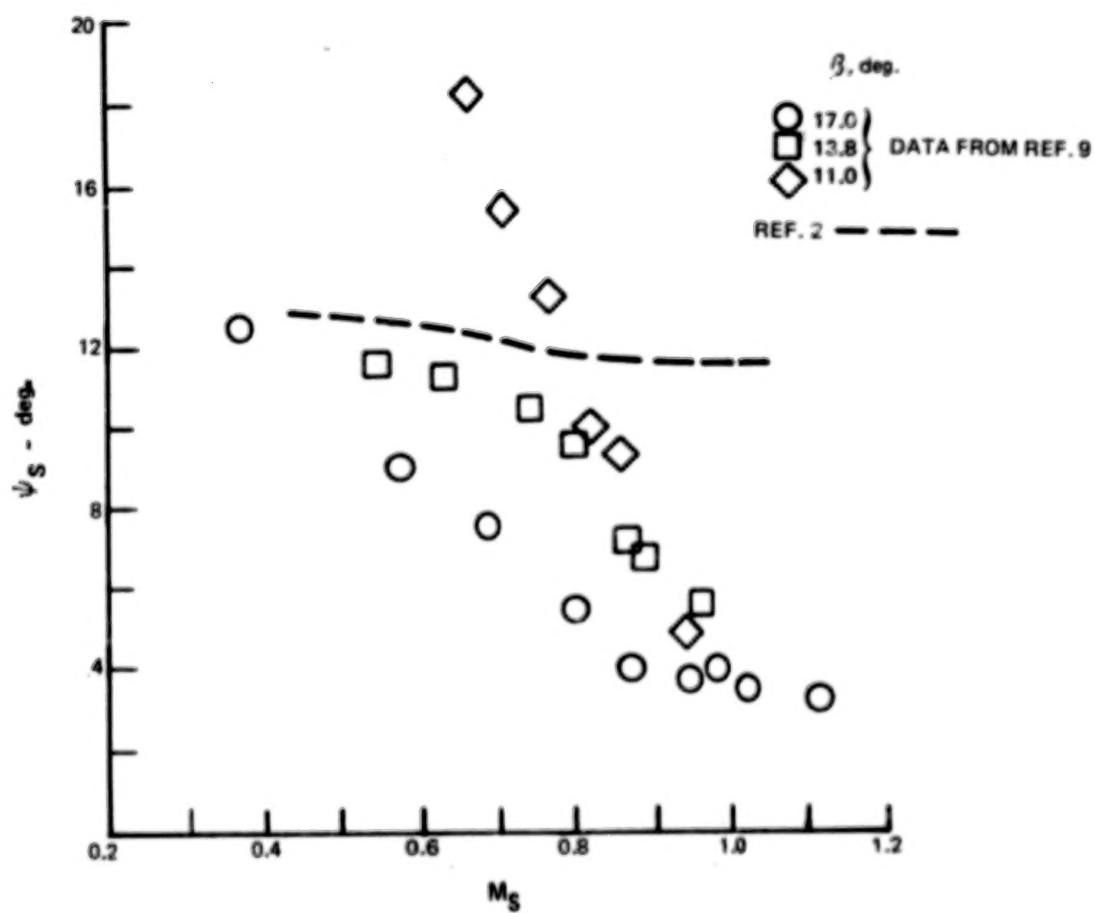


Figure 2 Comparison of Measured and Predicted Separation Angles

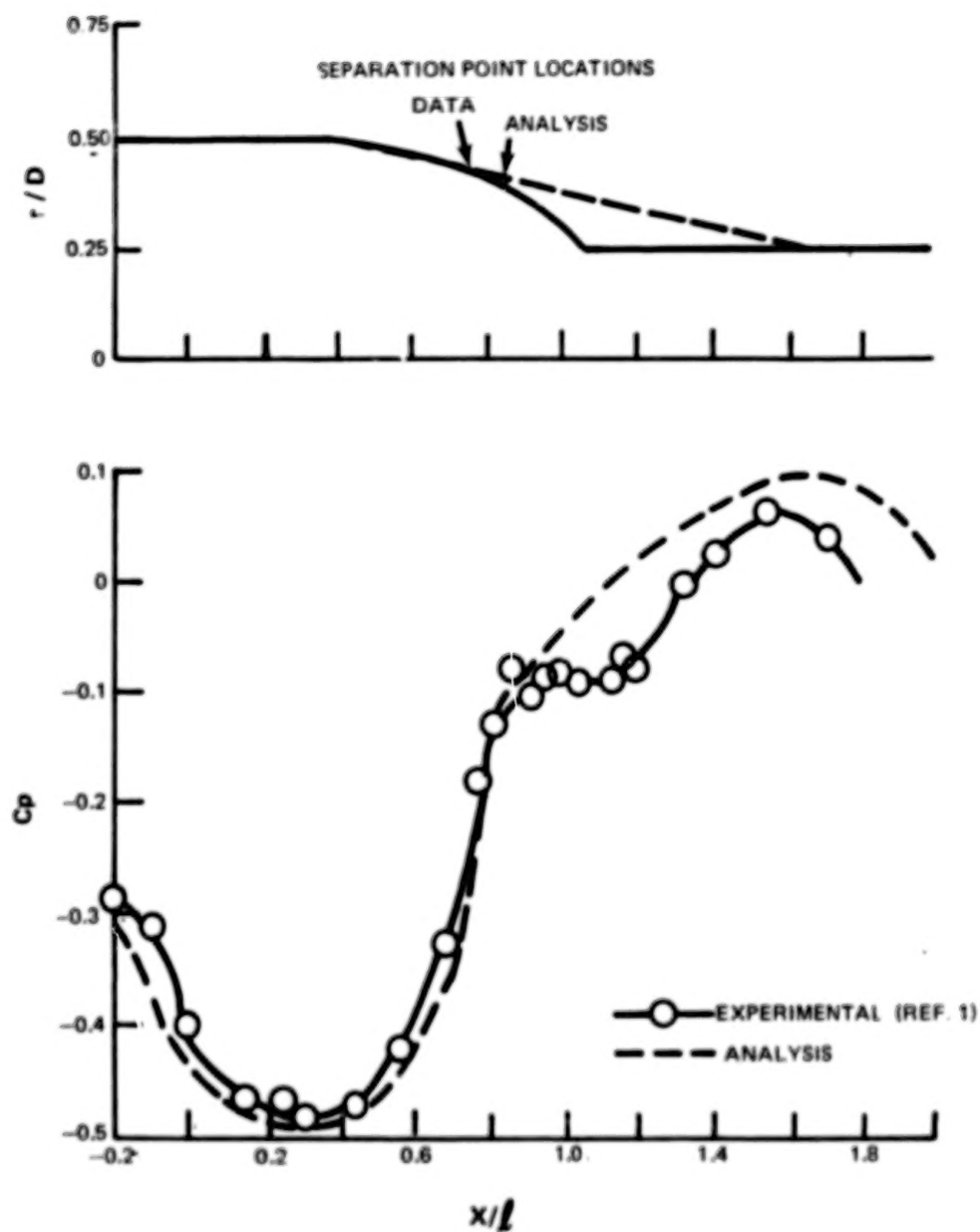


Figure 3 Comparison of Measured and Predicted Pressures on a Separated Afterbody At $M_{\infty} = 0.5$ with $\beta = 16^\circ$ and $(\delta^*/r) = 0.04$

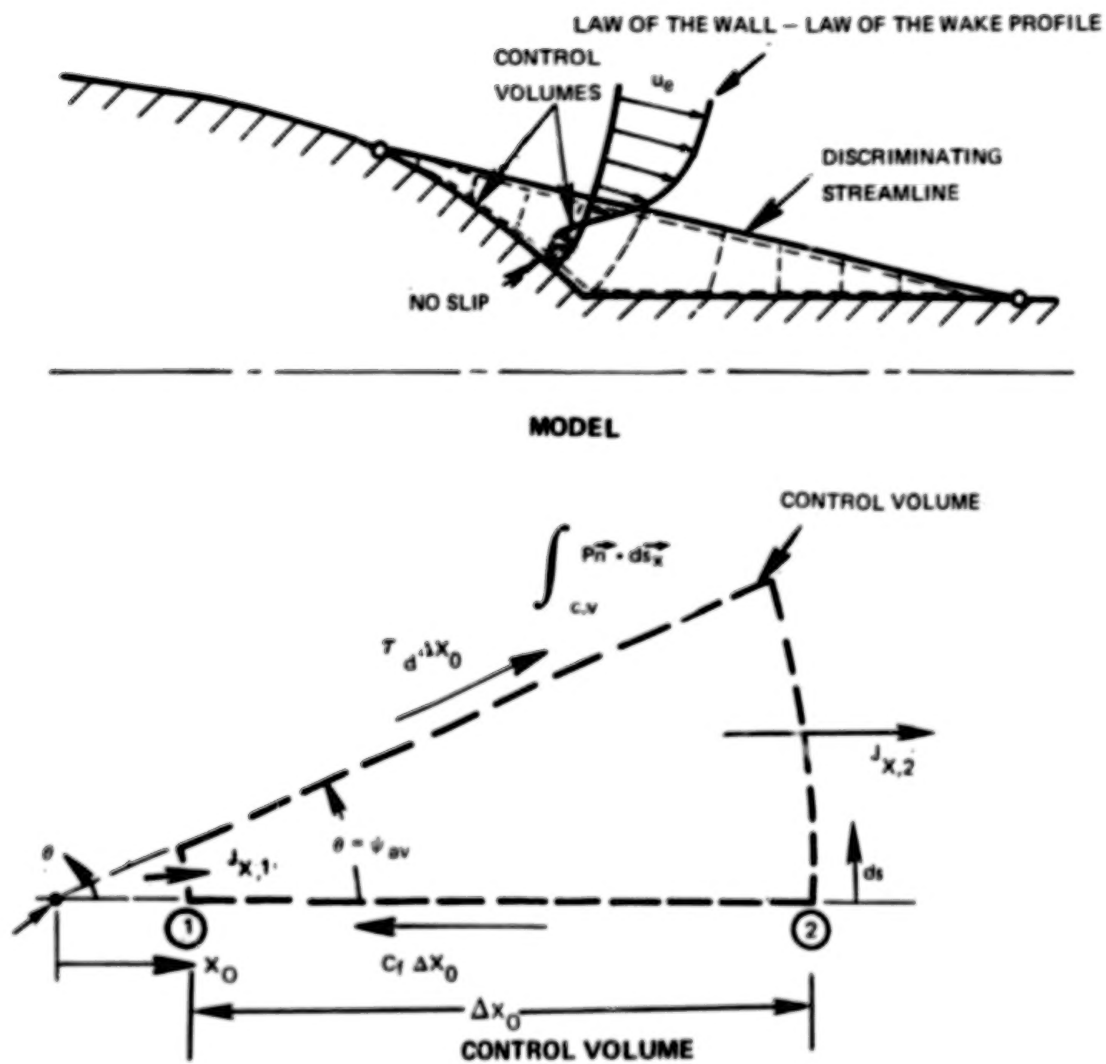


Figure 4 Differential Control Volume Analytical Model

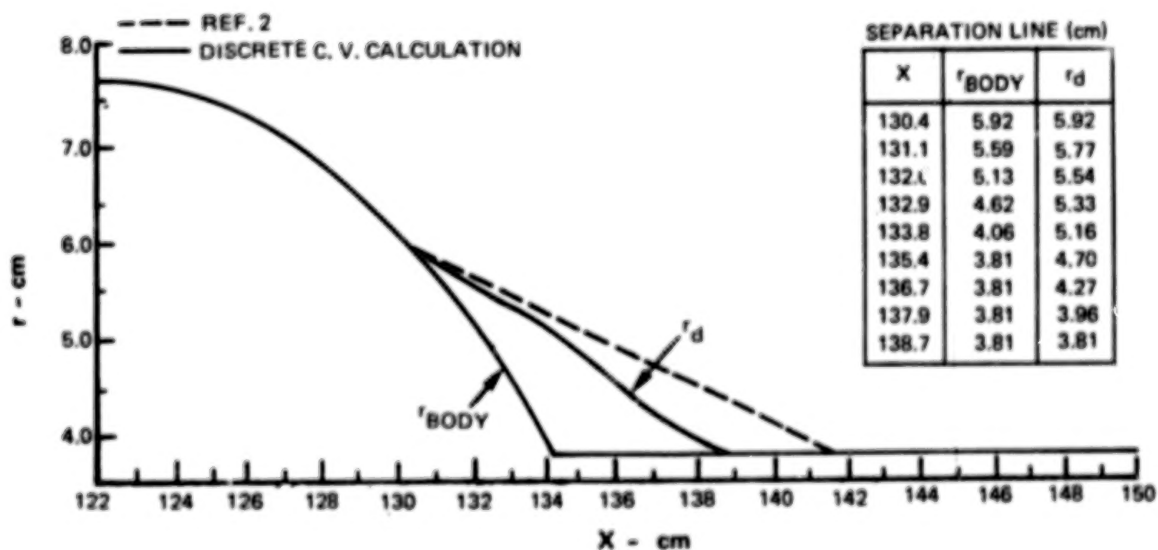
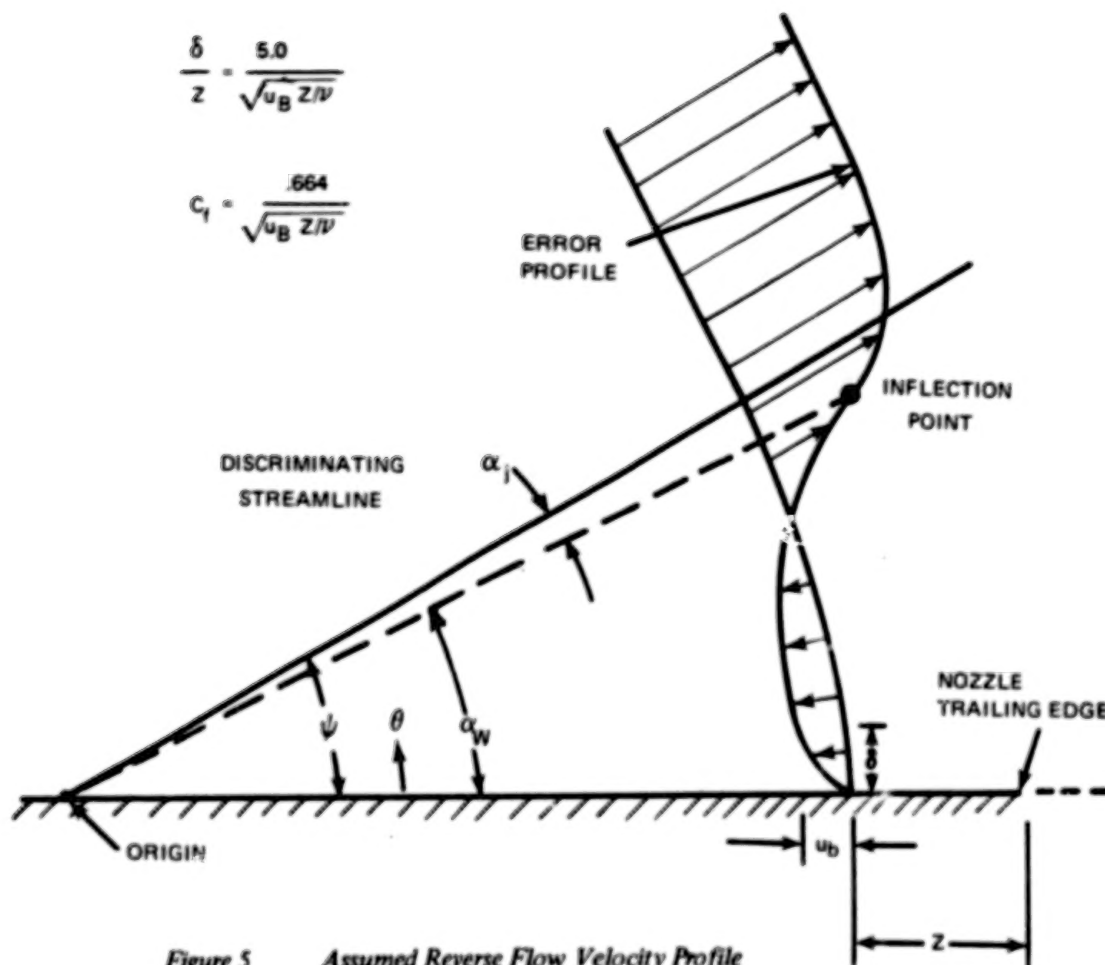


Figure 6 Comparison of Calculated Discriminating Streamline Shapes for Circular Arc Nozzle Configuration With $\beta = 17^\circ$ and $d_p/D = 0.51$ at $M_\infty = 0.6$

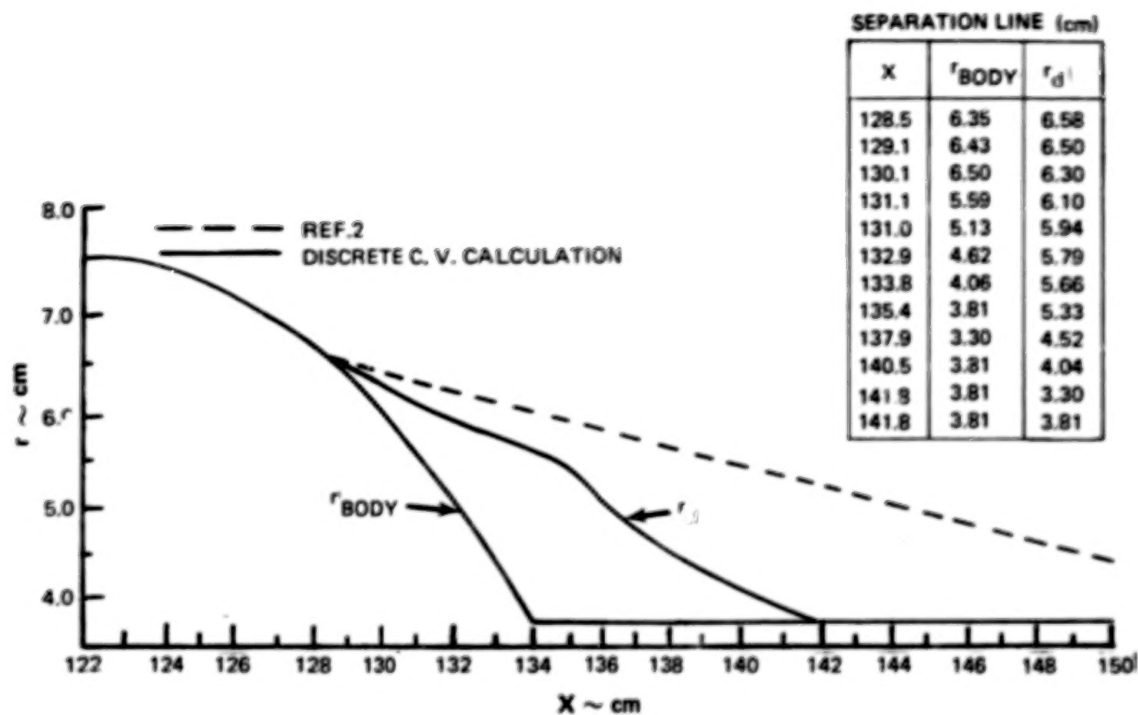


Figure 7 Comparison of Calculated Discriminating Streamline Shapes For Circular Arc Nozzle Configuration With $\beta = 17^\circ$ and $d_j/D = 0.51$ at $M_\infty = 0.8$

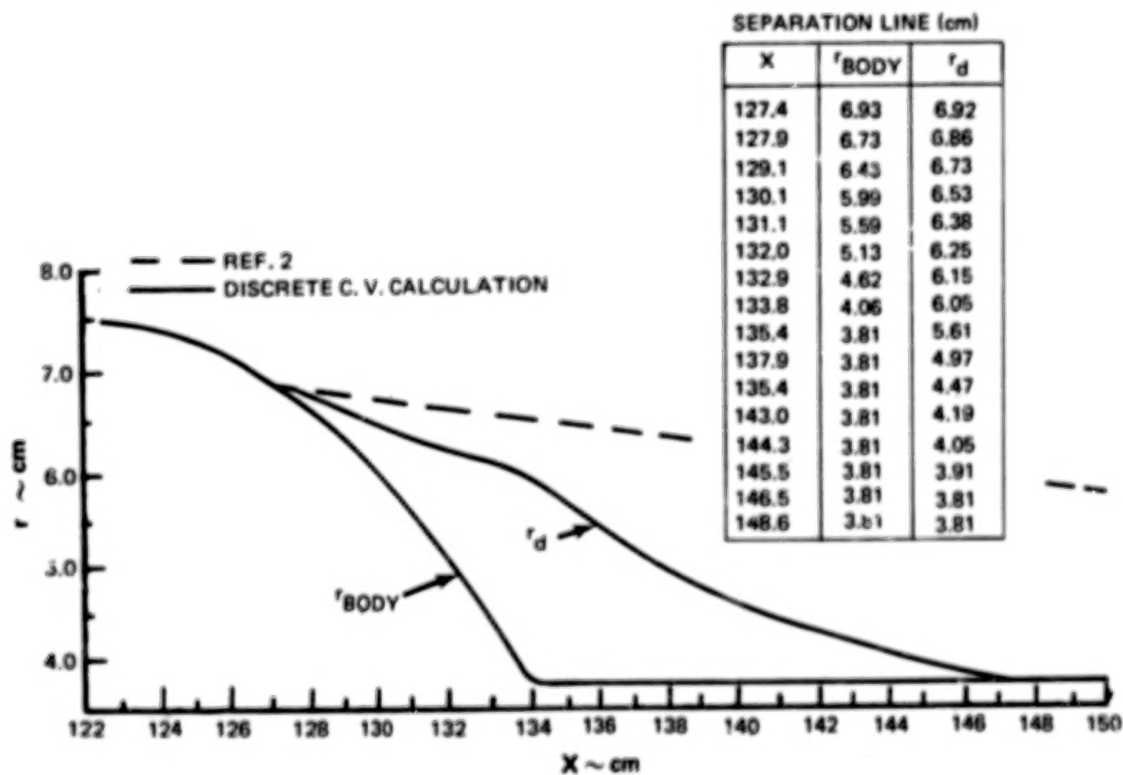


Figure 8 Comparison of Calculated Discriminating Streamline Shapes For Circular Arc Nozzle Configuration With $\beta = 17^\circ$ and $d_j/D = 0.51$ at $M_\infty = 0.90$

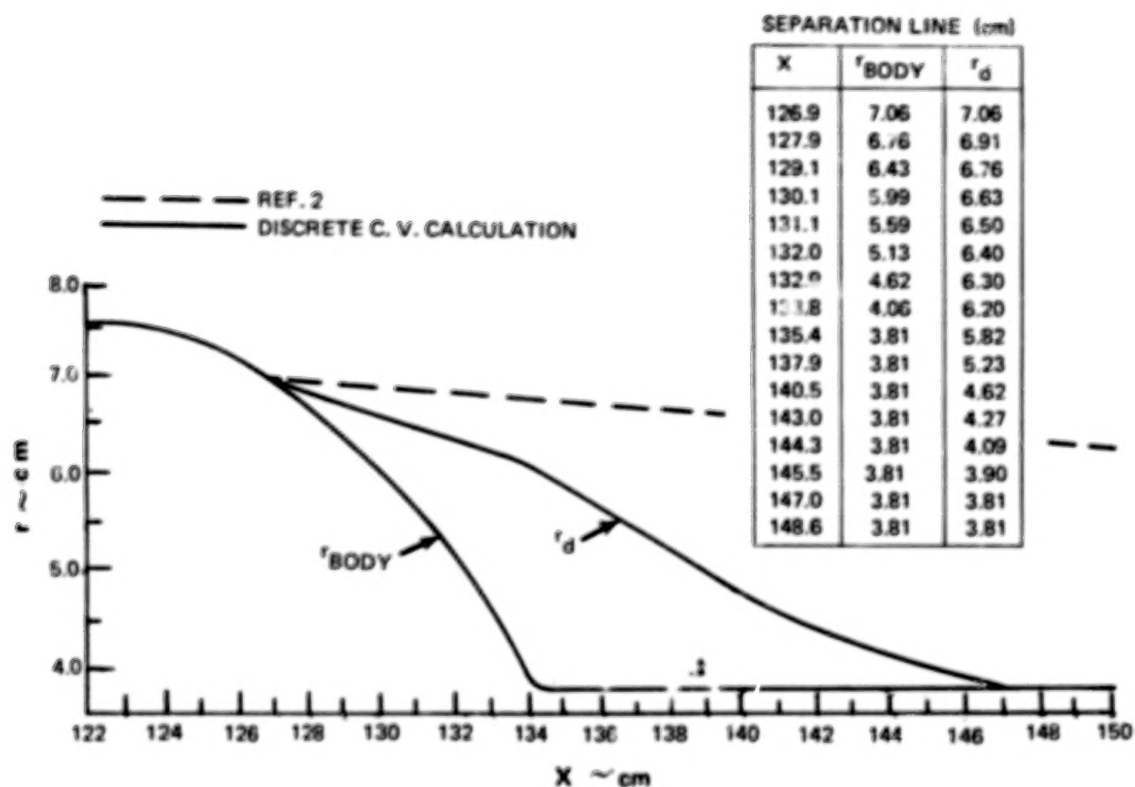


Figure 9 Comparison of Calculated Discriminating Streamline Shapes For Circular Arc Nozzle Configuration With $\beta = 17^\circ$ and $d_j/D = 0.51$ at $M_\infty = 0.94$

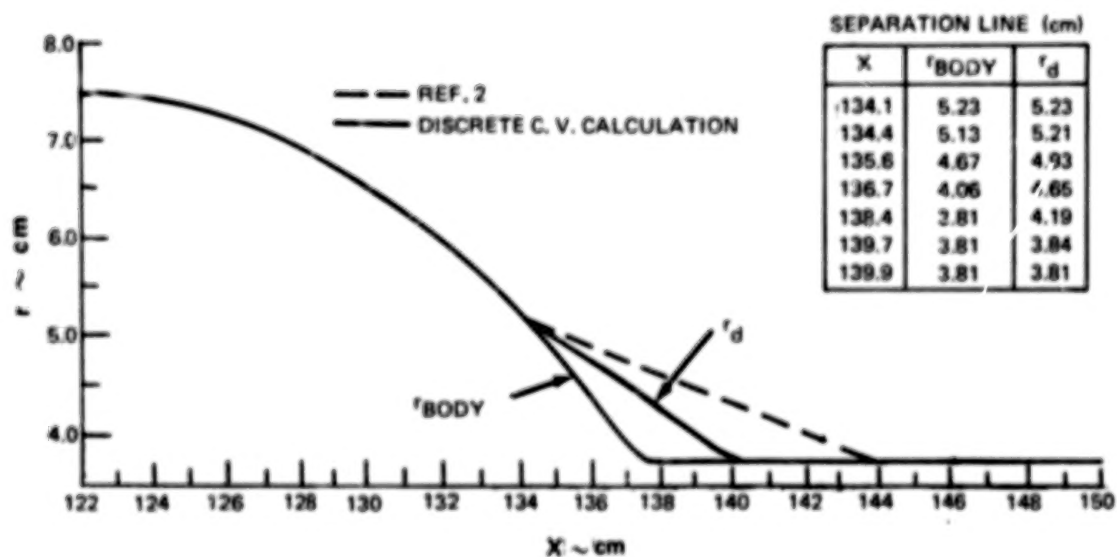


Figure 10 Comparison of Calculated Discriminating Streamline Shapes For Circular Arc Nozzle Configuration With $\beta = 138^\circ$ and $d_j/D = 0.51$ at $M_\infty = 0.8$

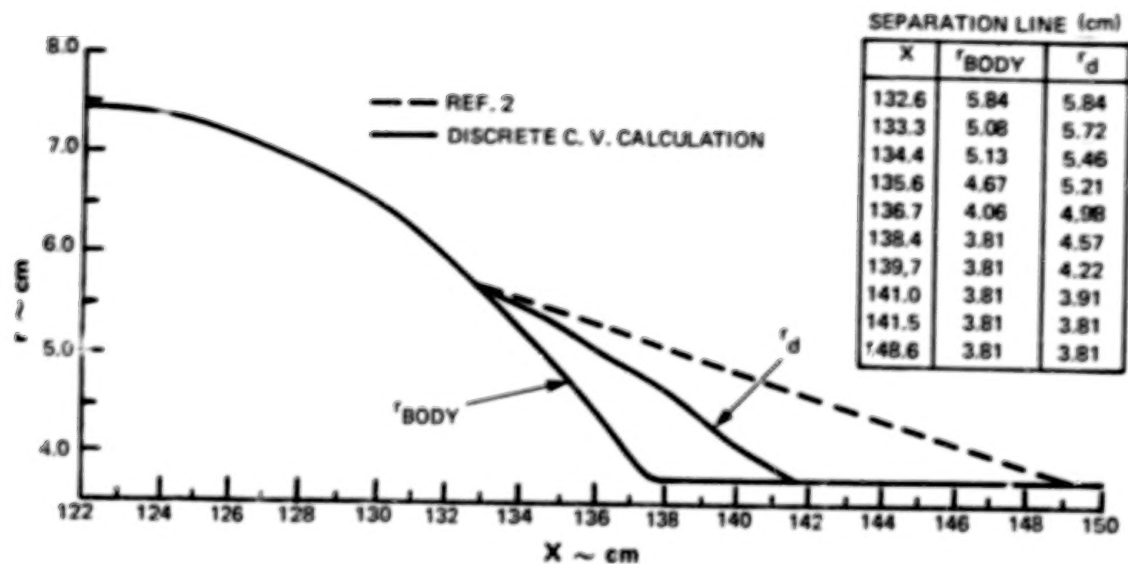


Figure 11 Comparison of Calculated Discriminating Streamline Shapes For Circular Arc Nozzle Configuration With $\beta = 13.8^\circ$ and $d_j/D = 0.51$ at $M_\infty = 0.90$

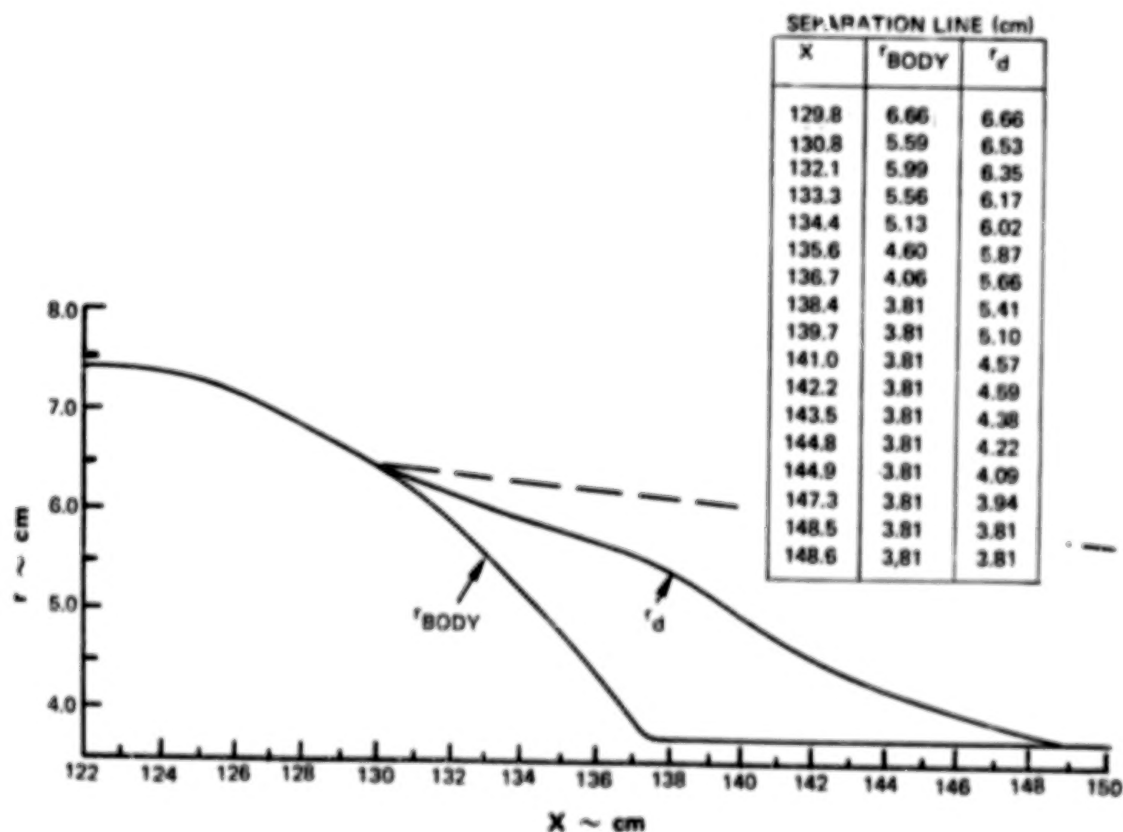


Figure 12 Comparison of Calculated Discriminating Streamline Shapes For Circular Arc Nozzle Configuration With $\beta = 13.8^\circ$ and $d_j/D = 0.51$ at $M_\infty = 0.94$

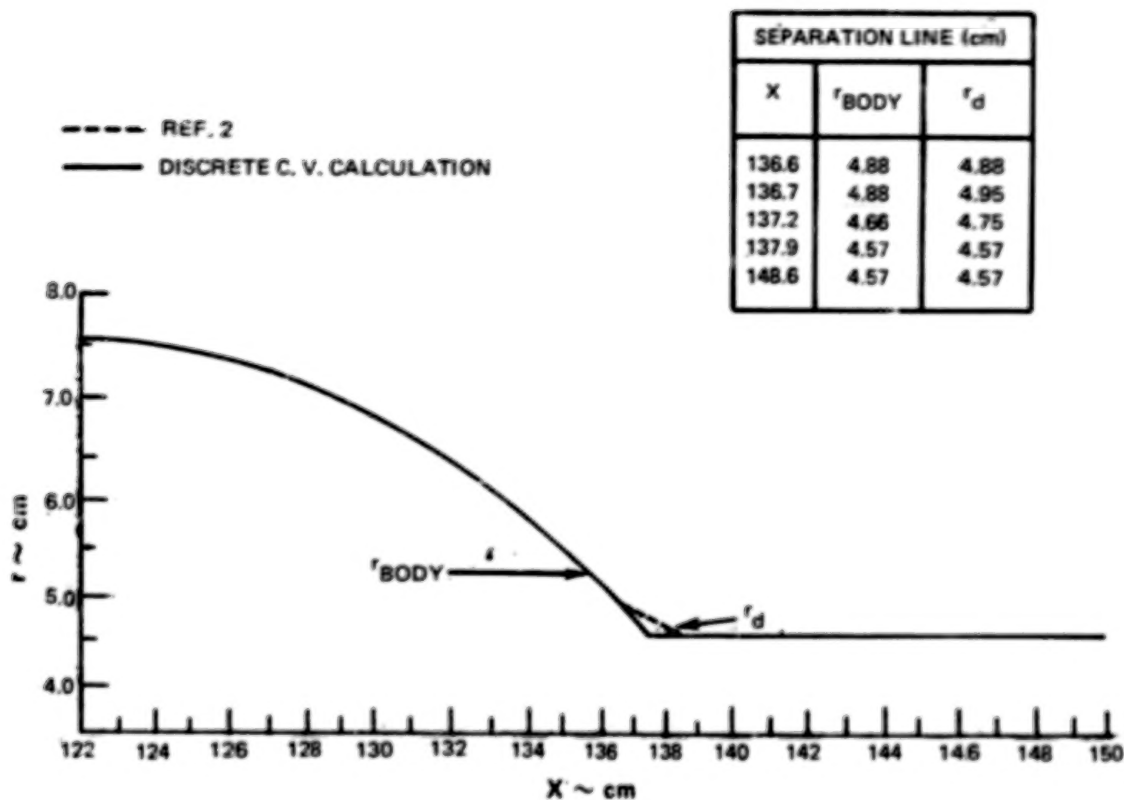


Figure 13 Comparison of Calculated Discriminating Streamline Shapes For Circular Arc Nozzle Configuration With $\beta = 11^\circ$ and $d_b/D = 0.61$ at $M_\infty = 0.8$

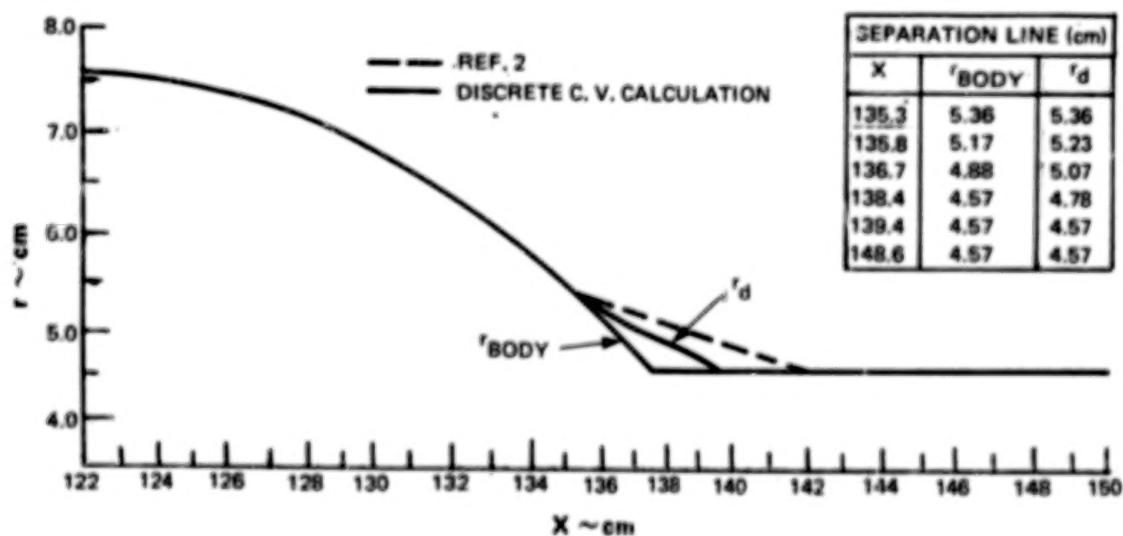


Figure 14 Comparison of Calculated Discriminating Streamline Shapes For Circular Arc Nozzle Configuration With $\beta = 11^\circ$ and $d_b/D = 0.61$ at $M_\infty = 0.90$

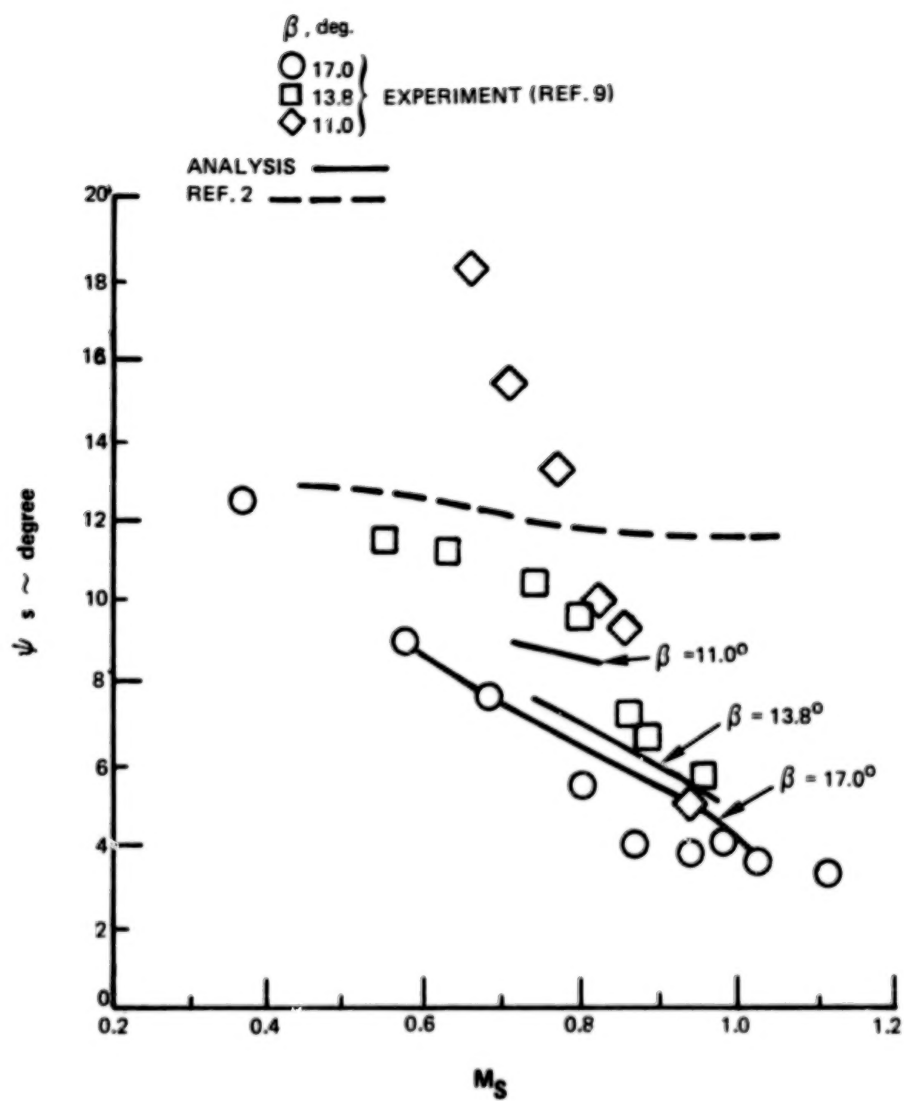


Figure 15 Comparison of Measured and Predicted Separation Angles

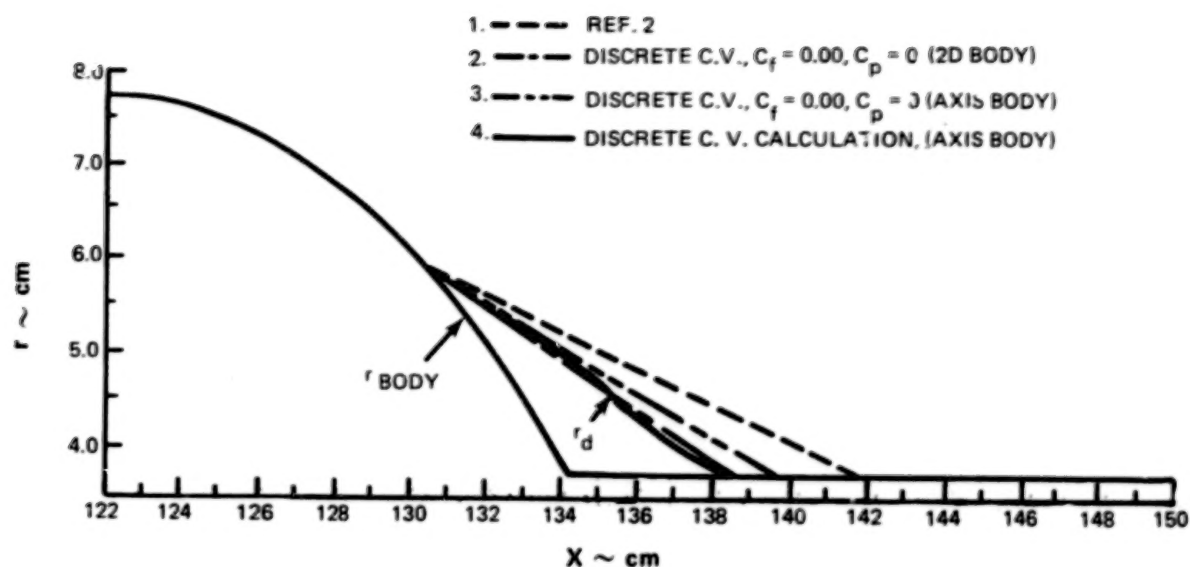


Figure 16 Skin Friction and Pressure Gradient Effects on the Calculated Discriminating Streamline For Circular Arc Nozzle Configuration With $\beta = 17^\circ$ and $d_b/D = 0.51$ at $M_\infty = 0.6$

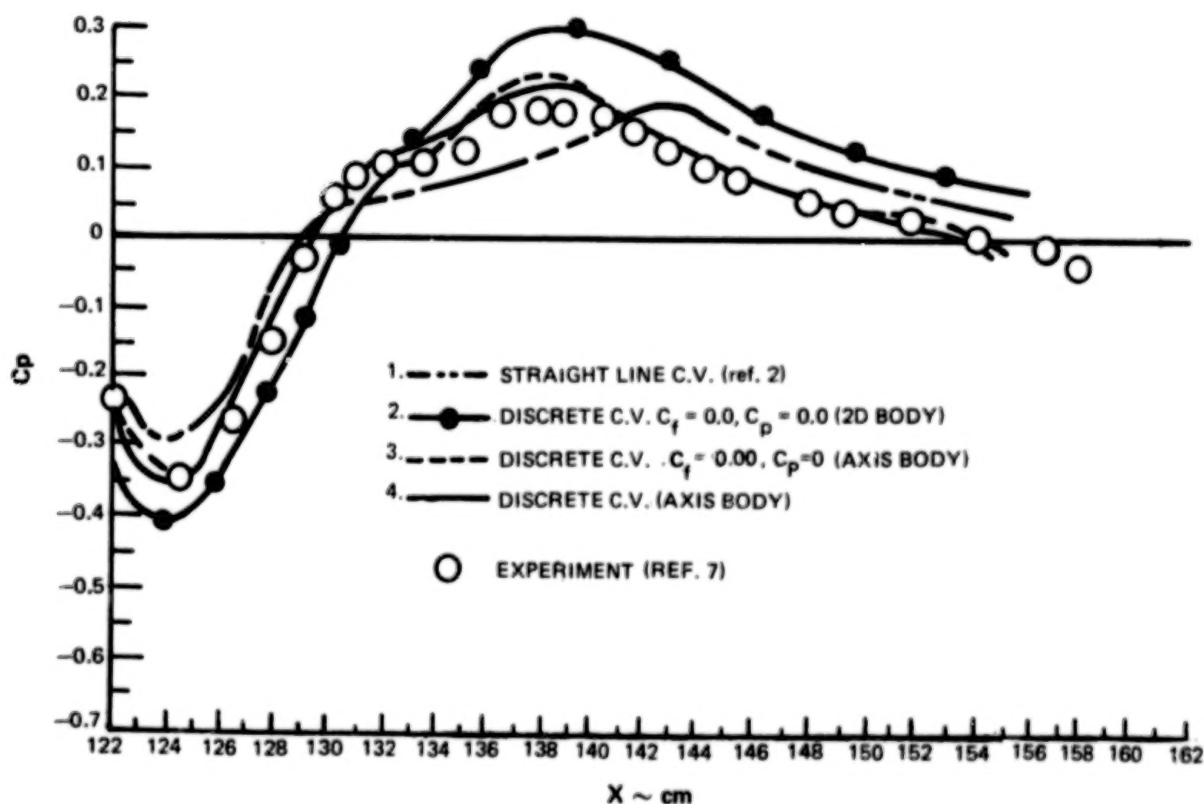


Figure 17 Discriminating Streamline Shape Effects on Afterbody Pressures For Circular Arc Nozzle Configuration With $\beta = 17^\circ$ and $d_b/D = 0.51$ at $M_\infty = 0.6$

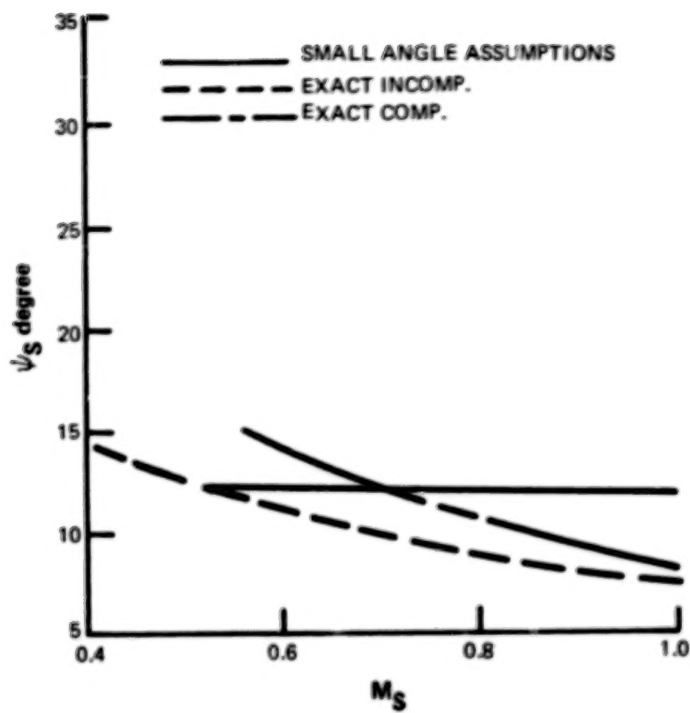


Figure 18 Comparison of Predicted Separation Angles

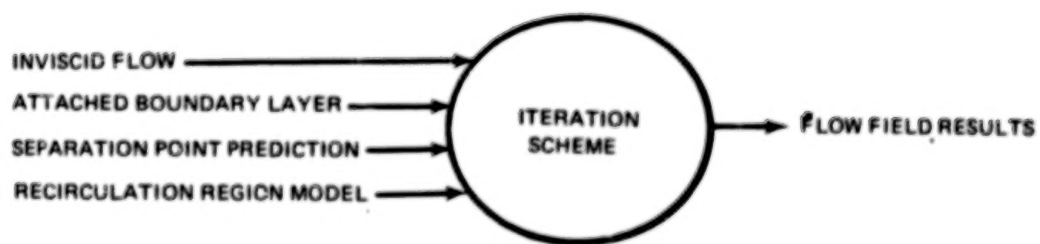


Figure 19 Major Components of the Calculation Scheme

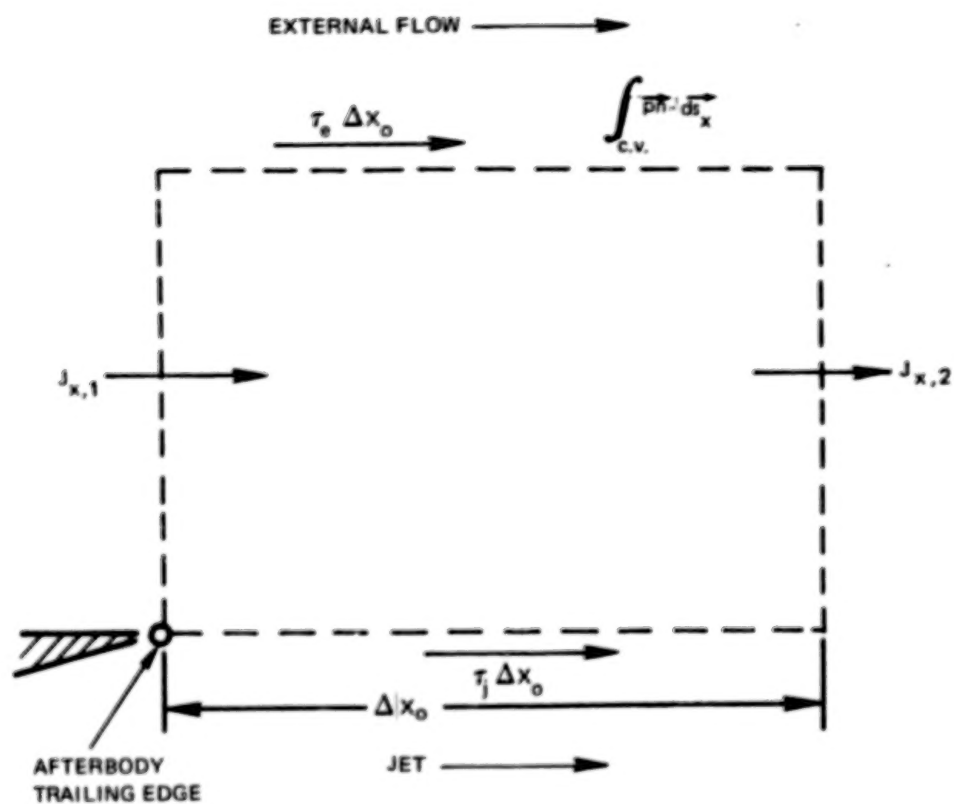


Figure 20 Discrete Control Volume For Jet Entrainment Region

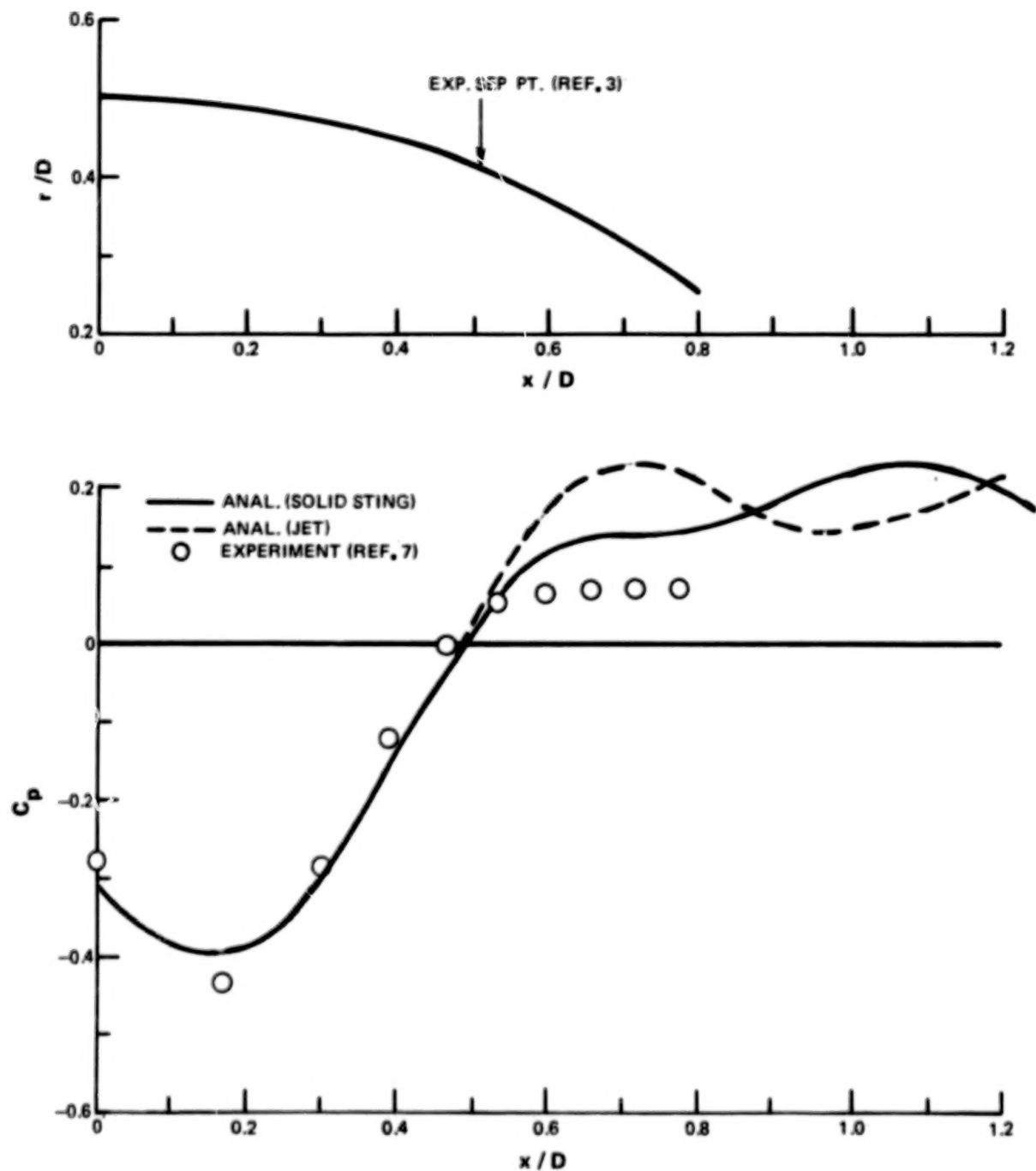


Figure 21 Jet Shearing Effects on Predicted Afterbody Pressure For Circular Arc Nozzle Configuration With $\bar{q}/D = 0.8$ and $d_b/D = 0.51$ at $M_\infty = 0.8$ and $NPR \approx 2.00$

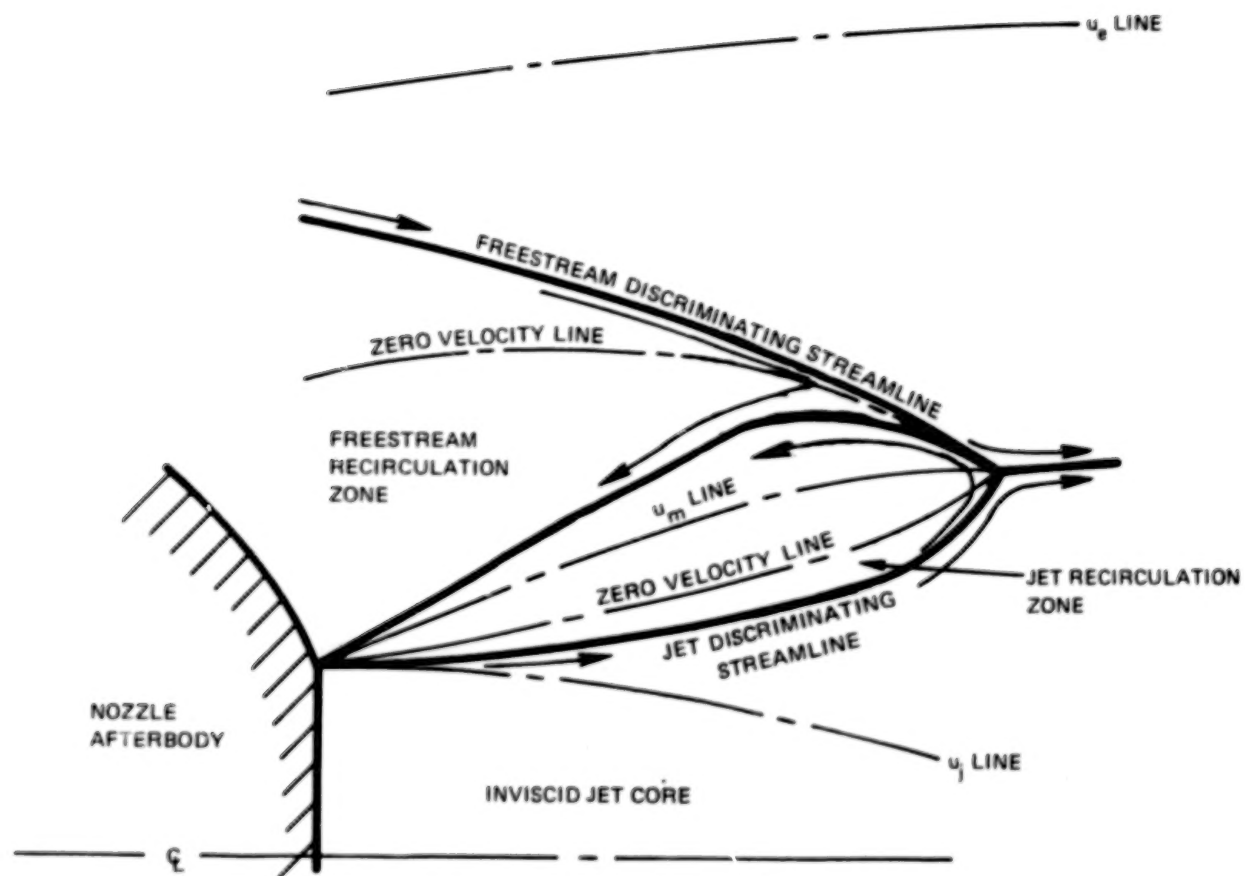


Figure 22 Schematic of the Flow Recirculation Regions

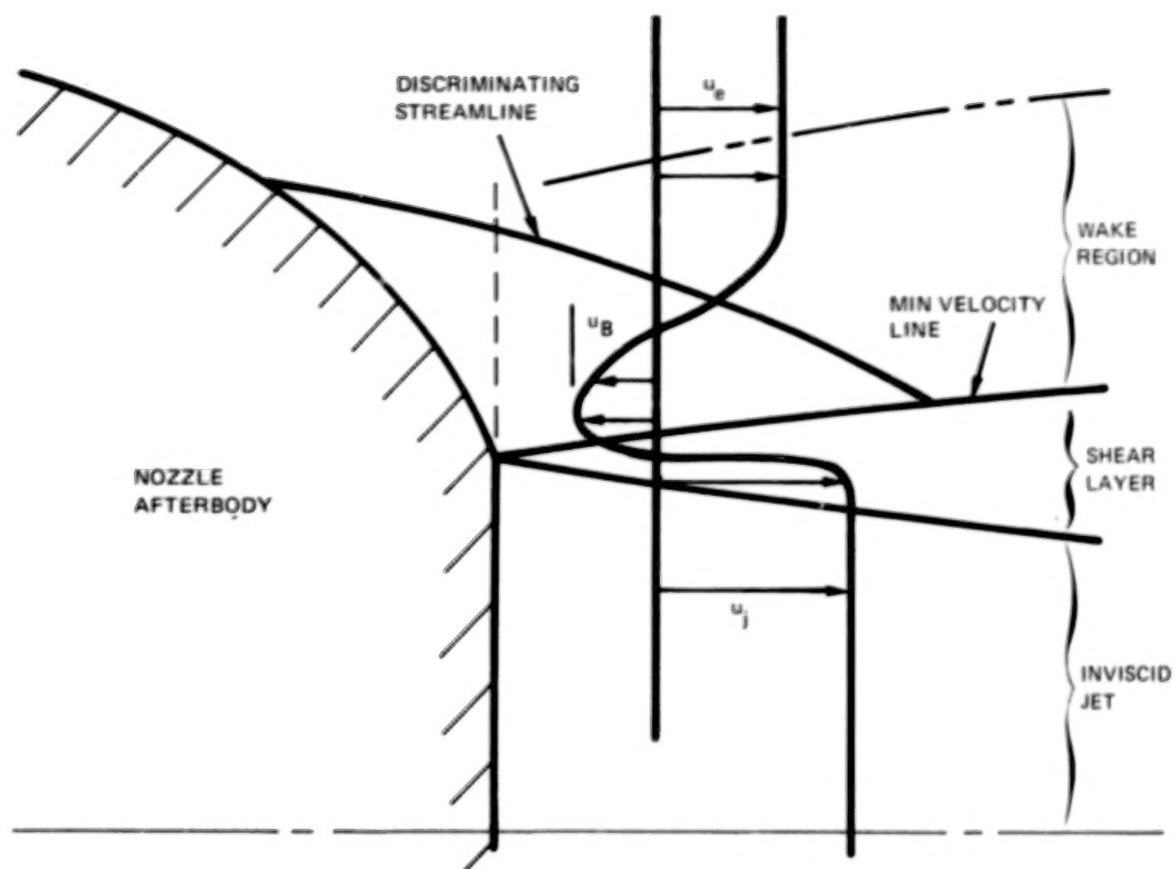


Figure 23 Schematic of the Jet Recirculation Flowfield

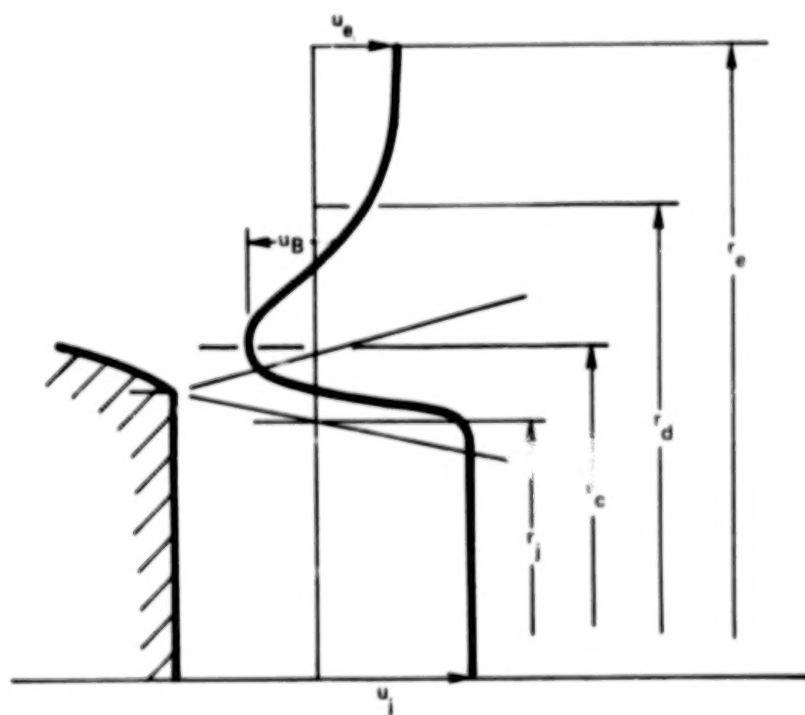


Figure 24 Schematic of the Assumed Velocity Profiles

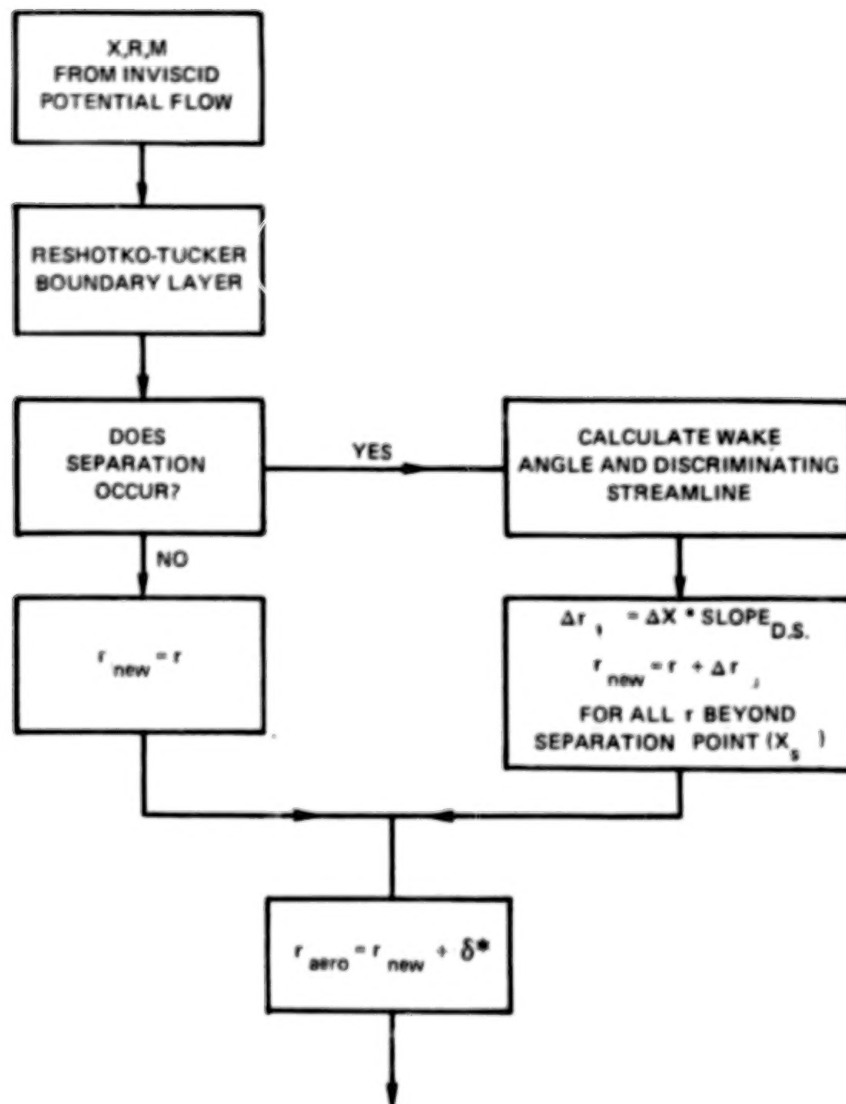


Figure 25 A Schematic of the Viscous Flow Calculation

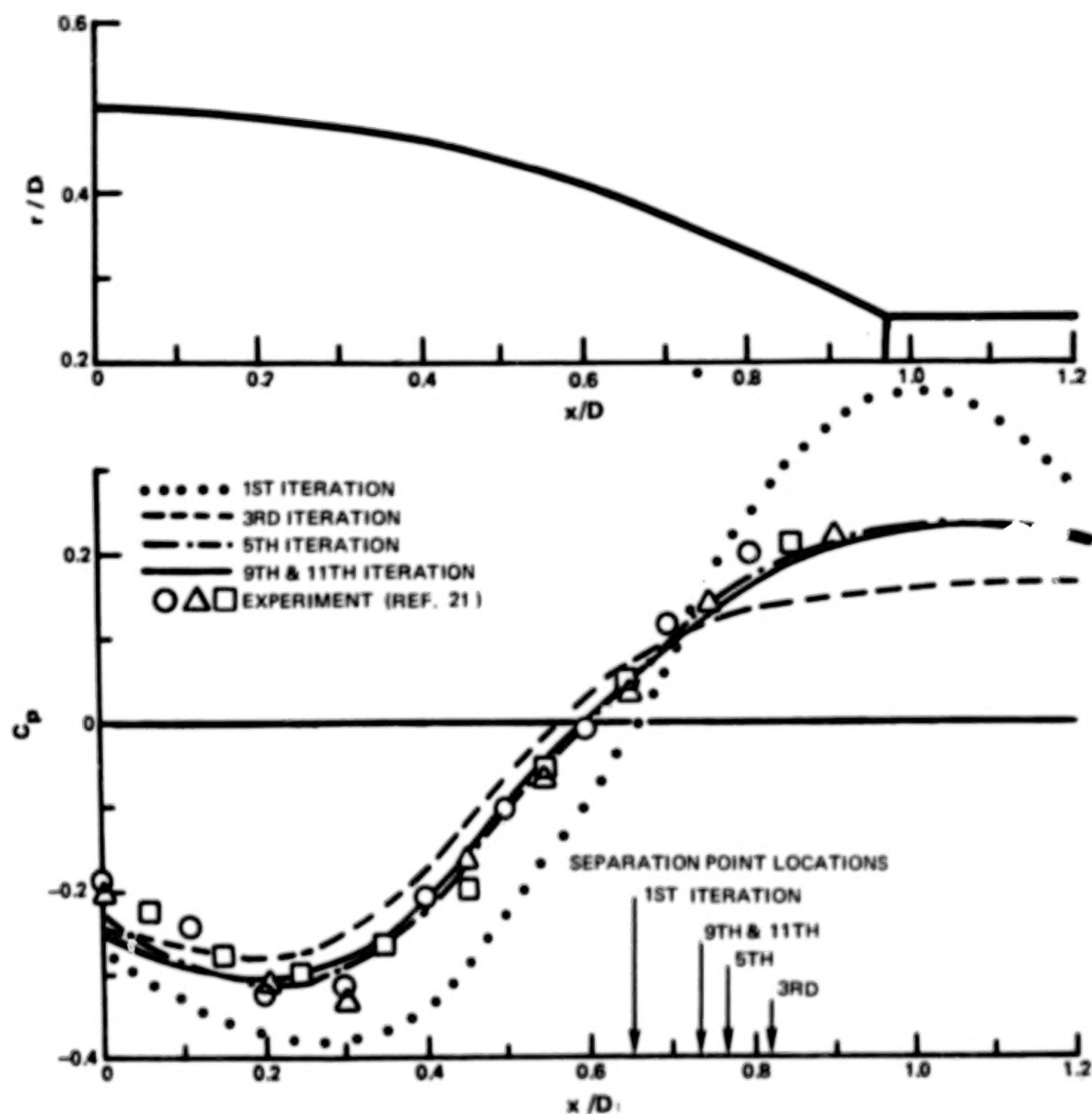


Figure 26 Convergence of the Viscous Inviscid Flow Iteration Scheme For A Circular Arc Conical Afterbody Configuration (6524) With An $\psi/D = 0.961$ and $d_b/D = 0.50$ at $M_\infty = 0.601$ and a Reynolds Number of 4.29×10^7

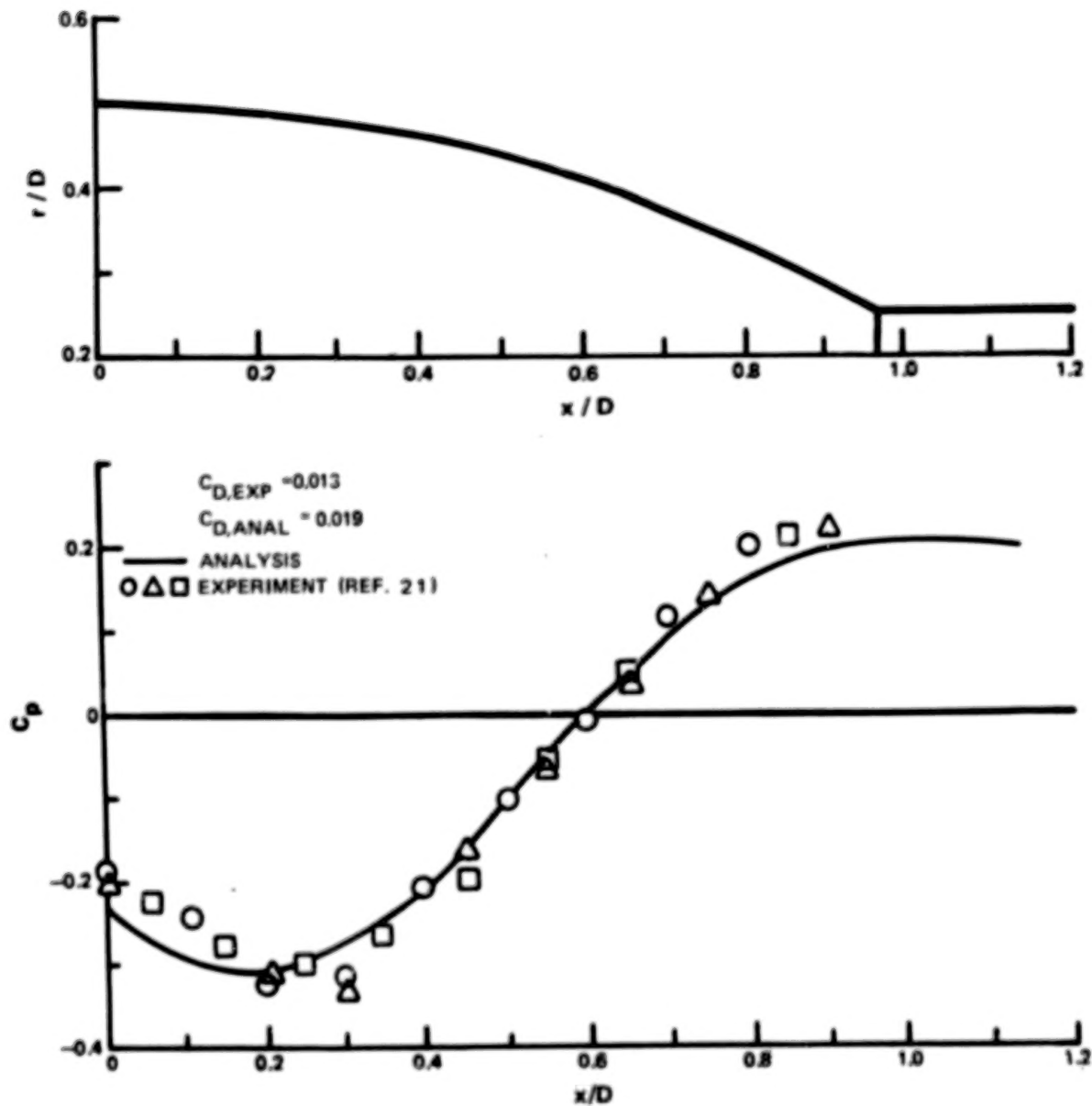


Figure 27 Comparison of Measured and Predicted Afterbody Pressures For A Circular Arc Conical Afterbody Configuration (6524) With $l/D = 0.961$ and $d_f/D = 0.50$ at $M_\infty = 0.601$ and a Reynolds Number of 4.29×10^7

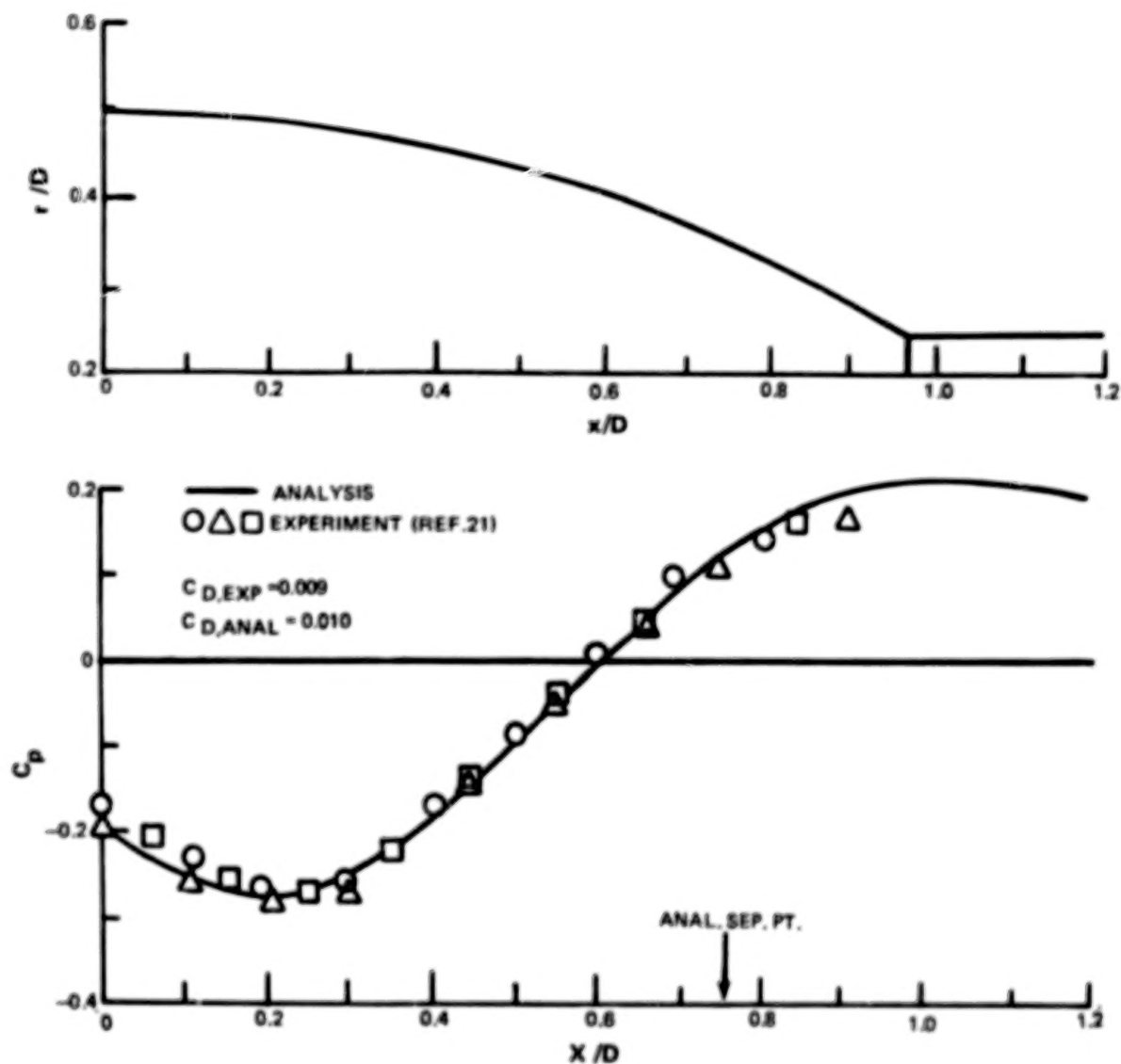


Figure 28 Comparison of Measured and Predicted Afterbody Pressures For A Circular Arc Conical Afterbody Configuration With $\theta/D = 0.961$ and $d_b/D = 0.50$ at $M_\infty = 0.597$ and a Reynolds Number of 2.61×10^6

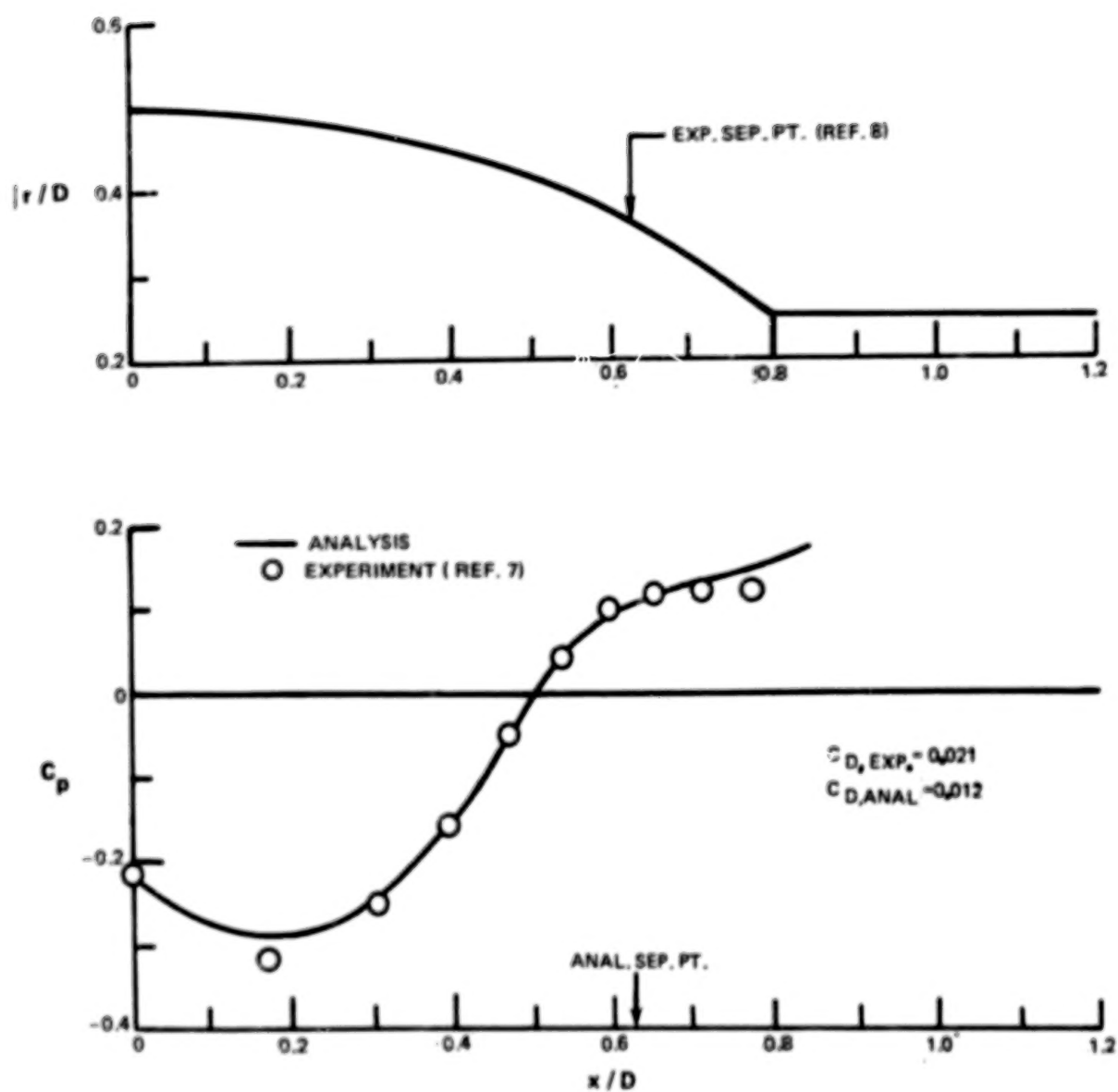


Figure 29 Comparison of Measured and Predicted Afterbody Pressures For A Circular Arc Nozzle Configuration With $\beta = 17^\circ$ and $d_y/D = 0.51$ at $M_\infty = 0.397$

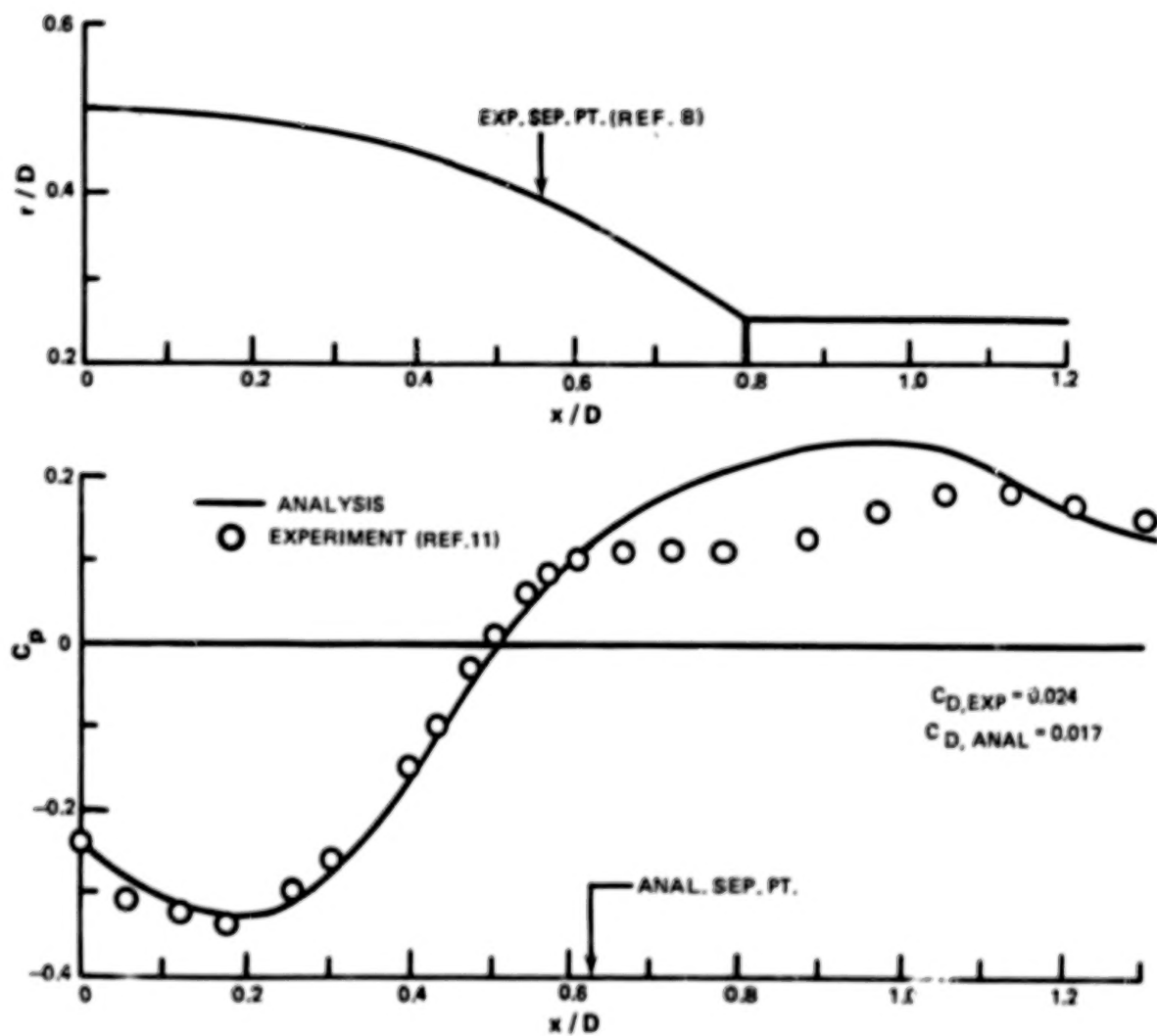


Figure 30 Comparison of Measured and Predicted Afterbody Pressures For A Circular Arc Nozzle Configuration With $\beta = 17^\circ$ and $d_f/D = 0.51$ at $M_\infty = 0.6$

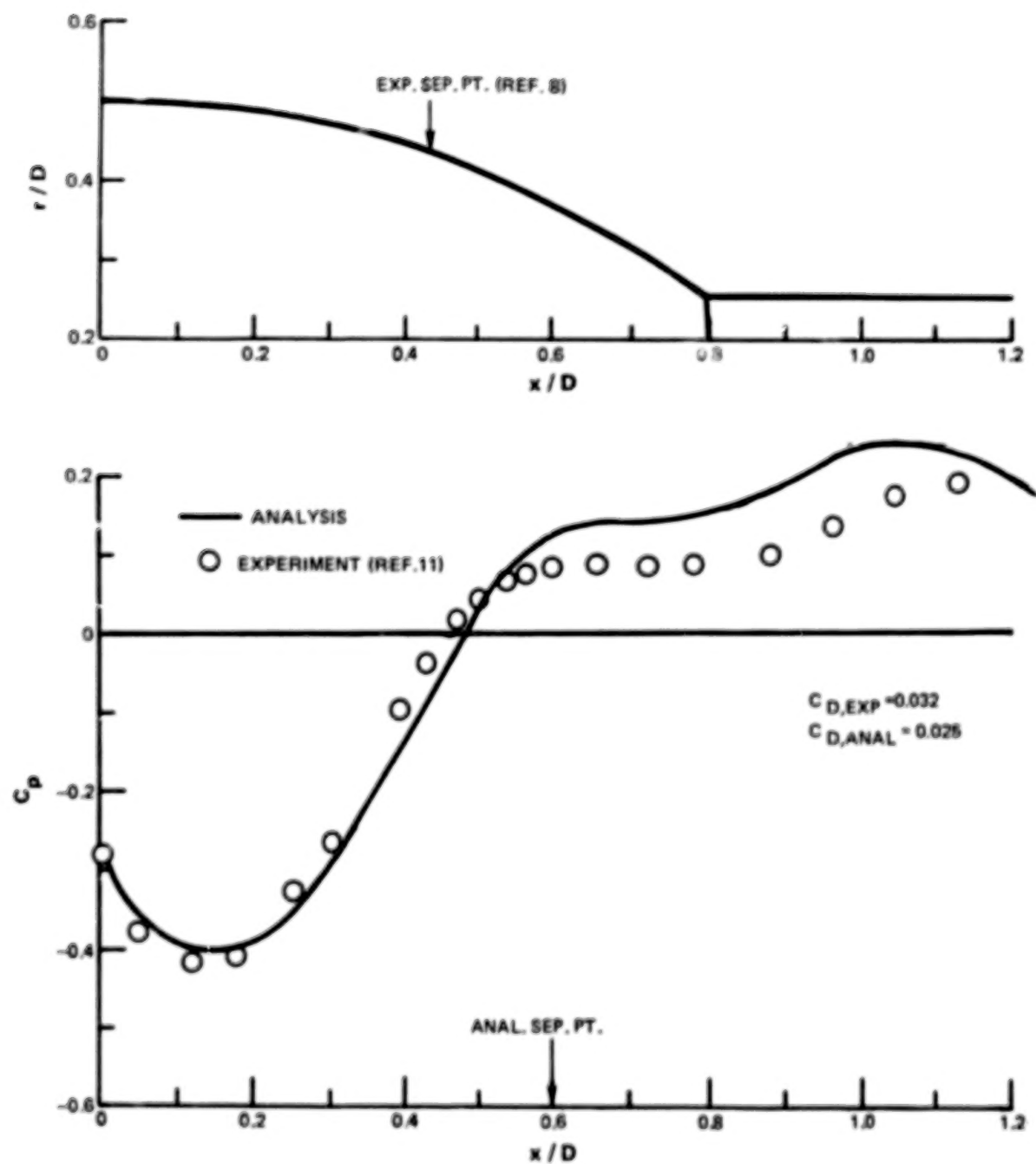


Figure 31 Comparison of Measured and Predicted Afterbody Pressures For A Circular Arc Nozzle Configuration With $\beta = 17^\circ$ and $d_f/D = 0.51$ at $M_\infty = 0.8$

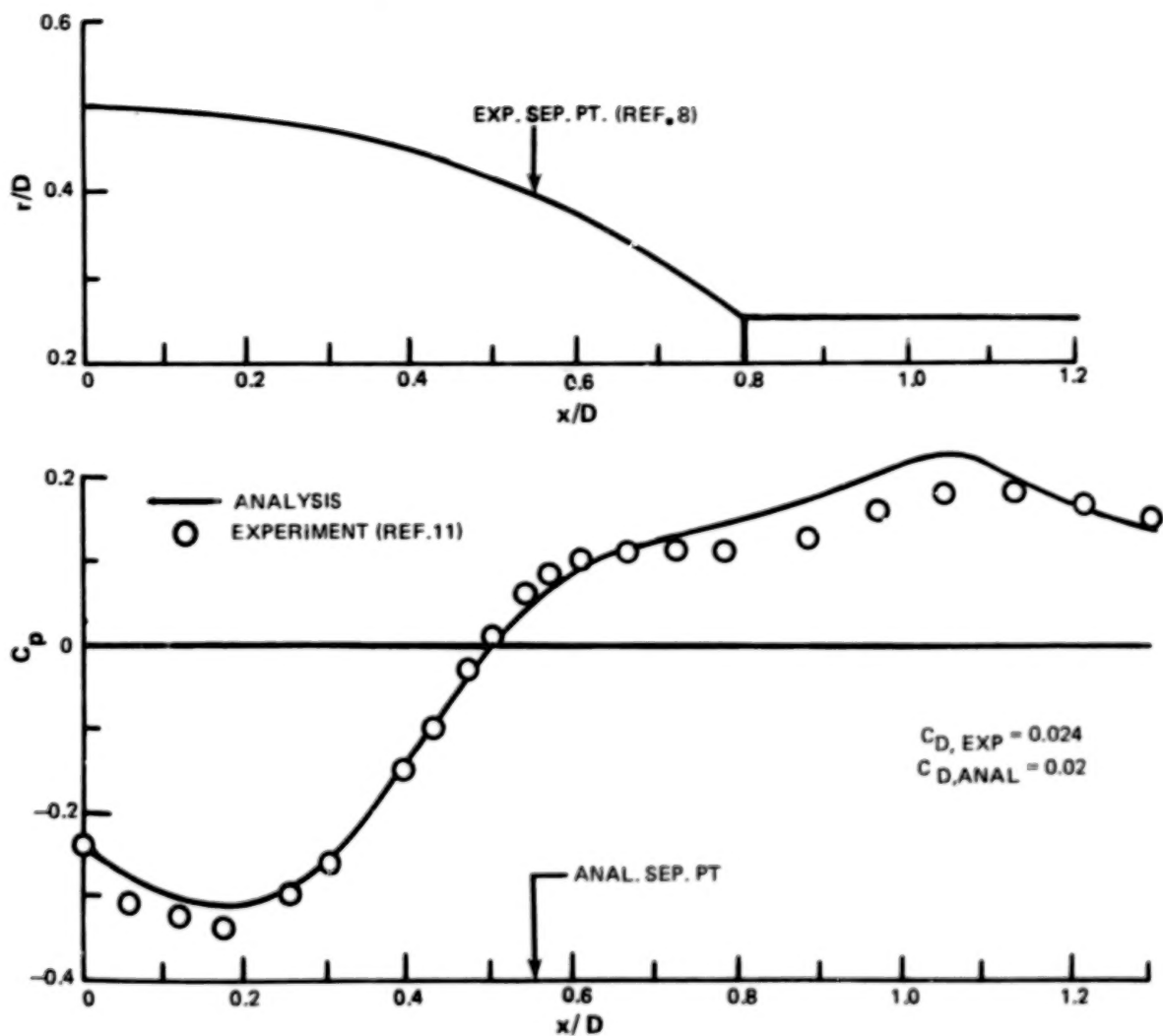


Figure 32 Comparison of Measured and Predicted Afterbody Pressures With Separation Point Fixed at Experimental Location For A Circular Arc Nozzle Configuration With $\beta = 17^\circ$ and $d_b/D = 0.51$ at $M_\infty = 0.6$

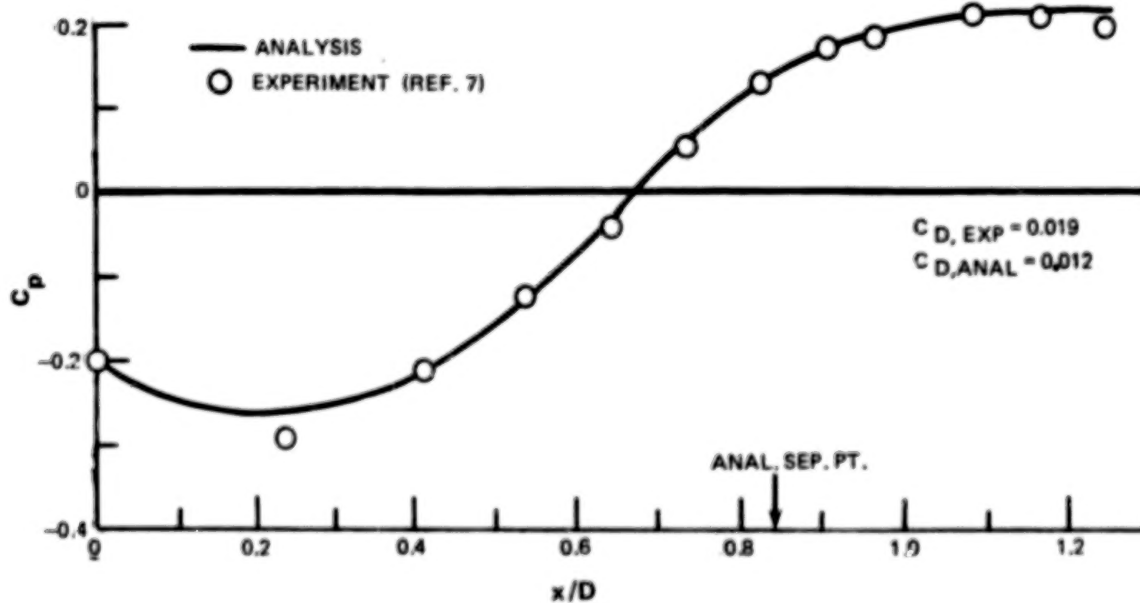
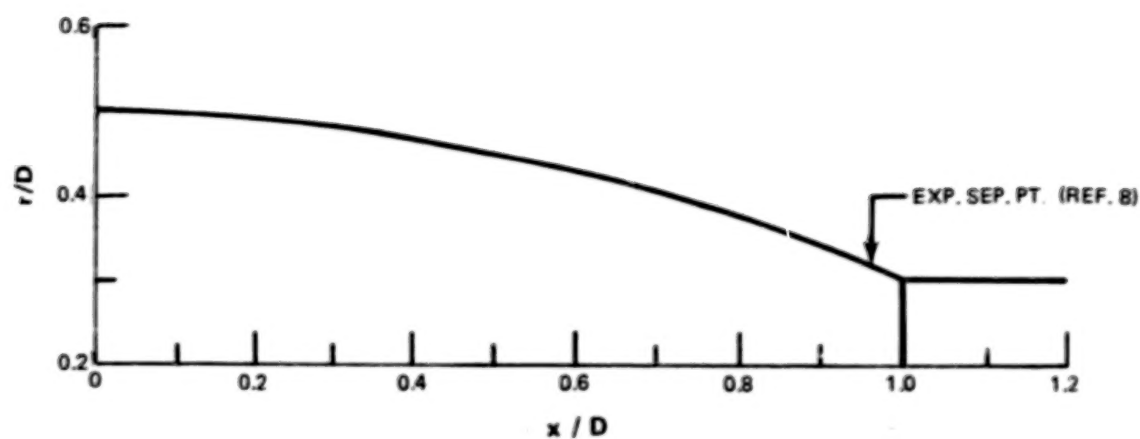


Figure 33 Comparison of Measured and Predicted Afterbody Pressures For A Circular Arc Nozzle Configuration With $\beta = 11^\circ$ and $d_j/D = 0.61$ at $M_\infty = 0.798$

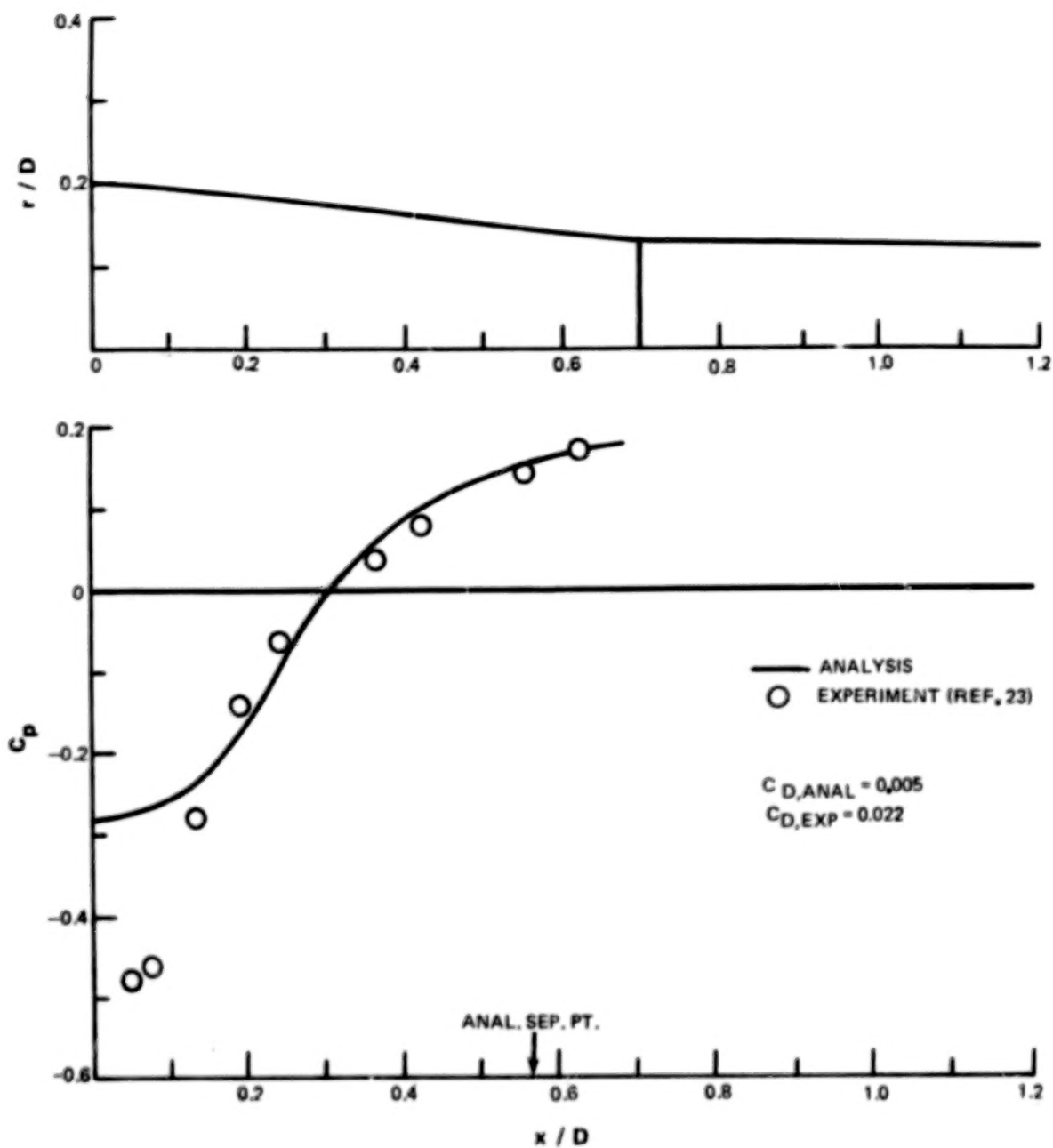


Figure 34 Comparison of Measured and Predicted Pressures for Shrewsbury Configuration 1015 at $M_{\infty} = 0.7$

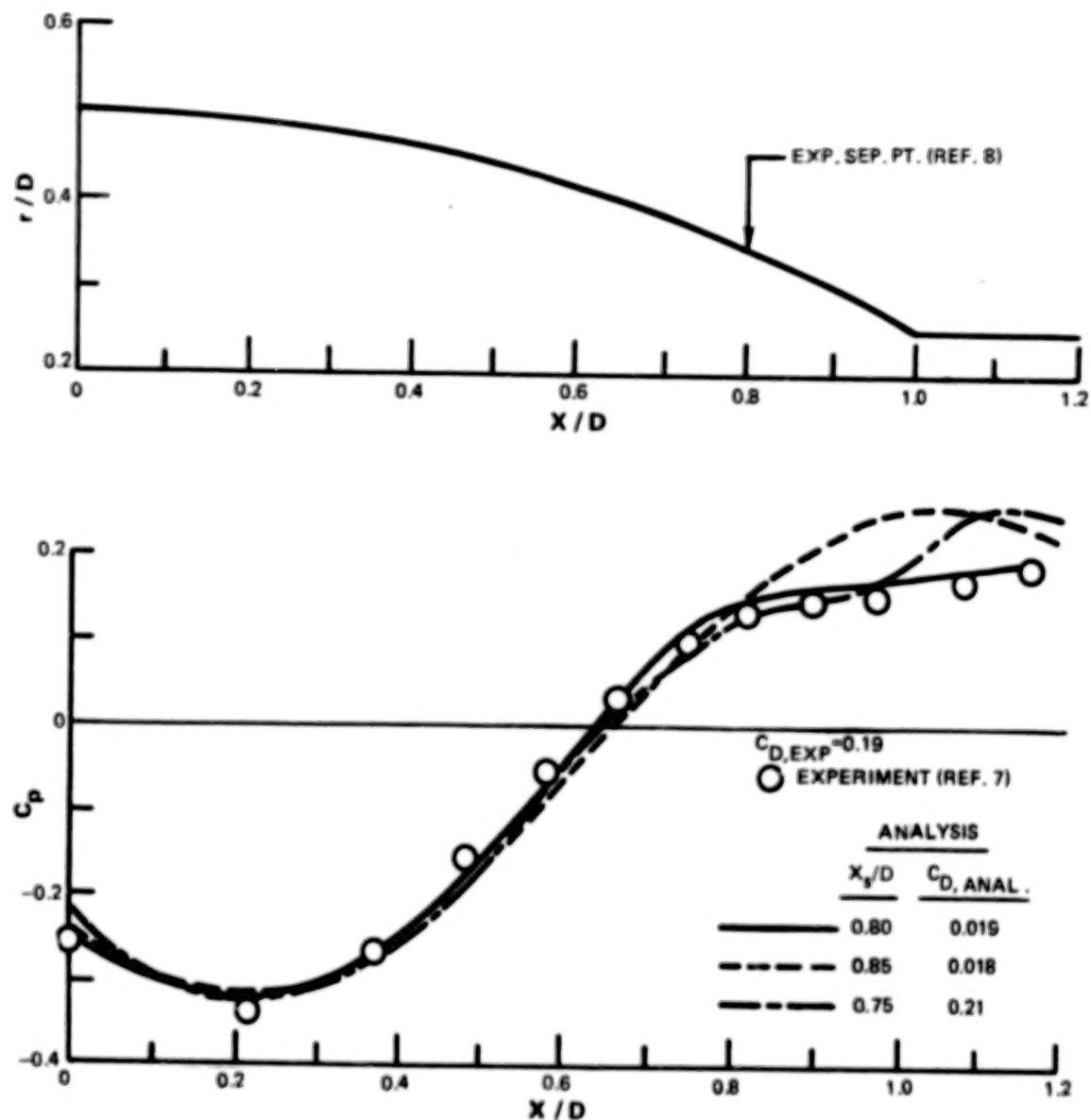


Figure 35 Effect of Separation Location on Predicted Pressures and Drag of Circular Arc Nozzle Configuration With $\beta = 13.4^\circ$ and $d_b/D = 0.51$ at $M_\infty = 0.798$

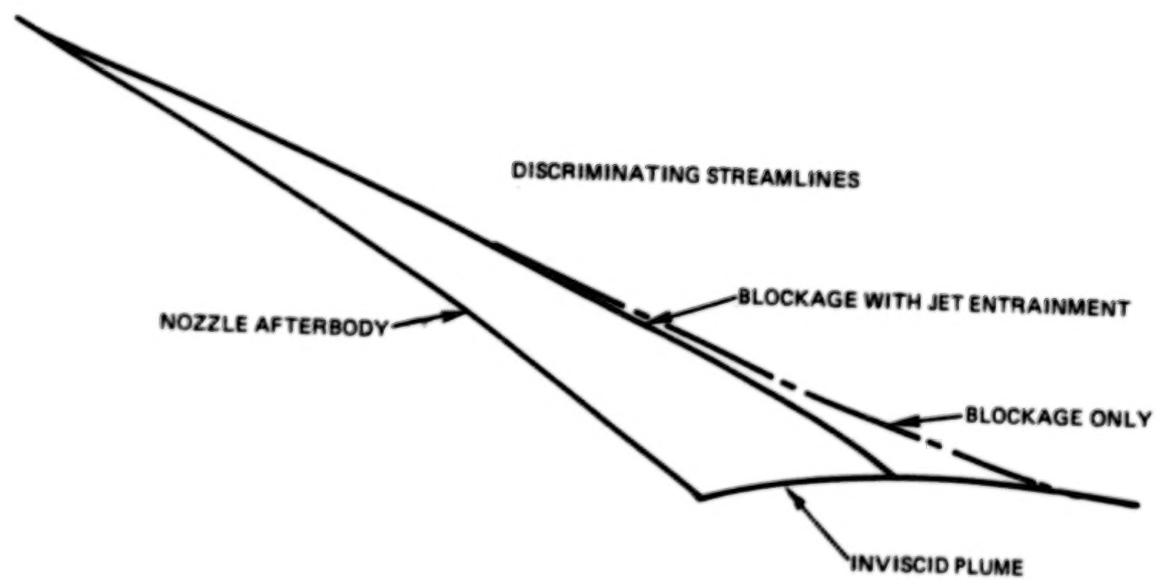


Figure 36 Effect of Jet Entrainment on Discriminating Streamline Shape of a Circular Arc Afterbody at $M_{\infty} = 0.6$ and $NPR = 2.91$

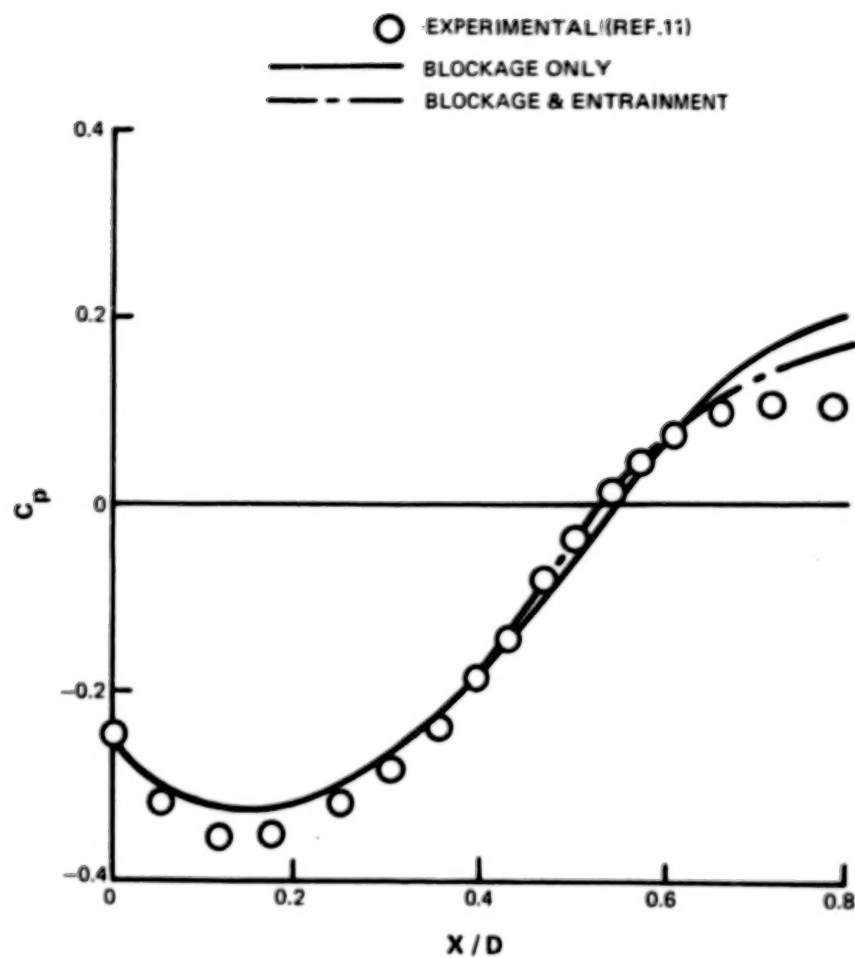


Figure 37 Effect of Entrainment on Afterbody Calculated Pressures for a Circular Arc Nozzle Configuration With $\beta = 17^\circ$ and $d_j/D = 0.51$ at $M_\infty = 0.8$ and $NPR = 2.91$

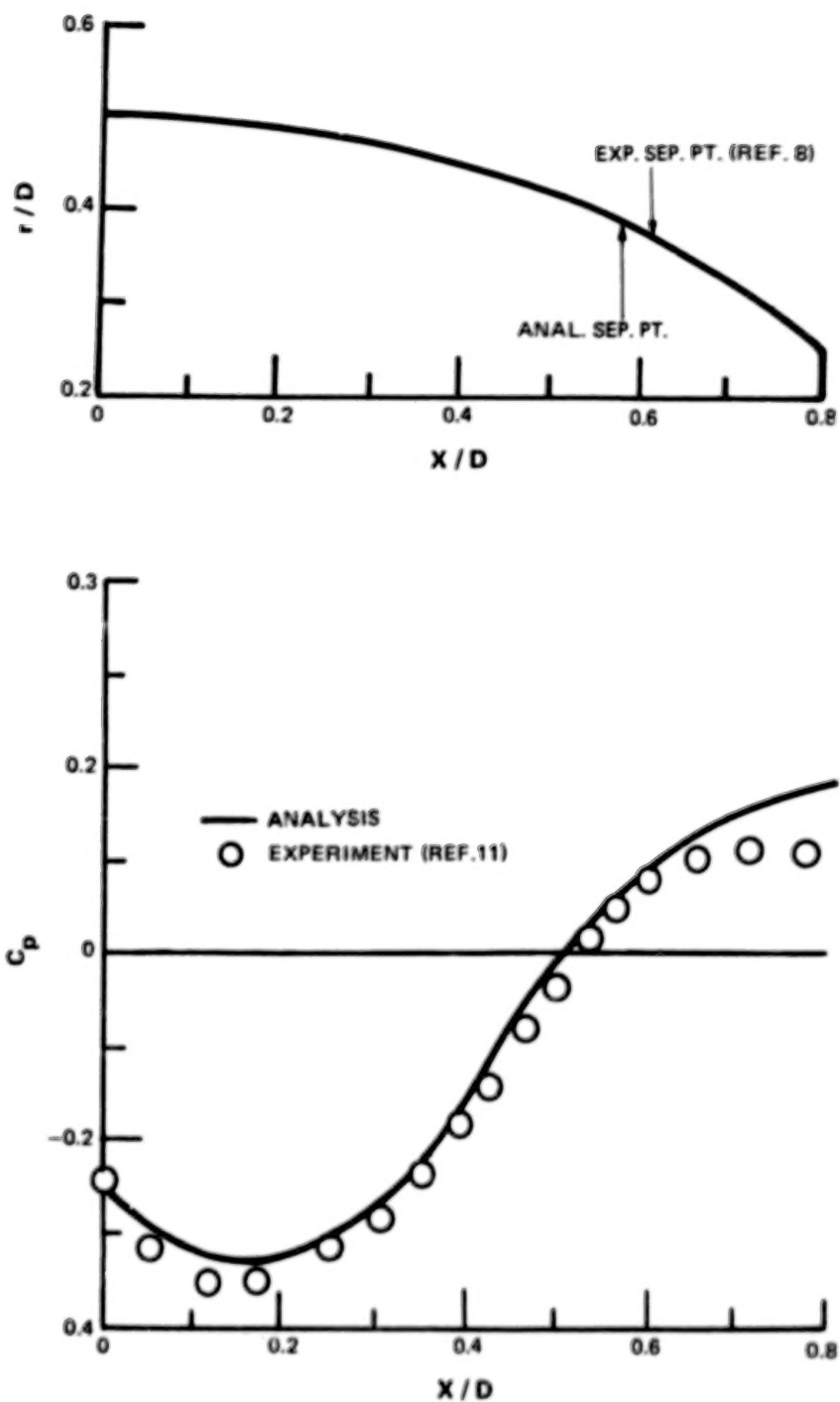


Figure 38 Comparison of Measured and Predicted Afterbody Pressures for a Circular Arc Afterbody With $\beta = 17^\circ$ and $d_f/D = 0.51$ at $M_\infty = 0.6$ and $NPR = 2.91$

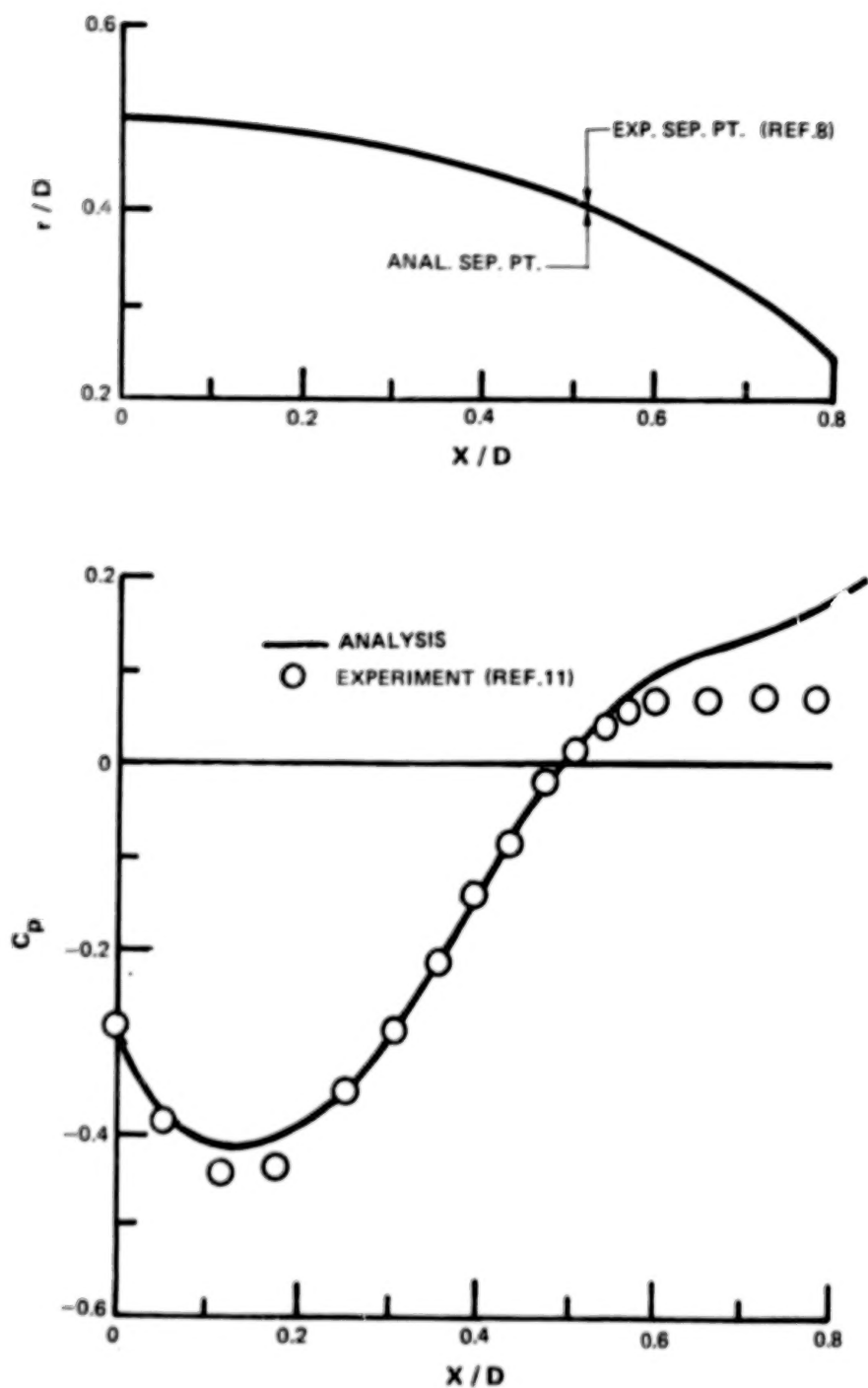


Figure 39 Comparison of Measured and Predicted Afterbody Pressures for a Circular Arc Afterbody With $\beta = 17^\circ$ $d_f/D = 0.51$ at $M_\infty = 0.8$ and $NPR = 2.91$

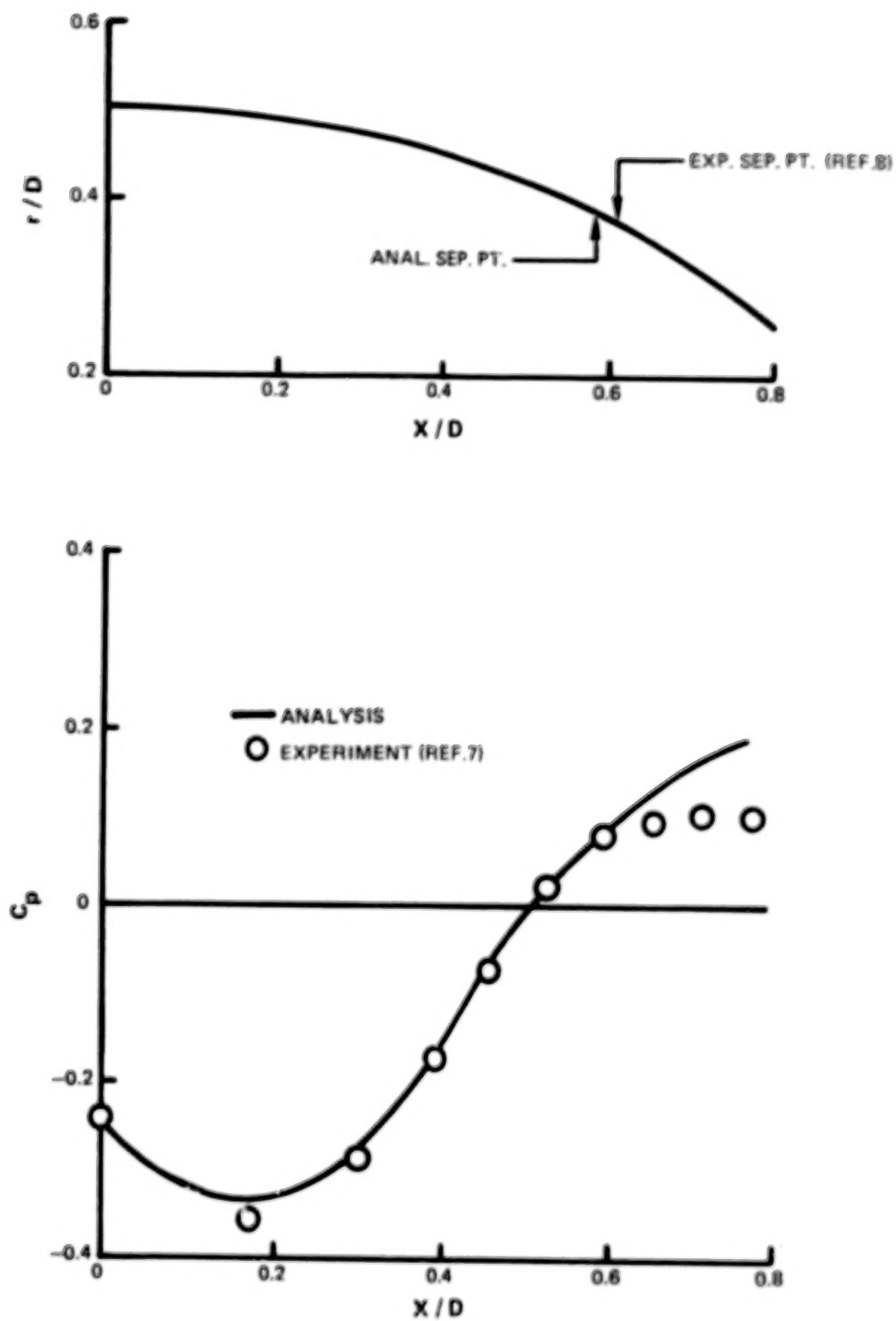


Figure 40 Comparison of Measured and Predicted Afterbody Pressures for a Circular Arc Afterbody With $\beta = 17^\circ$ and $d_f/D = 0.51$ at $M_\infty = 0.598$ and $NPR = 2.002$

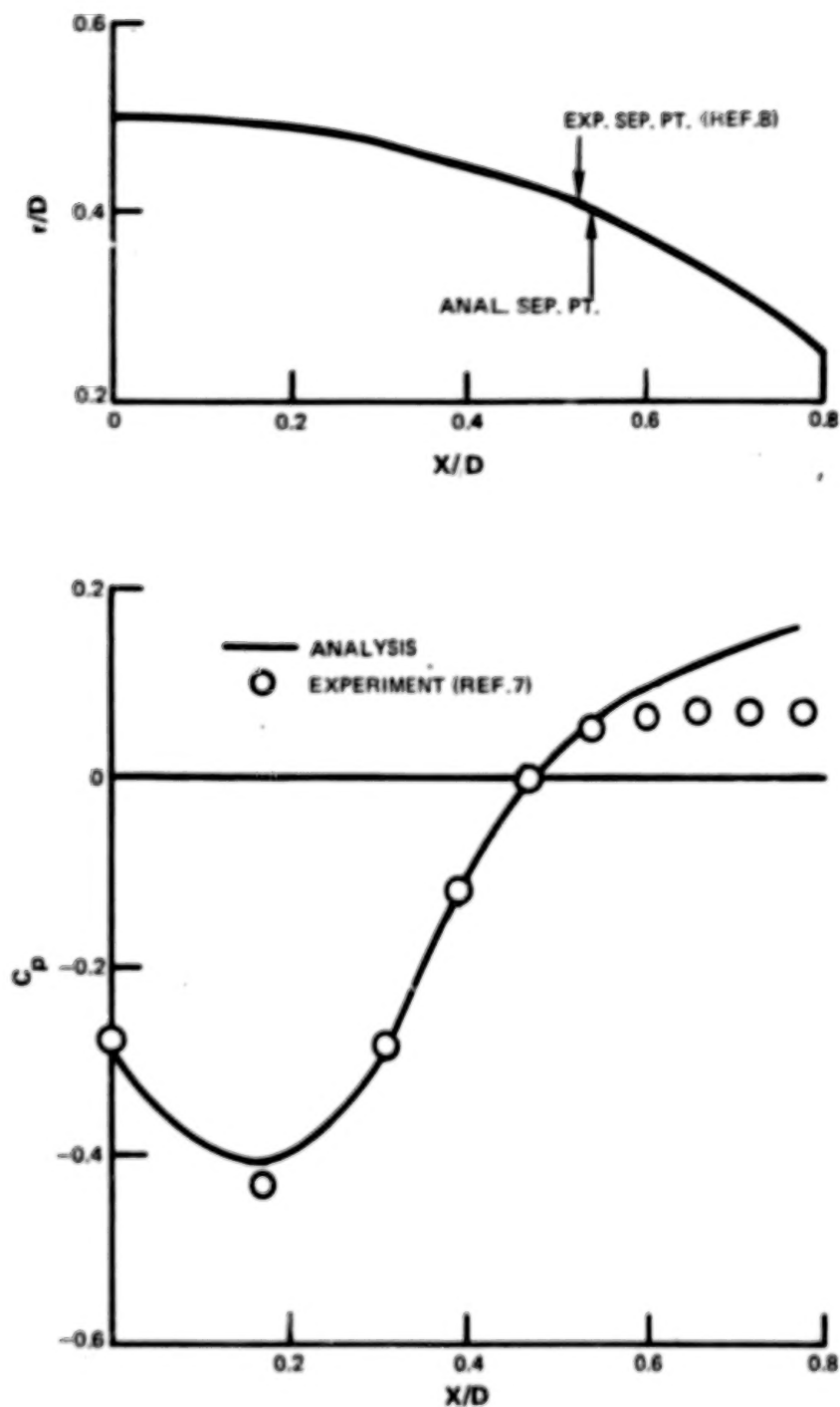


Figure 41 Comparison of Measured and Predicted Afterbody Pressures for a Circular Arc Afterbody With $\beta = 17^\circ$ and $d_p/D = 0.51$ at $M_\infty = 0.8$ and $NPR \approx 2.0$

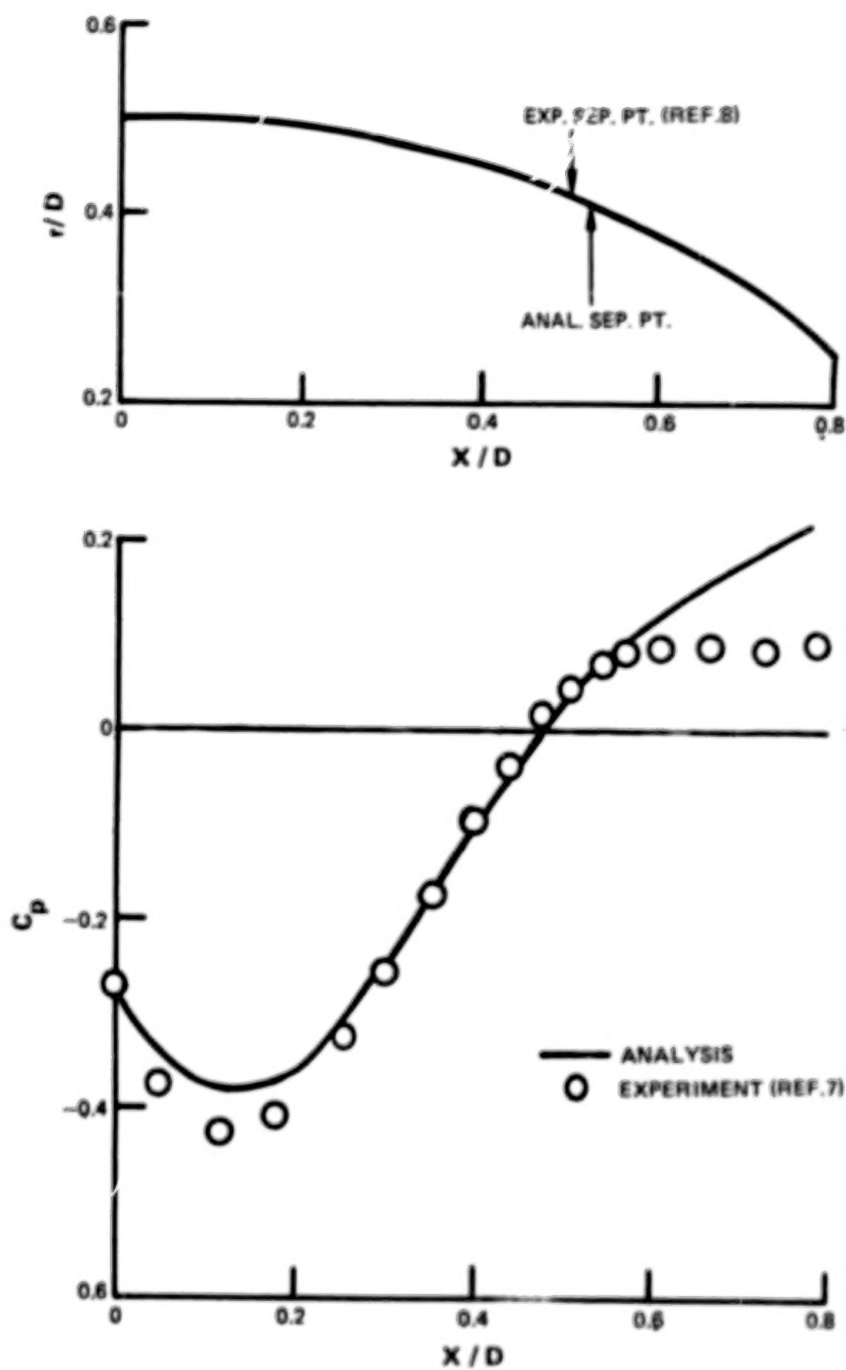


Figure 42 Comparison of Measured and Predicted Afterbody Pressures for a Circular Arc Afterbody With $\beta = 17^\circ$ and $d_f/D = 0.51$ at $M_\infty = 0.8$ and $NPR = 5.0$

BLANK PAGE

APPENDIX
AN AFTERBODY VISCOUS FLOW PROGRAM
USER'S MANUAL

Section	Title	Page
1.0	SUMMARY	61
2.0	GENERAL DESCRIPTION	61
3.0	USE OF VISCOUS SUBROUTINE PACKAGE	62
	3.1 GENERAL DESCRIPTION	62
	3.2 INTERFACE - FORTRAN CALL	63
	3.3 INTERFACE SAMPLE	65
4.0	USE OF STAND-ALONE PROGRAM	67
	4.1 DESCRIPTION	67
	4.2 INPUT	67
5.0	DESCRIPTION OF ROUTINE	72
6.0	GENERAL FLOW DIAGRAM	75

BLANK PAGE

APPENDIX

AN AFTERBODY VISCOUS FLOW PROGRAM USER'S MANUAL

1.0 SUMMARY

VISCUS is a computer subroutine package for analyzing the boundary layer flow separation occurring on aircraft afterbodies. The package is programmed to interface with existing computer programs that calculate external inviscid flow. Because VISCUS is a subroutine package, it cannot be executed without a controlling program. Therefore, to facilitate checkout, a main program – called the Stand-Alone Program – is being provided along with the VISCUS package.

This appendix describes the VISCUS program interface and all routines in the package and also the Stand-Alone Program. The subroutine package and the main program can be obtained from COSMIC, 112 Barrow Hall, University of Georgia, Athens, Georgia 30601.

2.0 GENERAL DESCRIPTION

There are four major calculations in the VISCUS package:

1. calculation of the boundary layer
2. determination of the separation pressure and the separation point
3. calculation of the discriminating streamline
4. combining of all components into an aerodynamic contour.

The VISCUS subroutine package uses the modified Reshoto-Tucker method with the Ludweig-Tillman skin-friction law to calculate the boundary layer. In the first iteration, the boundary layer is calculated over the original contour. Subsequent calculations use the last calculated separated contour.

Four different separation pressures can be calculated in the program, based on either the control volume criterion, Goldschmied's criterion, the modified Page's criterion, or Stratford's criterion. The user selects the criterion, and the program calculates the separation point.

After the second iteration, the separation point locations are averaged. Additional restraints on the movement of the separation point have been included to improve convergence.

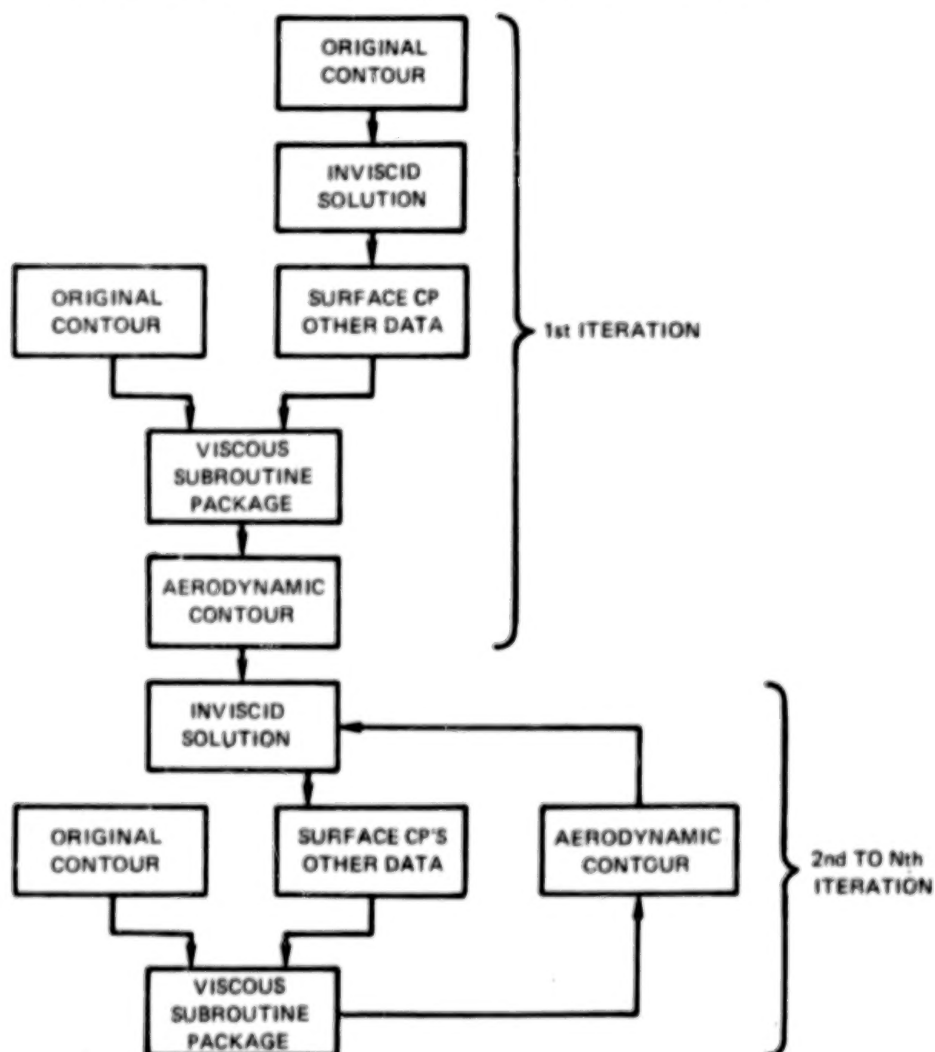
The separation point is used as the starting point for calculating the discriminating streamline. The program uses an axisymmetric control volume calculation that accounts for changing pressure, skin friction, and shear stress. There is also a "jet entrainment" option and jet-entrainment effects are included from the nozzle exit if the option is specified.

The primary output of the VISCUS subroutine package is the aerodynamic contour. And it is calculated by adding the boundary layer displacement thickness to the original or, if separation occurs, to the separated contour. The aerodynamic contour is returned to the inviscid program which uses the revised contour to recalculate the external inviscid solution. See flow diagrams pages 75 to 77.

3.0 USE OF VISCOUS SUBROUTINE PACKAGE

3.1 GENERAL DESCRIPTION

The Viscous Subroutine Package consists of all routines necessary to analyze boundary layer flow separation in the region of aircraft afterbodies. The Package has been designed to interface with an existing computer program system that calculates external inviscid flow. The "interface" is a fortran call that is inserted into the inviscid program after the program has computed surface pressure coefficients (C_p). The Viscous Subroutine Package uses the input contour and computed C_p to determine an aerodynamic contour that is used to calculate inviscid pressures for the next iteration. The procedure is outlined below.



The number of iterations required to converge to a satisfactory solution is a function of the inviscid program and the configuration being analyzed. Experience has shown that ten iterations are usually sufficient.

The following section describes the interface in detail.

3.2 INTERFACE – FORTRAN CALL

The user must include a call to the subroutine VISCUS, as described below. VISCUS is the controlling routine in the Viscous Subroutine Package, calling other subroutines as needed.

CALL VISCUS (INT, FLOT, XA, YIN, CP, RJ, UJ, FLOTO, RADO, AM, THR, DEL, H, CFA, DELI, HI, RET, TAW, PTPT, FNN)

Input Arguments

- INT - integer array used to input integer scalars. Each scalar is assigned an array location.
- INT (1) - number of points used to described contour (imax. = 500).
- INT (2) - array location to start boundary layer calculation.
- INT (3) - array location to start search for separation.
- INT (4) - array location to end search for separation
- INT (5) - jet entrainment option,
 = 0; omit jet entrainment effects,
 = 1; include jet entrainment effects. .
- INT (6) - array location of the nozzle exit.
- INT (7) - smoothing option,
 = 0; do not smooth aerodynamic contour,
 = 1; smooth aerodynamic contour.
- INT (8) - separation pressure option
 = 0: control volume
 = 1; Goldschmied
 = 2; modified Page
 = 3; Stratford
- FLOT - real array used to input real scalars. Each scalar is assigned an array location.
- FLOT (1) - scale option,
 = 12.; input in inches,
 = 1.; input in feet.
- FLOT (2) - thermodynamic wall option,
 = 0.; adiabatic wall,
 = 1.; isothermal wall.

FLOT (3)	-	free stream total pressure.
FLOT (4)	-	free stream total temperature.
FLOT (5)	-	free stream Mach number.
FLOT (6)	-	iteration counter.
FLOT (7)	-	ratio of specific heats.
FLOT (8)	-	initial boundary layer incompressible shape factor.
FLOT (9)	-	initial momentum thickness.
FLOT (10)	-	not used.
FLOT (11)	-	not used.
FLOT (12)	-	shear layer spreading rate constant (input if INT (5) = 1).
FLOT (13)	-	not used.
FLOT (14)	-	not used.
FLOT (15)	-	the axial location of the separation point. If blank or zero, program will calculate separation point.
XA	-	array containing the axial locations of contour.
YIN	-	array containing the radial locations of contour.
CP	-	computed pressure coefficients array.
RJ	-	inviscid plume radius array (input if INT (5) = 1).
UJ	-	jet velocity array (starting at nozzle exit) (input if INT (5) = 1).

Output Arguments

FLOTO	-	array containing scalar output items.
FLOTO (1)	-	pressure drag.
FLOTO (2)	-	separation pressure (control volume).
FLOTO (3)	-	separation pressure (Goldschmied).
FLOTO (4)	-	separation pressure (modified Page).
FLOTO (5)	-	separation pressure (Stratford)
FLOTO (6)	-	separation angle, degrees.
FLOTO (7)	-	axial location of separation point.
RADO	-	aerodynamic contour array.
AM	-	Mach number array.
THR	-	momentum thickness of the boundary layer array.
DEL	-	displacement thickness of boundary layer array.
H	-	compressible shape factor of the boundary layer array.

CFA	-	skin friction coefficient array.
DELI	-	thickness of the boundary layer array.
HI	-	incompressible shape factor of the boundary layer array.
RET	-	Reynolds number based on momentum thickness array.
TAW	-	adiabatic wall temperature array.
PTPT	-	ratio of boundary-layer-total-pressure to free-stream-total-pressure array.
FNN	-	exponential shape factor of boundary layer profile array.

3.3 INTERFACE SAMPLE

The printout below is for a simplistic, inviscid program intended only as an example of how the interface between the inviscid program and the Viscous Subroutine Package might be handled.

INVISCID PROGRAM

```

      DIMENSION      INT( 8), FLOT(15),  XA(500), YIN(500),  CP(500)
1      ,  RJ(500),  UJ(500), FLOT( 7), KADD(500),  AM(500)
2      ,  THR(500), DEL(500),  H(500),  CFA(500), DELI(500)
3      ,  HI(500), RET(500),  TAW(500), PTPT(500),  FNN(500)
4      ,VAERO(500)
      .
      .
      .
      READ (5,500) NN,NMIN,NMAX,IJET,NEXT
(500 FORMAT (5I5)
      WRITE(6,600) NN,NMIN,NMAX,IJET,NEXT
600 FORMAT(' NUMBER OF INPUT POINTS              =', 15, /
1      ' LOCATION TO START SEPARATION SEARCH      =', 15, /
2      ' LOCATION TO END SEPARATION SEARCH        =', 15, /
3      ' JET ENTRAINMENT OPTION                  =', 15, /
4      ' LOCATION OF NOZZLE EXIT                  =', 15, )
      READ (5,510) Z,TWW,PT,TT,AMIN,GA,HIX,THRR,XSEP,C,ALTER
510 FORMAT (8F10.0)
      WRITE(6,610) Z,TWW,PT,TT,AMIN,GA,HIX,THRR,XSEP,C,ALTER
610 FORMAT(' SCALE OPTION                          =', F12.5, /
1      ' THERMODYNAMIC WALL OPTION                =', F12.5, /
2      ' FREE STREAM TOTAL PRESSURE                =', F12.5, /
3      ' FREE STREAM TOTAL TEMPERATURE            =', F12.5, /
4      ' FREE STREAM MACH NUMBER                  =', F12.5, /
5      ' RATIO OF SPECIFIC HEATS                  =', F12.5, /
6      ' INITIAL BOUNDARY LAYER SHAPE FACTOR       =', F12.5, /
7      ' INITIAL MOMENTUM THICKNESS                =', F12.5, /
8      ' INPUT SEPARATION POINT (OPTIONAL)         =', F12.5, /

```

```

9      * SHEAR LAYER SPREADING RATE      =*, F12.5, /
A      * NO. OF ITERATIONS              =*, F12.5, )
      READ (5,520) (XA(I),YIN(I),I=1,NN)
520 FORMAT (2F10.0)
      WRITE(6,620) (XA(I),YIN(I),I=1,NN)
620 FORMAT (1 * X INPUT    Y INPUT*, / (2F12.5))
      .
      .
      .

```

ANA IS THE ITERATION COUNTER

```
ANA      = 1.
```

FIRST ITERATION

```

      DO 10 I=1,NN
10  YAERO(I)= YIN(I)
      .
      .
      .
20 CONTINUE

```

CALL ROUTINE TO CALCULATE INVISCID SOLUTION

```

      CALL INVIS (XA,YAERO, . . . , CP)
      .
      .
      .

```

SET UP ARRAYS FOR VISCOUS PACKAGE

```

INT(1)  = NN
INT(2)  = 1
INT(3)  = NMIN
INT(4)  = NMAX
INT(5)  = IJET
INT(6)  = NEXT
INT(7)  = 1
INT(8)  = 0
FLOT(1) = Z
FLOT(2) = TW
FLOT(3) = PT
FLOT(4) = TT
FLOT(5) = AMIN
FLOT(6) = ANA
FLOT(7) = GA
FLOT(8) = MIX
FLOT(9) = THRR
FLOT(12)= C
FLOT(15)= XSEP

```

REMEMBER TO INPUT ORIGINAL CONTOUR TO VISCUS

```
CALL VISCUS (INT, FLOT, XA, YIN, CP, KJ, UJ, FLOTD, RADO, AN, THR, DEL  
1           , H, CFA, DELI, HI, RET, TAN, PTPT, FNN)
```

CHECK IF ITERATION COMPLETE

IF (ANA .GE. AITER) GO TO 999

USE AERODYNAMIC RADII FOR NEXT INVISCID CALCULATION

```
DO 30 I=1, NN  
30 YAERO(I) = RADU(I)  
ANA = ANA + 1.
```

RETURN TO INVISCID SOLUTION

GO TO 20

•
•
•

999 STOP
END

4.0 USE OF STAND-ALONE PROGRAM

4.1 DESCRIPTION

The stand-alone program consists of a main routine and the viscous subroutine package described in Section 3. The main routine reads input, calls the subroutine package, and prints output. The functions of the stand alone program are to define the input to the viscous package, to provide an example of an interface with the viscous package, and to print output from one iteration of the viscous package.

4.2 INPUT

DATA INPUT TO DECK B851

DATE: _____

CARD _____ ; TITLE: Input to Stand Alone ProgramFORMAT (Namelist input)

GENERAL INSTRUCTIONS : Follow general rules for namelist input. The name of the input is NAME.

COLUMNS	VARIABLE TYPE	FIELD NAME	REMARKS AND/OR DESCRIPTIONS
	Integer	NN	Number of input contour points (max. = 500)
	Integer	NAZ	Array location to start boundary calculation.
	Integer	NMIN	Array location of minimum CP. The search for separation starts at this location.
	Integer	NMAX	Array location of end of afterbody. The search for separation ends at this location.
	Integer	NEXT	Array location of nozzle exit.
	Integer	IJET	Jet entrainment option = 0; no jet entrainment ≠ 0; jet entrainment
	Integer	ISMOO	Smoothing option. = 0; no smoothing = 1; smooth aerodynamic contour
	Integer	IPRESS	Separation pressure option = 0; control volume = 1; Goldschmied = 2; modified Page = 3; Stratford
	Real	Z	Scaling option to convert input to feet units = 12. , input inches = 1. , input feet

5.0 DESCRIPTION OF ROUTINE

This section briefly describes all routines in the Viscous Subroutine Package. The routines are described in the order (top to bottom, left to right) outlined in the block diagram shown on the next page.

VISCUS

The VISCUS routine is the interface with the inviscid program and the controlling routine of the viscous package. The routine, in addition to these functions, calculates the total velocity from the inviscid surface pressure coefficient, calculates the cross-sectional area of the separated contour, and determines the axial location of the separation point.

SHAPEJ

The SHAPEJ subroutine interfaces between VISCUS and SUMA and also sets boundary conditions for SUMA.

SUMA

The first derivative of the cross-sectional area versus axial location is calculated in SUMA routine. The routine fits a parabolic arc using a least-square fit before the derivatives are calculated.

NEWBL

The NEWBL routine calls the routine that calculates the boundary layer. After the boundary layer is calculated, the routine computes the component of the displacement normal to the x axis.

BLC

The BLC routine uses the modified Reshotko-Tucker method and the Ludweig-Tillman skin-friction law to calculate the boundary layer growth. The original contour is used for the first iteration. The separated contour is input for the other iterations.

FIX

The location of the minimum pressure coefficient is calculated in the FIX routine. The search region should be limited to the afterbody.

POWER

The axial coordinates are raised to integer powers and saved in a common statement. They are used in the separation pressure calculation.

SEPA

The SEPA routine calculates the separation pressure. Four different methods are used. The "user" can select Stratford's, Goldschmied's, modified Page's, or the Control Volume Criterion.

PRFL

The SEPA routine calls the PRFL routine to determine boundary properties based on the law-of-the-wall - the law-of-the-wake.

FLUX

The FLUX routine calculates integral boundary layer properties such as displacement and momentum thickness.

INTEG

The FLUX routine calls the INTEG routine to do the necessary numerical integration. The routine uses Simpson's rule.

SEP

The SEP routine controls the calculation of the discriminating streamline and the aerodynamic contour. Before separation and after reattachment, the aerodynamic contour is the original contour plus the boundary layer displacement thickness. In the separated region, the aerodynamic contour is determined by adding the displacement thickness to the discriminating streamline.

B834

The discriminating streamline is calculated in the B834 routine. A control volume technique is used.

JET

The JET routine calculates the effect of jet entrainment on the discriminating streamline. The JET routine is called only if the jet option is turned on.

NEWRAP

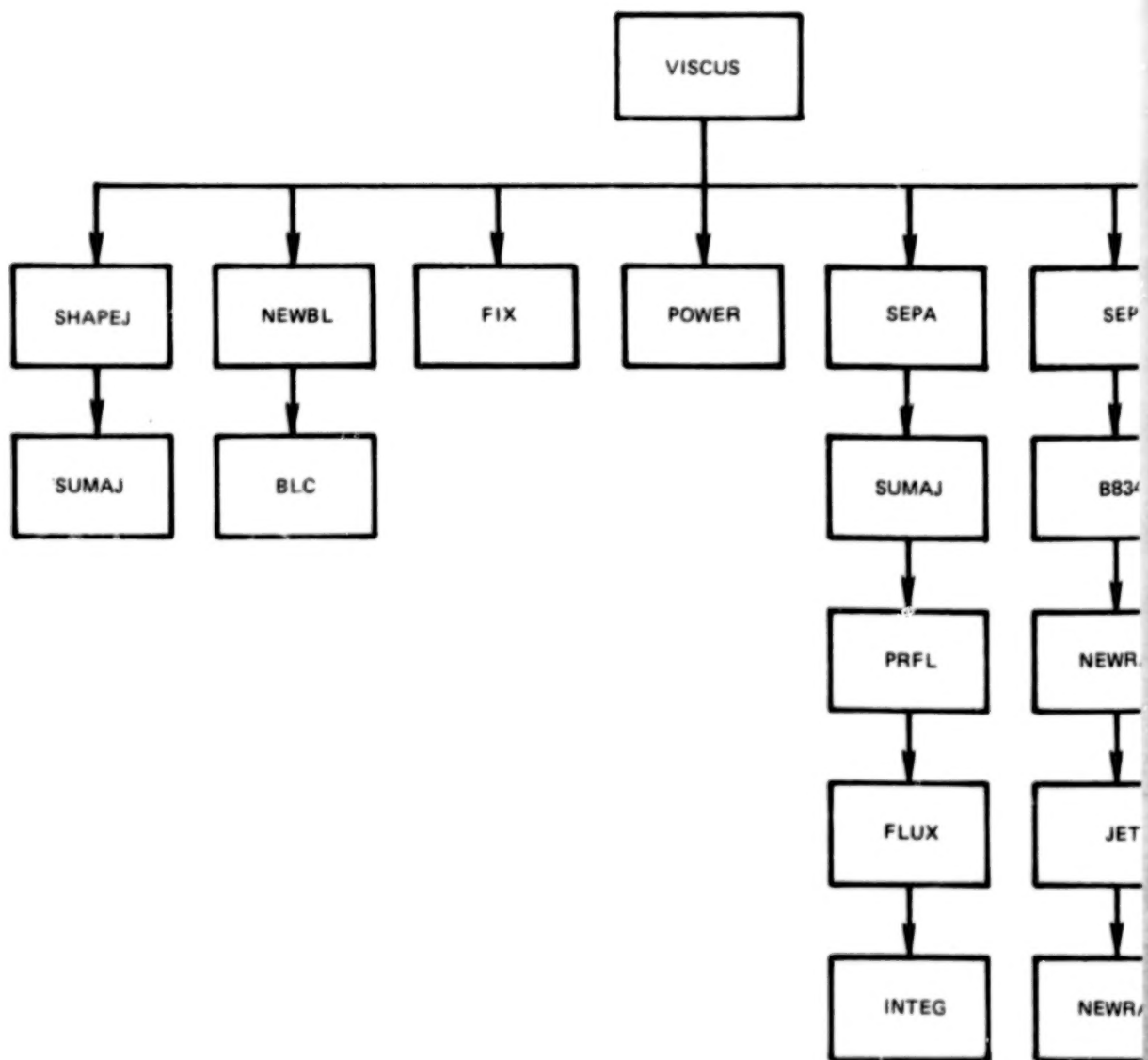
Both the B834 and the JET routines use the NEWRAP routine. The subprogram uses the Newton-Raphson method to predict the zero point of functions.

SMINT-SMOOTH-MSMTH-RSMTH

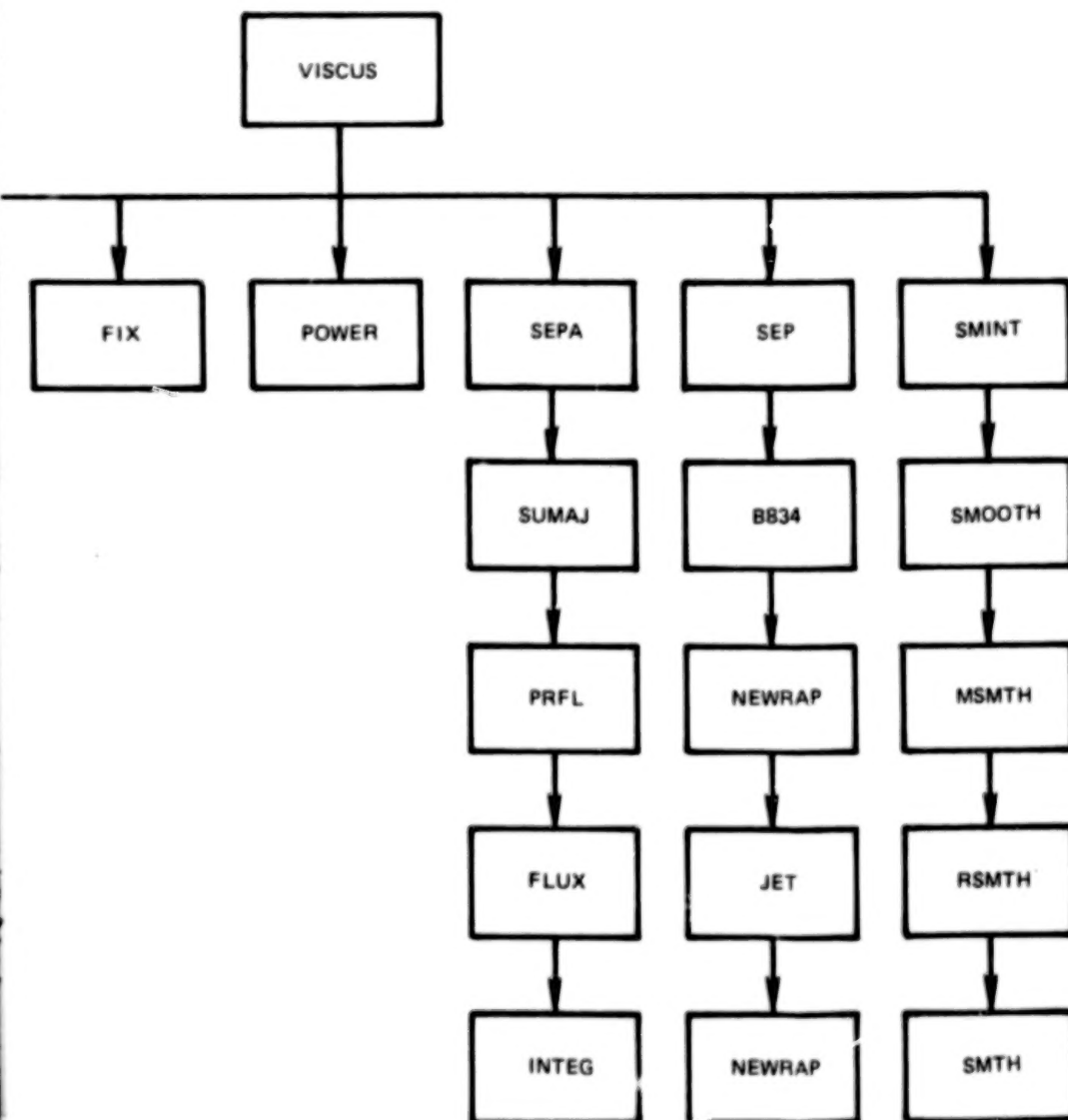
The SMINT-SMOOTH-MSMTH-RSMTH routines set up the contour for the smoothing routine. They set boundary conditions and divide the contour into equal increments.

SMTH

The SMTH routine smooths the contour, using terms from the Taylor series expansion for a polynomial.

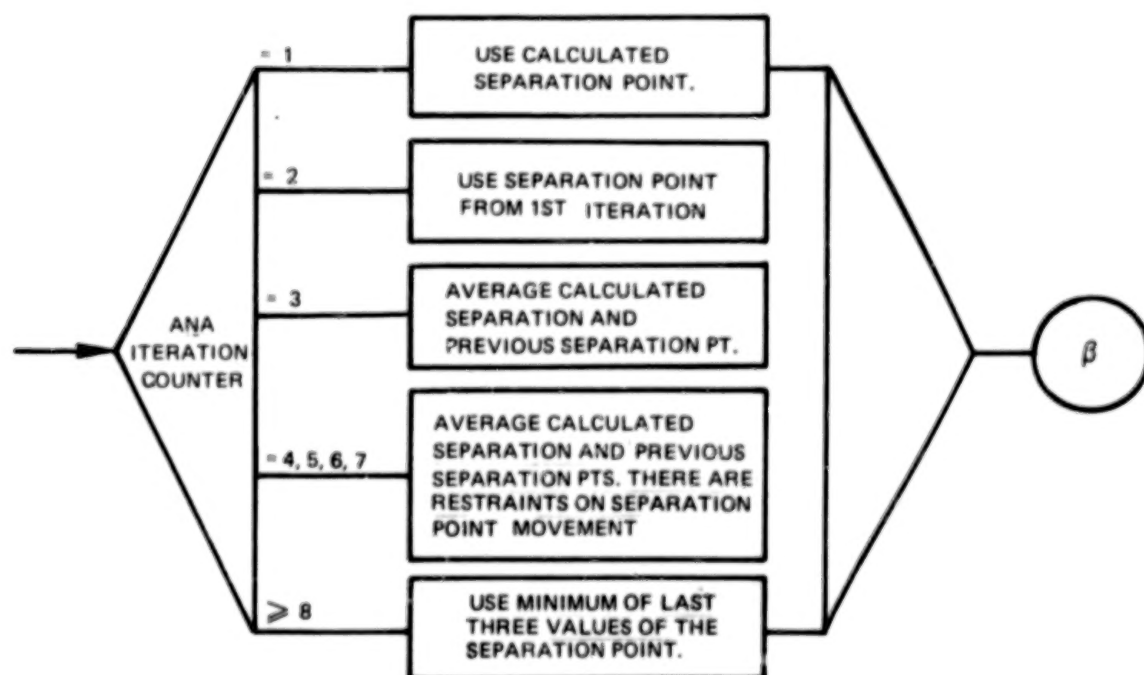
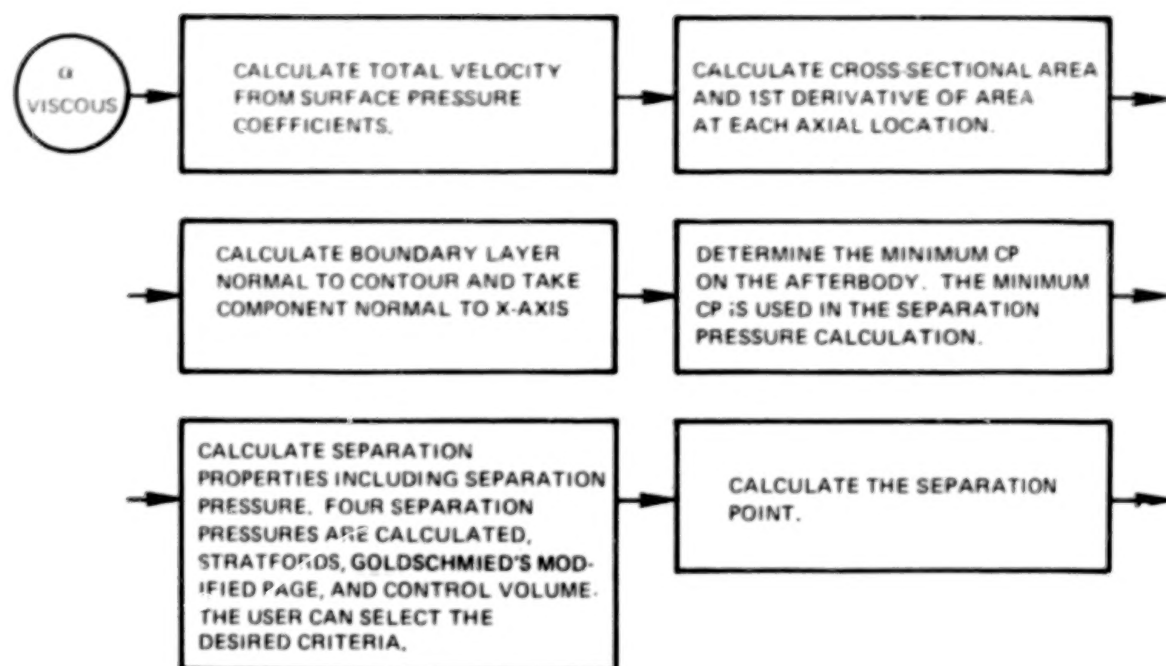


Viscous Subroutine Block Diagram

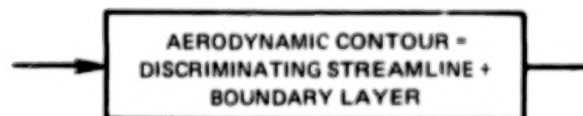
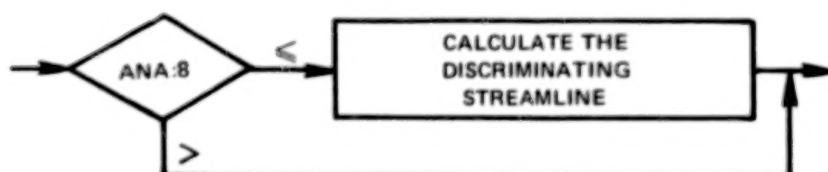
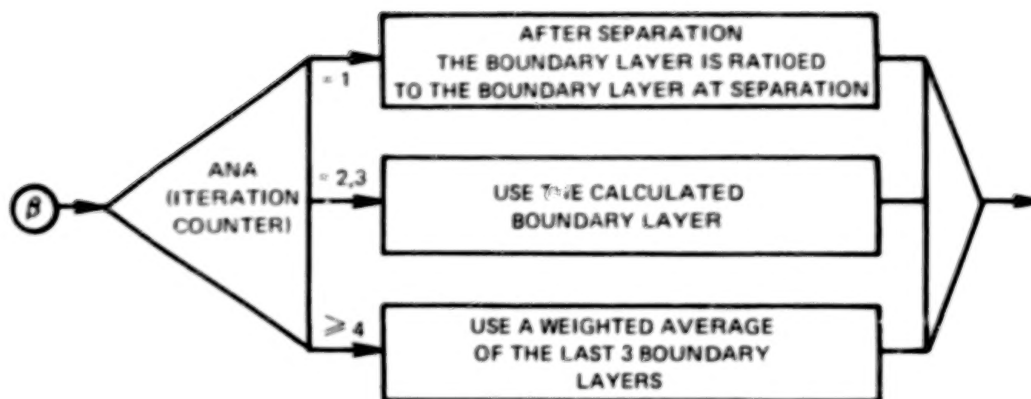


Viscous Subroutine Block Diagram

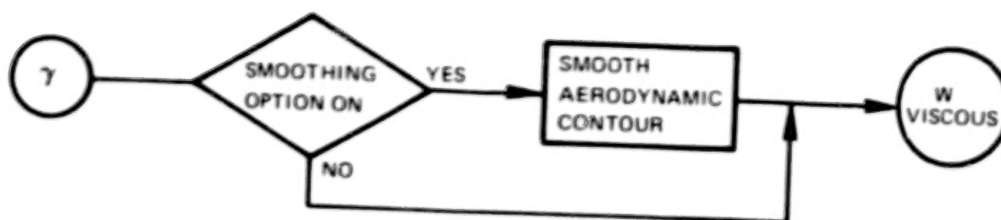
6.0 GENERAL FLOW DIAGRAM



GENERAL FLOW DIAGRAM



GENERAL FLOW DIAGRAM (Cont'd)



GENERAL FLOW DIAGRAM (Cont'd)

1. Report No. NASA CR- 3028	2. Government Accession No.	3. Recipient's Catalog No.
4. Title and Subtitle An Improved Analytical Model of the Separation Region on Boattail Nozzles at Subsonic Speeds		5. Report Date July 1978
7. Author(s) W. M. Presz, Jr., R. W. King, and J. D. Buteau		6. Performing Organization Code
9. Performing Organization Name and Address Pratt & Whitney Aircraft Group Commercial Products Division United Technologies Corporation East Hartford, CT 06108		8. Performing Organization Report No. PWA-5599
12. Sponsoring Agency Name and Address National Aeronautics and Space Administration Washington, D. C. 20546		10. Work Unit No.
		11. Contract or Grant No. NAS1-14462
		13. Type of Report and Period Covered Contractor Report
		14. Sponsoring Agency Code
15. Supplementary Notes NASA Project Manager: Mr. Lawrence E. Putnam, NASA-Langley Research Center Final Report		
16. Abstract <p>Boundary layer flow separation often occurs on the afterbody of aircraft, increasing drag, decreasing performance. The complexities of this phenomenon limit solutions of the governing equations to simplified flowfields. Because present methods are unreliable, this program was undertaken. A practical engineering calculation was developed to model the viscous effects of a separated, reverse-flow region on afterbody pressures and drag. This viscous calculation is iteratively coupled with an inviscid-flow calculation by means of an aerodynamic interface. A standard boundary layer displacement thickness is used to modify the afterbody shape where the flow is attached. A discriminating streamline calculation is developed to account for displacement effects of the reverse flow in separated regions with and without a flowing jet. The viscous flow calculation is coupled with a potential flow calculation. The analysis accurately predicted afterbody pressures and drag with variations in Reynolds number, Mach number, and afterbody shape.</p>		
17. Key Words (Suggested by Author(s)) Jet Aircraft Afterbody Flow Separation New Calculation Procedure Viscous and Inviscid Flow Calculation Afterbody Pressures and Drag		18. Distribution Statement Unclassified - Unlimited Subject Category 02
19. Security Classif. (of this report) Unclassified	20. Security Classif. (of this page) Unclassified	21. No. of Pages 85
		22. Price* \$6.00

* For sale by the National Technical Information Service, Springfield, Virginia 22104

NASA-Langley, 1978

90

50

END

NOV 28 1978